Quasi-One-Dimensional van der Waals Lattices with Diverse Magnetism: New Platforms Towards Ultrathin Magnetic Nanowires

by

Yi Qu (曲艺)

B. S. Chemistry
Nanjing University 南京大学 (2017)

SUBMITTED TO THE DEPARTMENT OF CHEMISTRY

IN PARTIAL FULFILLMENT OF THE REQUIREMENTS FOR THE DEGREE OF

DOCTOR OF PHYLOSOPHY IN CHEMISTRY

AT THE

MASSACHUSETTS INSTITUTE OF TECHNOLOGY

September 2022

Author ....
Department of Chemistry
June 29, 2022

Certified by ....
Mircea Dincă
W. M. Keck Professor of Energy
Thesis Supervisor

Certified by ....
Adam Willard
Associate Professor
Graduate Officer

This doctoral thesis has been examined by a Committee of the Department of Chemistry as follows:

Professor Timothy M. Swager ....

Chairman, Thesis Committee
John D. MacArthur Professor of Chemistry

Professor Mircea Dincă ....

Thesis Supervisor
W. M. Keck Professor of Energy

Professor Moungi Bawendi ....

Member, Thesis Committee
Lester Wolfe Professor of Chemistry

Quasi-One-Dimensional van der Waals Lattices with Diverse Magnetism: New Platforms Towards Ultrathin Magnetic Nanowires

by

Yi Qu

Submitted to the Department of Chemistry

On June 29, 2022 in Partial Fulfillment of the

Requirements for the Degree of Doctor of Philosophy in

Chemistry

Abstract

One-dimensional (1D) or quasi-1D van der Waals (vdW) magnets, which feature covalently bonded spin chains or ladders separated by weak vdW interactions, could potentially offer twofold benefits for the current field of 1D magnets. On the one hand, the bulk crystals of these phases are more ideal 1D magnets because large vdW gaps effectively prevent any inter-chain or inter-ladder exchange couplings. This allows for the study of unique 1D magnetic fluctuations coupled with 1D characteristic transport behaviors. On the other hand, the vdW gaps open up possibilities to exfoliate these 1D vdW magnets for magnetic nanowire production. These nanowires would then be used to investigate 1D confinement effects and for densely packed spintronics. In this thesis, efforts to synthesize new quasi-1D vdW magnets, control their bulk magnetism, and efficiently exfoliate them into high-quality nanowires are detailed. Chapter 1 reviews the definitions and fundamental physics of 1D magnets, discusses limitations with the current routes to access 1D magnets, and introduces lessons from the breakthroughs in two-dimensional (2D) magnets, which serve as the starting point of this thesis work. Chapter 2 demonstrates the first exfoliation strategy developed for quasi-1D vdW magnet $CrSbSe_3$ and presents the properties of the resulting nanowires. The exfoliated $CrSbSe_3$ nanowires have high aspect ratio, well-defined crystallinity, smooth surfaces, and high stability, and exhibit stronger coercivity compared to bulk $CrSbSe_3$ due to the stronger shape anisotropy therein. Chapters 3 and 4 are concerned with expanding the library of quasi-1D vdW magnets and efficiently controlling their bulk magnetic properties. Chapter 3 demonstrates the substitution of Se in $CrSbSe_3$ with S switches the overall magnetic ordering from ferromagnetic (FM) to antiferromagnetic (AFM) and discusses the metamagnetic transition and strong spin-phonon coupling in the resulting AFM spin-ladder phase $CrSbS_3$. Chapter 4 demonstrates that Bi alloying into the Sb sites in $CrSbSe_3$ and $CrSbS_3$ is an efficient strategy to enhance the magnetic anisotropy without altering the original 1D structural features or magnetic ground state. This offers an independent dimension to finely tune the magnetic behaviors of these quasi-1D vdW magnets.

Thesis Supervisor: Mircea Dincă

Title: W. M. Keck Professor of Energy

Contents

Chapter 3. Metamagnetic Transitions in $CrSbS_3$: A Quasi-One-Dimensional van der Waals Antiferromagnet

Chapter 4. Two Series of Quasi-One-Dimensional van der Waals Magnetic Lattices with Finely Tuned Magnetic Anisotropy 95

Chapter 1

Introduction to One-Dimensional Magnetic Solids

1.1 Abstract

Low-dimensional magnetic systems, especially one-dimensional (1D) magnetic solids, have long caught the research attention due to their unconventional physical properties and their potential for nanoscale technological applications. This first part of this chapter reviews the definitions and promises of low dimensional magnets and summarizes some fundamental solid-state physics crucial to understanding the behaviors of low dimensional magnets. The second part of this chapter reviews the current approaches to accessing 1D magnetic solids, discusses the limitations and sophistications of these approaches, and demonstrates how the recent breakthroughs enabled by two-dimensional (2D) van der Waals (vdW) magnets offer valuable lessons to address the limitations of current 1D magnetic systems. Our efforts following these lessons to develop 1D vdW magnetic materials will be further discussed in Chapters 2, 3, and 4.

1.2 Significance and Definitions of Low-Dimensional Magnets

Magnetism, together with superfluidity, charge-density waves, and superconductivity, is among the most crucial quantum cooperative phenomena observed in condensed matter at low temperatures. It has attracted vast research interest due to its theoretical complexity and technological significance.[1-3] From the theoretical point of view, constant progress has been made to theoretically describe the behaviors of the magnetic behaviors and their interactions with the other properties of magnets, such as electronic, optical, and thermal properties. For example, the theories of exchange interactions (e.g., direct exchange, superexchange, double exchange) have

been developed to explain the phenomenon of long-range magnetic ordering.[4-5] The theories of spin-orbit coupling have been proposed to describe magnetoelastic and magneto-optical effects. In terms of technical applications, numerous technological achievements based on magnets have significantly changed people's lives. Permanent magnets are widely used in wind power generators, electronic devices, and small motors.[6-8] The giant magnetoresistance effect in magnetic multilayers has enabled the design of hard disk drives and revolutionized the data storage industry. Magnetic materials are also crucial for the emerging field of spintronics, which allows for high-speed data processing and high circuit integration density and is envisioned to be the core of the next-generation information technology. [9-10]

Among the fundamental studies of magnetism, one most interesting and rapidly developing area is the investigation of magnetic systems with reduced dimensionalities, namely, zero-dimensional (0D), one-dimensional (1D), or two-dimensional (2D). In low-dimensional magnets, the quantum essence of matter manifests itself most clearly, and both the quantum fluctuations and frustrations become more significant. Therefore, their magnetic properties depend on the subtle balance between several factors, including the spin fluctuations, magnetic correlations, the charge ordering, and the spin-lattice or electron-lattice couplings. By tuning their relative strengths, it becomes possible to observe various quantum cooperative effects. For example, exotic ground states can be realized, such as nonmagnetic singlet,[11] spin-liquid,[12] Luttinger-liquid,[13] and superconducting ground states.[14] Novel dynamic behaviors can be observed, such as cascades of spin-reorientations, magnetization plateau, and instabilities of the spin subsystem induced by external magnetic field.[15]

For magnetic systems, the reduction of dimensionality can be structural, as in the case of magnetic nanoclusters (0D), magnetic nanowires (1D), and magnetic thin films (2D), which may offer superior performances over traditional materials. Their unique properties are mainly due to the size effects, leading to confinement effects or great sensitivity to external stimuli, and the surface effects, promoted through the significantly larger number of surface atoms compared to volume atoms. For example, giant magnetic anisotropy has been observed in ultra-thin films or ultra-thin nanowires due to the broken symmetry at surfaces/interfaces.[16] Nanoscale size confinement and high aspect ratio morphological confinement within nanowires have led to the observation of unconventional domain wall structures and motions, which have already been used for novel data storage devices, such as racetrack memory. [10, 17-18]

The reduction of dimensionality can also be magnetic, which may occur in otherwise structurally 3D compounds due to the directional nature of the chemical bonding. Within this definition, magnetic systems of low dimensionality arise when the anisotropic structural connections or electronic interactions translate into anisotropic magnetic couplings, thereby reducing the effective dimensionality of the magnetic subsystem. Therefore, a 1D magnet is a magnetic system where the spin interactions are strong only along a well-defined direction of the space, thus defining quasi-isolated chains of spins. When the spin interactions are strong along two directions of the space and weak along the third one, the spin system can be viewed as a stacking of quasi-isolated magnetic layers and a 2D magnet. The "intermediate" state, i.e., quasi-1D magnet, is a system where each 1D spatial unit consists of a few coupled chains or a zigzag chain. Therefore, each spin not only interacts with two nearest neighbors but also with the next nearest neighbors within each 1D magnetic motif. This definition of low-dimensional magnets is frequently used in the theoretical and experimental studies of highly directional spin-spin interactions and the resulting quantum phenomena at the bulk level rather than at the nanoscale. Over the past decades, several strategies have been developed to synthesize low-dimensional magnetic phases that approximately fit this definition and these synthetic routes will be discussed in Section **1.4.2**.

In this chapter, we focus on magnets with reduced dimensionality both in terms of structure/morphology (e.g., nanowires and thin films) and in terms of magnetic interactions such as 3D lattices with cation-separated spin ladders. Section **1.3** reviews the fundamental physics of magnetic ordering and magnetic anisotropy in low-dimensional magnets, which are crucial factors to understand low-dimensional magnetism. Section **1.4** surveys the current synthetic routes to fabricate low-dimensional magnets with a particular emphasis on 1D and quasi-1D magnets and discusses the limitations of these routes. Section **1.5** introduces the recent ground-breaking developments in the field of 2D magnets and potential strategies taught by the 2D magnets to access 1D magnets with unprecedented structural advantages. With these lessons in mind, Section **1.6** and **1.7** further analyzes the feasibility of extending the fabrication strategies developed for 2D magnets to 1D systems, which serve as the starting point and foundation of this thesis work.

1.3. Fundamental Physics of Low-Dimensional Magnets

1.3.1 Magnetic Ordering of Low-Dimensional Magnets

One crucial topic of solid-state magnetism is the appearance of spontaneous magnetic order at low temperatures. Many traditional terms being used for hundreds of years, such as ferromagnets and antiferromagnets, are all used to describe ordered phases. According to the general theory of phase transitions, a spin system at a given temperature T is characterized by an order parameter which is generally defined as the value of magnetization **M**. The magnetic system exhibits a phase transition towards long-range ordering if the magnetization becomes non-zero below a certain characteristic temperature T_C, which is called the critical temperature.

It is now widely acknowledged that the existence of a magnetic phase transition or long-range magnetic ordering at finite temperature depends crucially on both the space dimension (D) and spin dimension (n). Following the commonly used terminology, $n = 1, 2$, and 3 correspond to the so-called "Ising", "XY" and "Heisenberg" models, respectively.[19-20] According to the Mermin-Wagner theorem, in space dimension $D = 2$, a true phase transition exists only for the Ising systems, where strong anisotropy forces the spins to lie parallelly or antiparallelly along only one axis without any canting. In Ising systems, the intermediate states when flipping a spin to the opposite direction, which necessarily involves deviations from the preferred axis, are strongly unfavored, and an energy barrier exists for any disturbance of the uni-axial spin alignment, allowing for long-range ordering at finite temperatures.[21-22] However, in the space dimension $D = 1$, the strength of spin fluctuations increases so much that no spontaneous magnetization can appear down to T = 0 K, and there is no energy barrier for magnetic excitations, even in the Ising system. This is because long-range order in a chain of spins coupled with an exchange interaction J is destroyed by the flip of just a single spin. When a spin is flipped, the magnetic energy increases by $2J$, while the entropy increases by $kT\ln N$. The change of the free energy upon the flip of a spin is defined as

$$\Delta F = 2J - kTlnN \tag{1.1}$$

and can be made negative at any arbitrarily non-zero temperature if the number of spins N in the chain is large enough.[19, 23]

As the intermediate between chain (1D) and plane (2D), spin ladders are magnetic systems where two spin chains are put next to each other either with "overlap" (**Figure 1.1a**) or "zigzag" alignment (**Figure 1.1b**).[24] Compared to purely 1D spin chain systems, such quasi-1D magnetic subsystems have more neighboring interactions around each spin and weaker fluctuations, and therefore, an energy gap in the spin excitation spectrum can be achieved under certain conditions, and a magnetic ground state with long-range ordering can be accessed at finite temperature.[25-27] The ordering behavior of quasi-1D magnets is further diversified by the competing exchange interactions between spins along the leg direction and the rug direction, the anisotropy of each spin, and the anisotropy of each exchange coupling. Consequently, in addition to typical long-range ordering, these quasi-1D magnets can also exhibit many unconventional ordering behaviors, such as a spiral spin structure or a spin-liquid state.

Figure 1.1. **a)** The standard spin-ladder. **b)** The "zigzag" spin-ladder

1.3.2 Magnetic Anisotropy of Low-Dimensional Magnets

Magnetic anisotropy is the preference for the magnetization to lie in a particular axis in a sample and this axis is called magnetic easy axis. Accordingly, those directions that require more energy to align the magnetization are called magnetic hard axes. Magnetic anisotropy can originate from sample shape, crystal symmetry, stress, or directed atomic pair ordering and therefore may include magnetocrystalline anisotropy, shape anisotropy, and surface anisotropy. For low-dimensional magnets, magnetic anisotropy plays a central and sometimes even deterministic role in their ordering behaviors and magnetic properties. On the one hand, for 3D lattices with 1D or 2D magnetic motifs, magnetic anisotropy is an essential prerequisite for stabilizing any long-range magnetic ordering, as inferred from the Mermin-Wagner theorem discussed in **1.3.1**. On the other hand, for morphologically 1D or 2D magnetic materials, such as magnetic nanowires or thin films,

shape anisotropy and surface anisotropy can significantly control their magnetic performances, including the coercivity, magnetization values, and magnetoresistance. Therefore, before examining the known examples of low-dimensional magnets and strategies to tune their magnetic properties, we want to briefly discuss different types of magnetic anisotropy and how they may be rationally controlled by adjusting the material composition, shape, and surface states.

1.3.2.1 Magnetocrystalline Anisotropy

In crystalline magnetic materials, magnetocrystalline anisotropy is an intrinsic property determined by atomic stacking structures. The origin of magnetocrystalline lies in the coupling of the spin moments to the shape and orientation of electronic orbitals *via* spin-orbit coupling, which is further coupled to the chemical bonding of the orbitals on a given atom within their local environment *via* crystal field interactions. If the local crystal field felt by an atom is of low symmetry and if the bonding electrons of that atom have an asymmetric charge distribution ($L_Z \neq 0$), then the atomic orbitals interact anisotropically with the crystal field. Such preferred orientations of molecular orbitals or electron distributions then lead to certain preferred orientations of the spin moments along particular crystallographic directions. As a result, it is essential for magnetocrystalline anisotropy that there be a significant directional character to the bonding and strong spin-orbit coupling.[28]

1.3.2.2 Shape Anisotropy

For non-spherical magnets, the magnetic dipolar interactions along different sample axes generate different magnetostatic energies. The magnetic dipoles tend to lie in a certain direction to minimize the magnetostatic energy, which is the origin of magnetic shape anisotropy. This is intrinsically because the two poles located at two ends of a magnet (north and south) not only provide an external stray field but also generate a "demagnetizing field" ($\mathbf{H}_d$) inside the magnet, and

$$\mathbf{H}_d = -N\mathbf{M} \qquad (1.2)$$

where N is the demagnetizing tensor and is the sum of demagnetizing factors N_a, N_b, N_c along the a, b, c axes, respectively, with $N_a + N_b + N_c = 1$.[29]
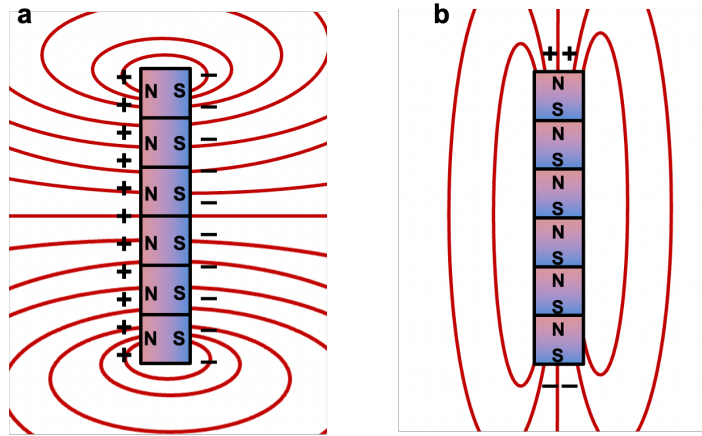

Figure 1.2. An illustration of the origin of shape anisotropy in nanowires

To better illustrate the concept of demagnetizing field and shape anisotropy in 1D magnets, we can think of a nanowire being built from small magnetic cubes. If the magnetic dipoles (symbolized by + and –) are presented along the long side of the wire (**Figure 1.2a**), the large surface creates a strong stray field, and strong repulsive forces exist when bringing these cubes together. Instead, suppose the magnetization lies along the wire axis (**Figure 1.2b**). In this case, it is energetically favorable for all cubes to attract each other and assemble into long wires, and the magnetic dipoles at both ends only create a small stray field. As a result, the shape of nanowires strongly favors an alignment of magnetization along the wire direction, and this shape anisotropy energy increases as the aspect ratio of the nanowires increases. Switching the magnetization direction in nanowires requires at least a partial or temporary formation of the unfavorable configuration shown in **Figure 1.2a**, so an energy barrier (i.e., a certain magnetic field) is required to change the magnetization of nanowires. Consequently, a hysteresis loop with large coercivity can be observed within 1D magnetic systems possessing strong shape anisotropy.

1.3.2.3 Surface Anisotropy

Magnetic surface anisotropy arises because the surface states have lower symmetry, which enhances the magnetocrystalline anisotropy at the surface. It is affected by the roughness of surfaces and the lattice mismatch at each interface and becomes more dominant as the surface-to-

volume ratio increases, which is usually the case for nanoscale materials. For example, for a magnetic thin film, the effective anisotropy constant can be viewed as the sum of three terms

$$K = \frac{2K_s}{t} + K_v - \mu_0 M^2 \qquad (1.3)$$

where the first term represents the surface anisotropy. K_s is the surface anisotropy constant, and t is the thickness of the layer. The second term is volume anisotropy due to magnetocrystalline anisotropy or lattice strains, and the third term is shape anisotropy determined by the dipolar interactions between two magnetic poles. Among these terms, the contribution of surface anisotropy is the only one that depends on the film thickness t and may dominate the overall magnetic anisotropy as t decreases. Consequently, although the dipolar term favors the in-plane orientation of magnetization in thin films, many ultra-thin films exhibit spontaneous magnetization perpendicular to the film plane, and this can be particularly useful in recording applications.[30-31]

1.4 Synthetic Pathways to Obtain 1D Magnets

As introduced in **1.2**, for magnetic systems, the reduction of dimensionality can be structural or magnetic, so in this section, we will use these two definitions to categorize the current techniques to achieve the correspondingly defined low-dimensional magnets. We focus primarily on 1D magnets, including structurally and morphologically 1D magnets such as magnetic nanowires, and 3D magnetic lattices with 1D or quasi-1D magnetic units such as spin-chain compounds and spin-ladder compounds. We also point out the limitations and complications of each category of synthetic routes and the reasons why a novel fabrication strategy is warranted to access 1D magnetic systems.

1.4.1 Synthesis of 1D Magnetic Nanostructures
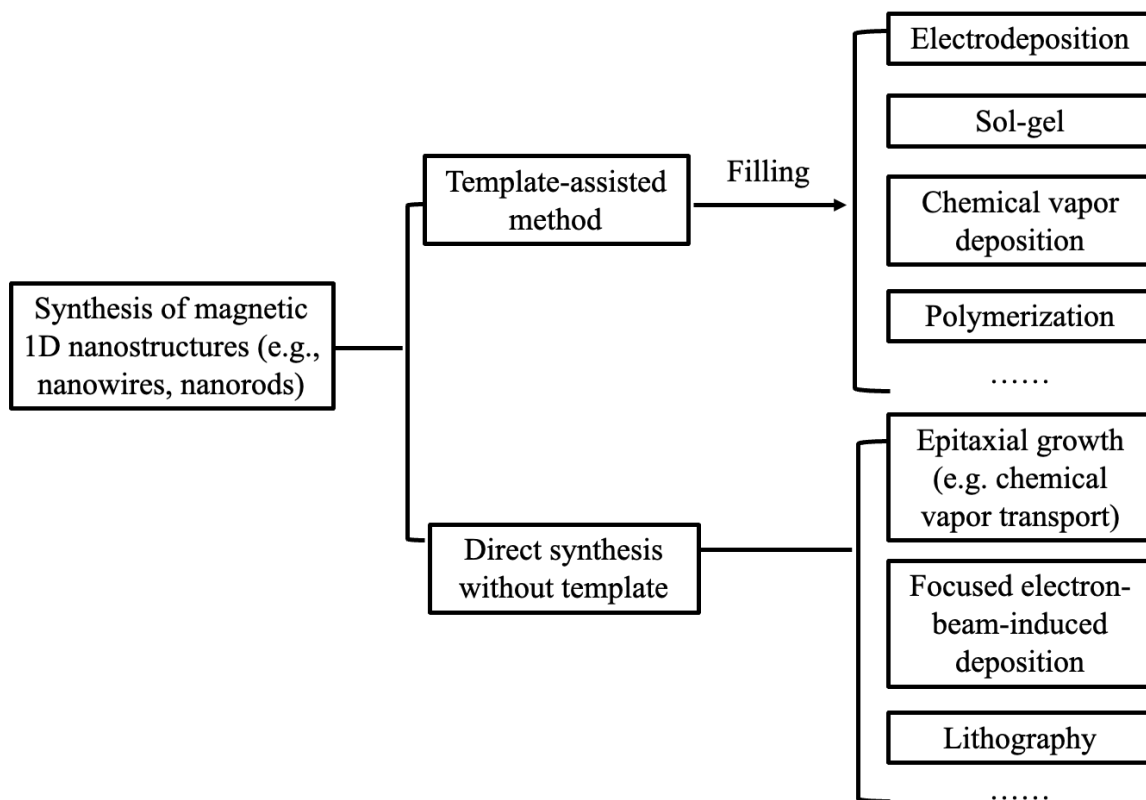
Figure 1.3. A general scheme of various synthetic techniques to fabricate 1D magnetic nanostructures

Experimental techniques to fabricate low-dimensional magnetic nanostructures (e.g., 1D nanowires or 2D thin films) can be divided up into two approaches: bottom-up or top-down approach. As the name suggests, the former approach starts with tiny building blocks (e.g., atoms, molecules) and lets these assemble to form a nanostructure with designed dimensionality spontaneously. On the other hand, the latter approach starts with large structures and employs shrinking of these *via* exfoliation until the desired nanostructures remain.

To the best of our knowledge, the top-down approach has been rarely, if ever, applied to fabricate magnetic nanowires, and the state-of-the-art techniques to obtain ultrathin magnetic nanowires are focused on bottom-up synthesis. These techniques can be roughly categorized into two categories: template-directed synthesis and template-free direct patterning/synthesis (**Figure 1.3**). Within each category, there are various methods to synthesize magnetic nanowires with the

target compositions and morphologies, but each category of synthetic techniques also suffers complications and limitations.

Template-based deposition is by far the most commonly employed technique to obtain magnetic nanowires, nanotubes, or core-shell nanowires. The essence of this technique is to synthesize or deposit the target magnetic materials inside the pores of nanoporous templates, which are usually alumina membranes with desired sizes and geometric arrangement of nanochannels. Because the synthetic or deposition process is confined within 1D nano-channels of the template membranes, it can produce freestanding nanowires or nanoribbons at a large scale with low cost after removing the template membrane.

To fill the template, various strategies have been explored (**Figure 1.3**). A widely used technique is electrodeposition, which involves an electrochemical process by which the metallic ions from an electrolyte are reduced to form a solid deposit in the cathode (i.e., the anodic alumina template) in the form of nanowires. This technique has been employed to build homogeneous magnetic metallic nanowires based on a wide compositional range of transition metals and their alloys with diverse diameters and lengths, as well as to fabricate multisegmented nanowires modulated in geometry or composition along their length.[32] An alternative strategy to fill the 1D channels of templates for nanowire production is the sol-gel technique, which is particularly suitable for fabricating nanowires of magnetic oxides such as ferrites or multiferroic perovskites. The sol-gel growth starts with forming colloidal nanoparticles by mixing atomic or molecular prosecutors, which are then interconnected within the pores of templates and solidified to form nanowires or nanotubes.[33-34] In addition, template-directed autocatalytic deposition, which relies on the chemical reduction of metallic ions from solutions, is also a common method to fill the 1D channels within the templates with a variety of magnetic materials, including metals, alloys, and oxides, for magnetic nanowire productions.[35]

These template-assisted methods have revolutionized the production of magnetic nanowires. The accurate control of all parameters during the synthetic processes, such as the type and concentration of molecular precursors, temperature, electrodeposition potential, PH, and solvents, together with the template, allows for the fabrication of magnetic nanowires with finely tailored structural, morphological, and magnetic features, which further enables the implementation of these nanowires in technological applications. However, these methods suffer from limitations (**Figure 1.4**). Firstly, it remains challenging and sophisticated to create templates with high-quality 1D channels that have ultrathin diameters, high aspect ratio, uniform morphologies along the channel, and smooth inside surfaces. As a result, the fabricated nanowires based on these templates may have low aspect ratio, surface kinking or tampering, cone or dumbbell-shape geometries, small branching, and rough surfaces. These structural defects can significantly affect the long-range ordering, anisotropic behaviors, and potential interfacial interactions of these nanowires. Therefore, the as-fabricated nanowires can exhibit significant deviation from the magnetic 1D nature and poorly controlled magnetic properties, which hinder their applications in highly precise nanodevices. Secondly, due to the restraints imposed by templates during the filling and the rapidity of deposition processes, the reactions happening inside the 1D channels are not under equilibrium, so the magnetic nanowires so produced sometimes may not be highly crystalline and can have local crystal inhomogeneities. The poor crystallinity, polycrystallinity, and poorly controlled crystalline orientations along the nanowires can induce local strains and grain boundaries, significantly damage the idealness of 1D transport and magnetic properties and decrease the mechanical strength of these nanostructures.
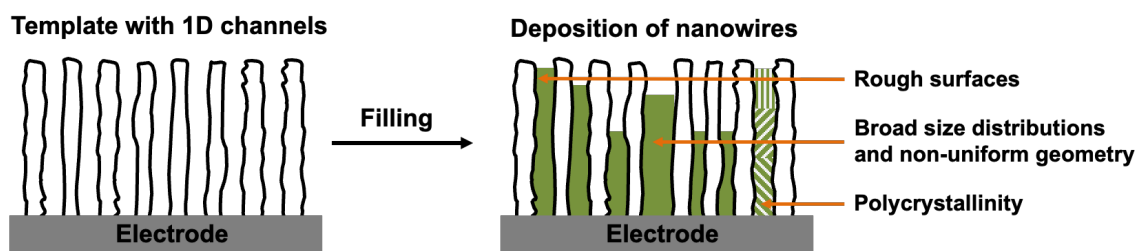

Figure 1.4. A schematic illustration of templated-assisted techniques to produce nanowires and an exaggerated view of some limitations of template-directed grown nanowires

17

The fabrication difficulties of templates and the non-equilibrium nature of the filling process can be circumvented with the template-free direct synthesis strategies. Many methods mentioned above to synthesize nanowires within the 1D channels of templates can also be used to fabricate magnetic nanowires on template-free substrates or in solutions, such as the sol-gel technique and the autocatalytic deposition. Other commonly used direct fabrication methods of magnetic nanowires include epitaxial growth such as chemical vapor deposition (CVD), focused electron-beam-induced deposition (FEBID), and electron-beam lithography, which are briefly introduced below.

Epitaxial growth typically refers to the growth of nanostructures utilizing the lattice match between the material to be grown and the substrate. One commonly used method to epitaxially grow various magnetic nanowires is the CVD technique, especially the vapor-liquid-solid (VLS) growth. Originally developed to fabricate semiconducting nanowires, the VLS process starts with a catalyst (usually Au) forming a eutectic with the growing material, which then initiates the growth of the magnetic nanowires. This technique is particularly useful for preparing Si-based nanowires containing ferromagnetic metals such as Fe and Co and/or Mn.[36] Another valuable method to epitaxially fabricate various magnetic nanowires vertically or laterally on substrates is the CVT process, during which a gas phase intermediate generated by heating a mixture of solid source materials is transported and deposited at the temperature stabilizing the interfacial energy of the substrate. Subsequently, the gas intermediate grows into nanowires. The CVT technique has been employed to fabricate metal or intermetallic magnetic nanowires, such as Ni nanowires, Co nanowires, and nanowires of NiCo, CoFe, and NiFe alloys, together with semiconductor-based magnetic nanowires. For example, with FeI_2 being heated on one end of the furnace as the Fe source and Ge/carbon powder seated on the other end as the Ge source, vertically aligned magnetic $Fe_{1.3}Ge$ nanowires can be grown on graphene substrate placed on the Ge/carbon mixture.[37]

Electron-beam lithography and focused electron beam induced deposition (FEBID) are lithography techniques that allow for direct writing or patterning of 1D nanostructures with electron beam, which usually offers better control over the structural features of magnetic nanowires compared to conventional epitaxial growth or template-directed electrodeposition. The most common electron-beam lithography starts with large structures of the targeted material and shrinking these structures *via* etching, cutting, or removing other parts until the desired 1D nanostructures remain. This technique is typically used to prepare pattered nanostrips or nanowires

lying on the surface of a substrate but is not suitable for preparing vertical or freestanding magnetic nanowires with large aspect ratio, due to the technical difficulty with vertical deep-etching or coating. Direct writing assisted by focused electron beam, i.e., FEBID, allows for higher preparation flexibility, especially for vertical structures. The typical FEBID technique relies on the dissociation of injected gaseous metal-containing precursors absorbed on a substrate to deposit metal nanowires, after which further purification is needed to remove the undesirably deposited elements. FEBID is more suitable for producing purely metallic nanowires such as Co and Fe nanowires or nanowires with core-shell structures such as Co nanowires covered with Pt.[36]

However, these direct fabrication methods also have limitations. Firstly, although the direct patterning improves control over the crystallinity and crystalline orientation, it remains challenging to control the phase purity and morphology of the prepared nanowires. For example, the nanowires grown from VLS methods may have the catalyst nanoparticle such as Au attaching to one end of them, which may interfere with the fabrication of the spintronic devices based on these nanowires and be detrimental to their performance. The nanowires produced by FEBID may contain a non-negligible amount of carbon co-deposited with the metals, affecting their magnetic behaviors and electronic properties. Secondly, such direct patterning techniques usually require highly sophisticated instruments, are extremely time-consuming, and have low throughput. In addition, the dangling bonds due to the broken symmetry on the surfaces of these nanostructures can lead to strong interactions with substrates and local interfacial strains, which may even induce non-intrinsic magnetic orderings or anisotropies within the magnetic nanostructures. As a result, it remains challenging to precisely control or even predict the properties and performances of the resulting magnetic 1D nanostructures, which significantly hinders their large-scale technological applications.

1.4.2 Synthesis of 3D Compounds with 1D Magnetic Motifs

While accessing magnetic solids with 1D morphologies, 1D confinement effects, and unidirectional transport behaviors at the nanoscale (e.g., magnetic nanowires) has been a popular approach to investigating the effects of low dimensionality on magnetism and developing densely-packed spintronic devices, there have also been growing efforts to study the 1D magnetism and its coupling with other physical properties in structurally 3D crystals, which can provide the sufficient intensity and size for experiments investigating thermal properties (e.g., specific heat) and dynamic behaviors (particularly quantum excitations) by bulk techniques such as neutron scattering. For this purpose, people have sought to synthesize various structurally 3D magnetic materials where the magnetic ions are arranged in chains well separated by bulky nonmagnetic groups of atoms.
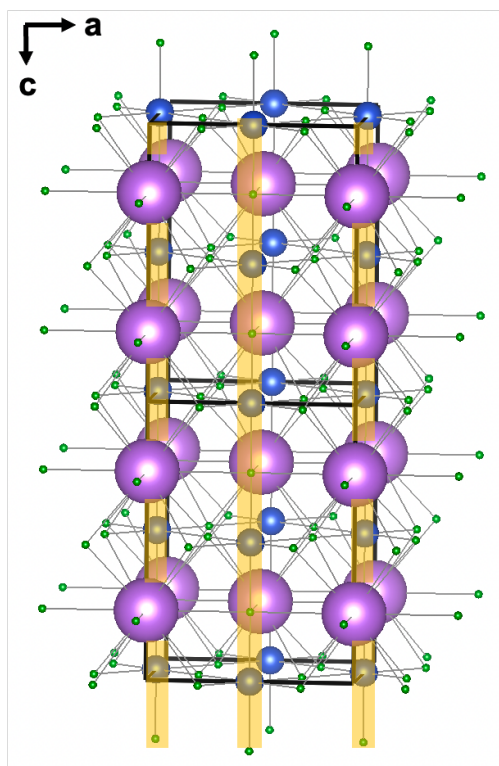

Figure 1.5. Crystal structure of $KCuF_3$ with the 1D magnetic Cu–F–Cu chains highlighted in yellow. Blue, violet, and green spheres represent Cu, K, and F, respectively. The ionic radii of different elements are modified disproportionally for clarity and illustration.

Under certain approximations, the reasonably short magnetic exchange couplings only exist along these 1D chains (see **Figure 1.5** for illustration) and consequently, the 3D crystals are defined as 1D magnets. These 1D magnetic solids have provided a unique possibility to study ground and excited states of low-dimensional magnets, possible new phases of maters and new theories of magnetism, and the interplay of quantum fluctuation and thermal fluctuation.[38-41]

One big class of such materials has the formula of ABX_3, with A being a large and nonmagnetic monovalent cation, B being a divalent *3d* transition metal ion, and X being halide. For example, $(CH_3)_4NMnCl_3$, also known as TMMC, is among the most ideal 1D magnetic crystal yet studied, in which the interchain coupling strength is at least three orders of magnitude smaller than the intrachain exchange coupling. As a result, it has an extremely low ordering temperature (T_C = ~0.8 K) and exhibits 1D dynamic behaviors in inelastic neutron scattering.[42] Such single-chain magnets are extremely useful for studying quantum effects, especially those magnets featuring Cu^{2+} ions which realize spin-$\frac{1}{2}$ or Ni^{2+} ions that realize spin 1. For example, $KCuF_3$ (**Figure 1.5**) has been among the best realizations of the spin-$\frac{1}{2}$ antiferromagnetic Heisenberg model,[43] and $CsNiF_3$ is particularly important as a ferromagnetic XY-like chain that allows for the demonstration of magnetic solitons.[44]

Despite their unique values in investigating dynamic behaviors and testing quantum models, the single-chain magnetic solid systems mentioned above, as indicated by the Mermin-Wagner theorem, usually have very weak long-range ordering, which hinders the studies of the long-range physical properties of magnetic systems with 1D nature. As a result, magnetic solids with 1D nature together with robust long-range magnetic ordering are warranted. For this purpose, the intermediate states between 1D and 2D magnets, namely quasi-1D magnets, featuring two or three magnetic chains lying close together (i.e., spin ladders), have been intensively investigated over
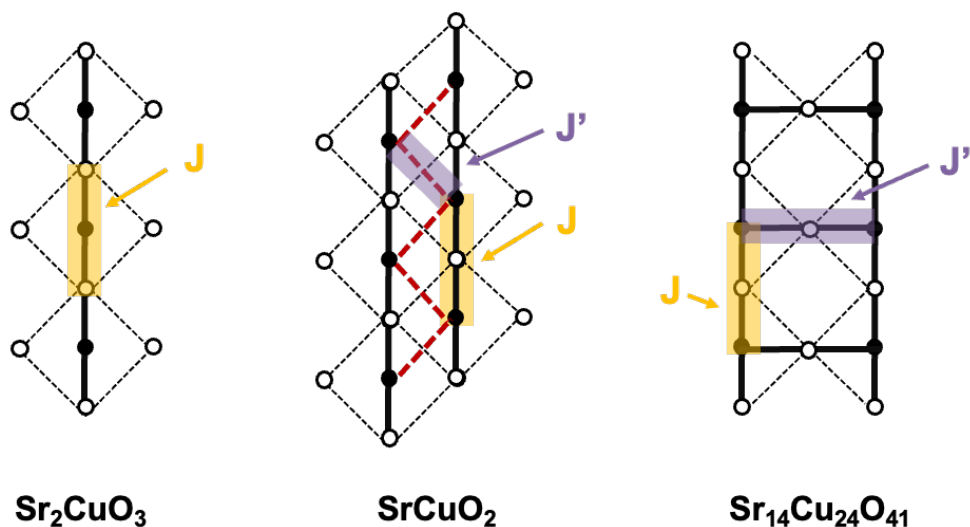
Figure 1.6. The schematic view of the 1D or quasi-1D Cu–O chains in three representative phases belonging to the SrCuO class. Potential competing magnetic interactions within each spin-chain or spin-ladder are highlighted in yellow and purple.

the past decades and have significantly facilitated the discovery and investigation of novel physical behaviors. For example, $CuGeO_3$, a quasi-1D spin-$\frac{1}{2}$ antiferromagnet, is the first inorganic material showing spin-Peierls distortion.[45-46] The class of SrCuO phases featuring a mixture of ladders two-leg and multi-leg ladders with competing interactions, such as $SrCu_2O_3$ and $Sr_{14}Cu_{24}O_{41}$, [47-50] has been crucial to realizing and understanding superconductivity (**Figure 1.6**). In addition to these efforts, people have been actively developing 1D or quasi-1D molecular magnetic systems with bulky organic spacers or metal-organic frameworks (MOFs) with separated magnetic chains or ladders locked in the 3D rigid framework.[51]

However, these 3D crystals with 1D or quasi-1D magnetic units are not structurally 1D, which may raise problems. From the theoretical point of view, potential magnetic exchange pathways through nonmagnetic separators are still possible and can break the "ideal" 1D magnetism. For technological applications, the strong ionic or covalent interactions between magnetic units in these phases complicate their structural miniaturization and potential nanocomposite fabrication, hindering their applications as spintronics or sensors at the nanoscale. Therefore, we need to develop a new 1D magnetic material system which minimizes the magnetic

exchange coupling between the 1D magnetic units and allows for straightforward miniaturization to produce nanowires. Not only are such materials (bulk and the miniaturized nanowires) better candidates in terms of both definitions, but they also allow the study of the true crossover of magnetism from 3D to 1D with the same phase, both with bulk techniques and at nanoscale.

1.5 Lessons from 2D van der Waals Magnets to Improve Current 1D Magnetic Systems

To access 1D magnetic solids possessing ideal 1D magnetism in bulk and allowing for straightforward miniaturization to prepare high-quality magnetic nanowires, we can draw important inspirations and lessons from the development history of 2D magnetic systems. Similar to the history of accessing 1D magnetic solids mentioned in **1.4**, the investigation of 2D magnetic systems has also shown two categories of approaches. The first approach is to grow ultra-thin magnetic films, where many finite-size effects emerge, and physical properties unique to 2D systems can be observed and studied.[52] But despite decades of development, such 2D magnetic nanostructures suffer from problems just like the bottom-up synthesized magnetic nanowires. It remains sophisticated and challenging to precisely control the thicknesses, morphologies, and crystallinities of the resulting nanostructures, which is further complicated by their surface dangling bonds and their strong interactions with substrates or environments. The second approach is to grow 3D crystals with non-magnetic spacers between 2D magnetic sheets, and this has enabled the study of novel physical systems such as the Kagome lattice.[53] However, similar to the 1D spin-chain or quasi-1D spin-ladder systems discussed in **1.4.2**, these so-called 2D magnetic lattices still exhibit inter-plane magnetic couplings and derivation from ideal 2D magnetic behaviors, and the strong ionic or covalent interactions between the 2D magnetic planes prevent efficient structural miniaturization necessary for the production of thin-film spintronics.
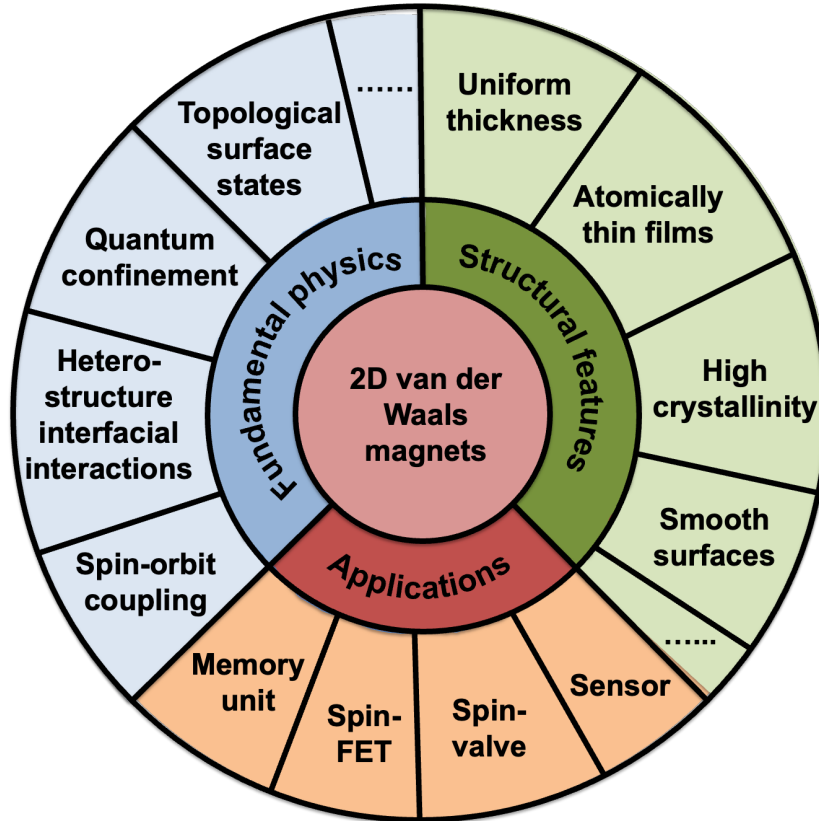
Figure 1.7. A brief summary of the structural features of the 2D magnetic thin films produced by top-down exfoliation of 2D vdW materials and the values of these thin films for fundamental study and device application.

Despite the constant efforts to optimize the growth techniques and the design of magnetic crystals, these limitations remained until the revolutionary discovery and the advent of top-down exfoliation of 2D layered van der Waals (vdW) crystals. By utilizing "empty spaces" (i.e., vdW gaps) to isolate the 2D magnetic layers in 3D crystals, interlayer superexchange coupling pathways can be entirely ruled out due to the lack of any interlayer covalent bonds or ionic interactions. Direct exchange coupling is also suppressed to a negligible level due to the large interlayer distance and the minimal direct orbital overlaps between magnetic ions in adjacent layers. As a result, the bulk crystals of such 2D vdW magnets can be viewed as "ideal" 2D systems and provide a clearer system to test theoretical models on 2D magnetism. Even more encouragingly, due to the vdW nature of the interlayer interactions, such materials allow for the isolation of nanostructures with uniform thickness down to a single atomic layer, with well-defined surfaces and atom-precise

termination, which further allow for the investigation of nanoscale 2D confinement effects and the low-cost fabrication of thin-film spintronic devices. In addition, due to the naturally layered structure and high crystallinity of these 2D vdW magnets, the 2D thin films resulted from their exfoliation couple weakly to substrate and exhibit very low surface strains. As a result, they can also be efficiently integrated into nanoscale heterostructures, which significantly increases their values for fundamental studies and technological applications (**Figure 1.7**).[54]

First efforts to realize 2D vdW magnets were carried out in the early 1980s, with the synthesis of layered transition-metal thiophosphates MPS_3, where M is a first-row transition metal such as Mn, Fe, and Ni and forms a 2D honeycomb magnetic sublattice.[55] Later, the vdW nature of these magnetic phases was further explored by intercalating guest molecules or ions between the magnetic layers and using intercalation to alter the magnetic properties of the bulk crystal.[56] The earliest efforts towards the exfoliation of magnetic 2D materials were carried out in 2016 with the isolation of monolayer and few-layer forms of $NiPS_3$ and $FePS_3$. Raman measurement provides (albeit only indirectly) evidence that the bulk magnetism is preserved in these thin exfoliated crystals.[57] The revolutionary breakthrough occurred in 2017 when the first realization of magnetism was confirmed with clear and direct experimental evidence in atomically thin CrI_3 and $Cr_2Ge_2Te_6$ down to the mono- and bilayer limit.[58-59] This ground-breaking discovery has sparked intense interest and activities in expanding the scope of 2D vdW magnetic materials, optimizing the exfoliation techniques to obtain mono- or multilayer thin films, and investigating the physical properties of these atomically thin 2D magnetic structures. So far, several classes of 2D vdW magnets have been synthesized and exfoliated, with a diverse range of properties being observed and a variety of functional devices being developed. The first class is the chromium-based compounds, including $Cr_2Ge_2Te_6$, CrI_3, $CrBr_3$, $CrCl_3$, and $CrSiTe_3$. These materials exhibit different types of inter-layer and intra-layer magnetic coupling and consequently exhibit layer-dependent magnetic behaviors, which can be modulated by moving the electrons between layers *via* gate voltage. This paves a unique pathway to study the magnetoelectric control and spintronics of 2D atomically thin magnets and fundamentally understand the interplay between electronic and magnetic properties. Other 2D vdW magnets include Fe_3GeTe_2, which has strong magnetocrystalline anisotropy and magnetostrictive effect, 1T VSe_2 and 1T-VS_2, which, when exfoliated into a few layers, possess room temperature ferromagnetic ordering, and the above-mentioned NPS_3 and $NPSe_3$ (M = Mn, Fe, or Ni) class, which exhibit antiferromagnetic ordering

maintained in monolayer and may show superconductivity, although further confirmations are still warranted.[60]

The field of 2D vdW magnetic materials has just started, but the experimental results already reported have provided powerful solutions to many challenges in fabricating 2D magnetic nanostructures and developing platforms to study 2D magnetism, which have given us a glimpse of how fertile the research domain is, as opened by the discovery and exfoliation of these 2D vdW magnets. This also offers great inspiration for the development of 1D magnetic materials. To address challenges mentioned in **1.4** and to deepen the understanding of vdW bonding in crystals, we seek to study solid-state crystalline phases that possess the same vdW structural attributes as that of 2D vdW phases but, instead of being comprised of sheets, are made of sub-nanometer inorganic chains that are held by very weak vdW interactions (i.e., 1D vdW materials) (**Figure 1.8**). Such structural features, if combined with well-controlled magnetic properties, would enable us to build nearly ideal platforms to study 1D magnetism, access ultra-thin magnetic nanowires for technological applications, and in turn, help us to understand the crossover of magnetism from 3D to 2D, and to 1D.
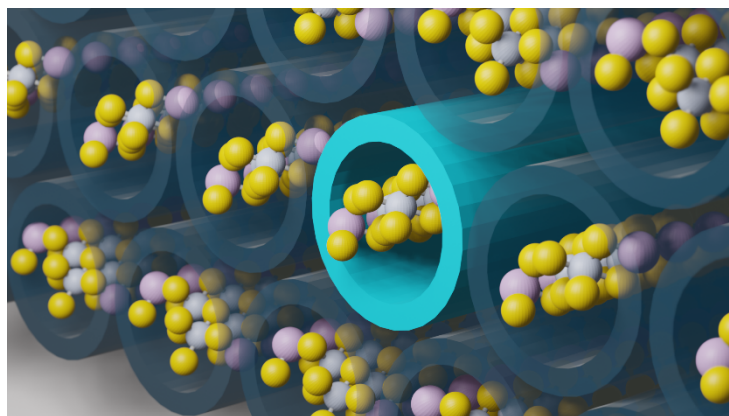

Figure 1.8. A cartoon illustration of the concept of 1D vdW materials, where covalently bonded 1D chains are stacked and separated by weak vdW interactions.

1.6 Exfoliation of 1D van der Waals Phases for Electronic and Optical Applications

Prior to this thesis work, top-down exfoliation of 1D vdW lattices, including solution exfoliation by sonication and mechanical exfoliation by adhesive tapes, have not been employed to produce 1D magnetic nanostructures yet, but they have been developed to obtain 1D nanowires for electronic and optical applications. With these nanowires, the crossover of electronic or optical properties from 3D to 1D has also been studied. These explorations have offered valuable insights into the mechanism of exfoliation and are an inspiring starting point towards the top-down fabrication of 1D magnetic nanostructures.

The essence of solution exfoliation of 1D vdW crystals is the breakdown of the vdW interactions and dispersion of the exfoliated nanomaterials in solvent (**Figure 1.9**). Such processes are highly dependent on the wetting behavior and the binding energy between the solvent and the material surface. Among various properties of solvents, the polarity affects the binding energy between the solid surface and the liquid through dipole-dipole interactions, and the dispersity affects the wetting behaviors. As a result, by optimizing the solvent with respect to the vdW material of interest, people have successfully exfoliated various 1D magnetic nanostructures using simple solvent systems.[61] For example, MoSI nanowires with the formula of $Mo_6S_{9-x}I_x$ (typically $4 \leq x \leq 6$) down to less than 1nm thin can be prepared by sonicating the as-synthesized bulk crystals within in isopropanol.[62] Similarly, V_2Se_9 and Nb_2Se_9, both featuring covalently bonded chains connected by weak inter-chain vdW interactions, can be easily exfoliated into nanowires with ~ 1nm diameter by sonication in isopropanol or acetone.[63-64] In addition, 1D vdW crystals, including Ta_2NiSe_7, Sb_2Se_3, and Nb_2Se_9, can be mechanically cleaved into nanowires by adhesive tapes.[65]
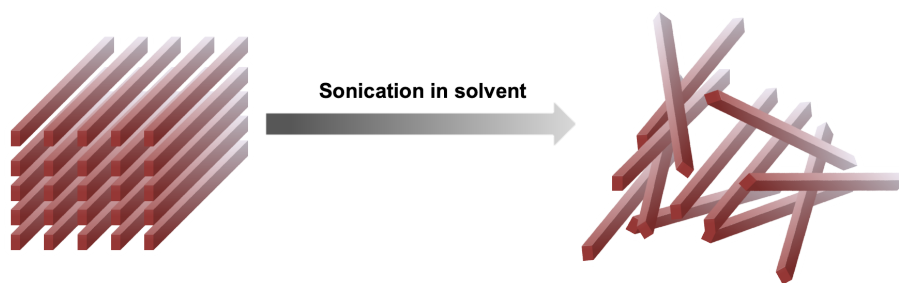

Figure 1.9. A conceptual illustration of solution exfoliation process of 1D vdW lattices

It is crucial to distinguish the exfoliation methods mentioned in the preceding paragraphs from the solution stabilization of 1D ionic lattice with polar organic solvents, which is also called "exfoliation" in many literature. The solution stabilization involves bulk materials that are 1D ionic lattices with anionic 1D chains separated by group I or group II cations, and a polar medium such as highly polar organic solvents that can solvate the cation and then allow the anionic chains to be isolated by the electrostatic repulsion forces between the chains. One representative demonstration of this method is the solvation of $LiMo_3Se_3$ into chains with less than 5nm diameters using *N*-methylformamide and dimethyl sulfoxide.[66] Because of the existence of counter ions on the surface of the negatively charged nanowires, these 1D nanostructures are much more sensitive to air or water and less stable than the nanowires produced by cleaving vdW gaps. In addition, these ionic nanowires can have strong interactions with substrate and local structural defects, which are much more challenging to manipulate or be incorporated into functional devices than the exfoliated nanowires resulting from vdW crystals.

1.7 1D van der Waals Magnetic Materials

Although people have intensively investigated the 2D vdW magnets and have developed efficient strategies to exfoliate 1D vdW crystals, to our knowledge, very few groups have studied 1D vdW magnetic systems, and these 1D top-down exfoliation techniques have not been extended to magnetic vdW phases to access highly desirable ultrathin magnetic nanowires. To fill this gap, we first need to identify 3D bulk crystals with our desired structural features and magnetic properties and use them as the precursors for top-down exfoliation. In addition, we also need to explore strategies to efficiently control the magnetic properties of the bulk 1D vdW crystals so that a diverse library of 1D vdW magnetic phases can be achieved. Such a broadened scope of material candidates will offer us more opportunities to optimize the top-down exfoliation techniques and achieve various magnetic behaviors within the exfoliated nanowires.

Prior to this thesis work, only two classes of 1D vdW magnetic solids had been reported. One class has the formula of $CrSbCh_3$ (Ch = Se and S), which features double-rutile chains of Cr (III) separated by weak vdW interactions (**Figure 1.10**). $CrSbSe_3$ was first synthesized in 1997 and reported as a ferromagnet with long-range ordering,[67-68] although no magnetic structure was reported before our work. $CrSbS_3$ was first synthesized in 1994 with contradictory claims on its magnetic ordering being reported.[69-71] Another class of isostructural 1D vdW magnets has the formula of MPn_2Ch_4 (M = Mn, Fe, Pn = Sb, Bi, and Ch = S, Se), which features single-rule chains of the magnetic metal ions separated by vdW gaps (**Figure 1.10**). For phases within this class, the dominant magnetic ordering depends strongly on the nature of the magnetic atom (Mn, Fe) lying in the center of the 1D chains and the dominant charge carrier type (electrons or holes) can be
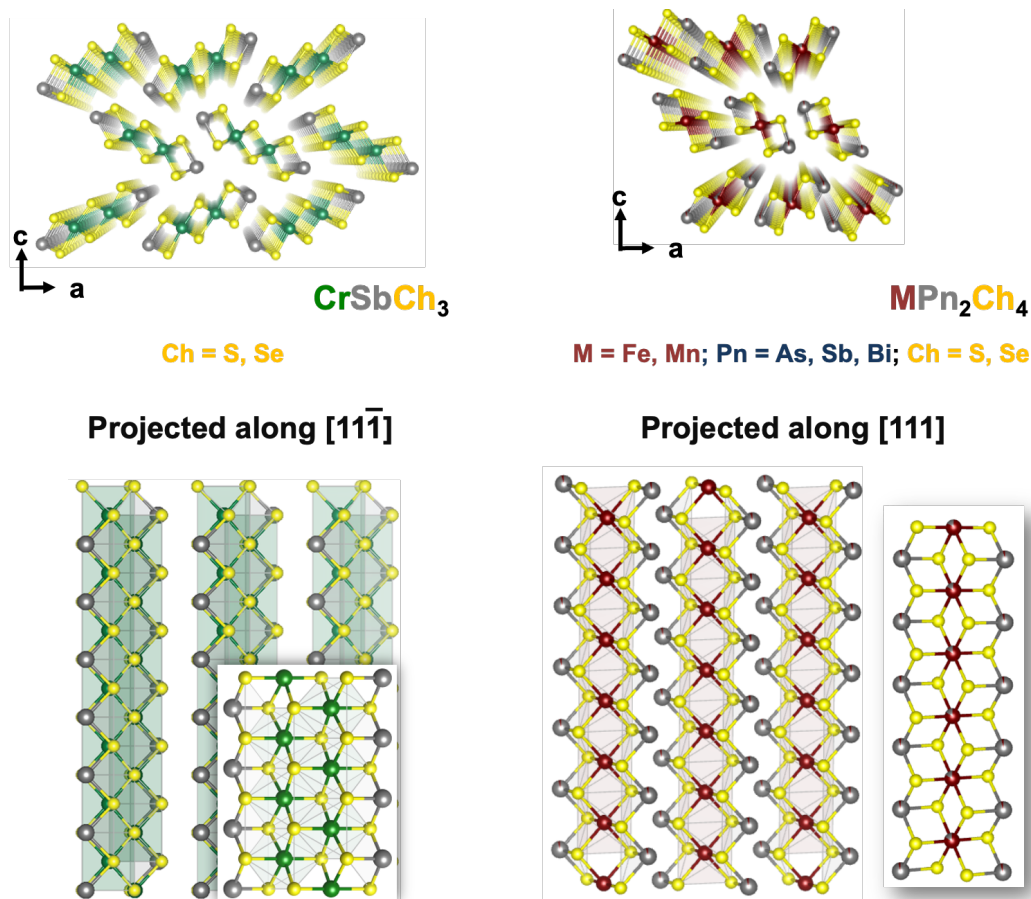

Figure 1.10. Crystal structures and the structures of 1D unit of the two classes of 1D vdW magnetic phases reported before this thesis work.

manipulated by the nature of the Pn atoms on the edge of the 1D chains. For example, $FeSb_2Se_4$ has been reported to be a ferromagnet, while $MnSb_2Se_4$ is an antiferromagnet. P-type semiconduction behavior was observed in $MnSb_2Se_4$ and $FeSb_2Se_4$, while the Bi analog $MnBi_2Se_4$ and $FeBi_2Se_4$ exhibit n-type behaviors.[72-76] However, due to the low spin moments on Fe (II) and the antiferromagnetic coupling between Mn (II), weaker magnetization is observed for this class of 1D vdW magnets compared to the $CrSbCh_3$ class. In addition, we expect a relatively weaker long-range magnetic ordering in MPn_2Ch_4 phases because of the single-chain nature of each 1D magnetic unit, in contrast to the spin-ladder connections within the $CrSbCh_3$ class. With this in mind, we started from phases belonging to the $CrSbCh_3$ class, developed top-down methods to exfoliate these phases for nanowire production, and significantly broadened the scope of materials belonging to this class. Details of these results will be discussed in the following chapters.

References

(1) Haldane, F. D. M., Continuum dynamics of the 1-D Heisenberg anti-ferromagnet – Identification with the O(3) non-linear sigma-model. *Phys. Lett. A* **1983,** *93* (9), 464-468.

(2) Dagotto, E.; Rice, T. M., Surprises on the way from one- to two-dimensional quantum magnets: The ladder materials. *Science* **1996,** *271* (5249), 618-623.

(3) Gnezdilov, V.; Lemmens, P.; Pashkevich, Y. G.; Wulferding, D.; Morozov, I. V.; Volkova, O. S.; Vasiliev, A., Dynamical lattice instability versus spin liquid state in a frustrated spin chain system. *Phys. Rev. B* **2012,** *85*, 214403.

(4) Goodenough, J. B., Theory of the role of covalence in the perovskite-type manganites [La, *M*(II)]MnO$_3$. *Phys. Rev.* **1955,** *100* (2), 564-573.

(5) Kanamori, J., Superexchange interaction and symmetry properties of electron orbitals. *J. Phys. Chem. Solids* **1959,** *10* (2-3), 87-98.

(6) Lee, S.; Pirogov, A.; Kang, M. S.; Jang, K. H.; Yonemura, M.; Kamiyama, T.; Cheong, S. W.; Gozzo, F.; Shin, N.; Kimura, H.; Noda, Y.; Park, J. G., Giant magneto-elastic coupling in multiferroic hexagonal manganites. *Nature* **2008,** *451* (7180), 805-808.

(7) Li, H.; Chen, Z.; Polinder, H., Optimization of multibrid permanent-magnet wind generator systems. *IEEE Trans. Energy Convers.* **2009,** *24* (1), 82-92.

(8) Strnat, K. J., Modern permanent magnets for applications in electro-technology. *Proc. IEEE* **2002**, *78* (6), 923-946.

(9) White, R. L., Giant magnetoresistance - a primer. *IEEE Trans. Magn.* **1992,** *28* (5), 2482-2487.

(10) Parkin, S. S. P., Hayashi, M., Thomas, L., Magnetic domain-wall racetrack memory. *Science* **2008**, *320* (5873), 229-255.

(11) Hase, M.; Kuroe, H.; Ozawa, K.; Suzuki, O.; Kitazawa, H.; Kido, G.; Sekine, T., Magnetic properties of $Rb_2Cu_2Mo_3O_{12}$ including a one-dimensional spin-1/2 Heisenberg system with ferromagnetic first-nearest-neighbor and antiferromagnetic second-nearest-neighbor exchange interactions. *Phys. Rev. B* **2004,** *70*, 104426.

(12) Christian, A. B.; Masunaga, S. H.; Schye, A. T.; Rebello, A.; Neumeier, J. J.; Yu, Y. K., Magnetic field influence on the Neel, dimer, and spin-liquid states of the low-dimensional antiferromagnets $NiTa_2O_6$ and $CoSb_2O_6$. *Phys. Rev. B* **2014,** *90*, 224423.

(13) Wu, L. S.; Nikitin, S. E.; Wang, Z.; Zhu, W.; Batista, C. D.; Tsvelik, A. M.; Samarakoon, A. M.; Tennant, D. A.; Brando, M.; Vasylechko, L.; Frontzek, M.; Savici, A. T.; Sala, G.; Ehlers, G.; Christianson, A. D.; Lumsden, M. D.; Podlesnyak, A., Tomonaga-Luttinger liquid behavior and spinon confinement in $YbAlO_3$. *Nat. Commun.* **2019,** *10*, 698.

(14) Christensen, N. B.; McMorrow, D. F.; Ronnow, H. M.; Lake, B.; Hayden, S. M.; Aeppli, G.; Perring, T. G.; Mangkorntong, M.; Nohara, M.; Takagi, H., Dispersive excitations in the high-temperature superconductor $La_{2-x}Sr_xCuO_4$. *Phys. Rev. Lett.* **2004,** *93*, 147002.

(15) Kimber, S. A. J.; Mutka, H.; Chatterji, T.; Hofmann, T.; Henry, P. F.; Bordallo, H. N.; Argyriou, D. N.; Attfield, J. P., Metamagnetism and soliton excitations in the modulated ferromagnetic Ising chain CoV_2O_6. *Phys. Rev. B* **2011,** *84*, 104425.

(16) MacIsaac, A. B.; Whitehead, J. P.; DeBell, K.; Poole, P. H., Phase diagram for a magnetic thin film with dipolar interactions and magnetic surface anisotropy. *Phys. Rev. Lett.* **1996,** *77* (4), 739-742.

(17) Rossler, U. K.; Bogdanov, A. N.; Pfleiderer, C., Spontaneous skyrmion ground states in magnetic metals. *Nature* **2006,** *442* (7104), 797-801.

(18) Fert, A.; Cros, V.; Sampaio, J., Skyrmions on the track. *Nat Nanotechnol.* **2013,** *8* (3), 152-156.

(19) Ising, E., Report on the theory of ferromagnetism. *Z. Phys.* **1925,** *31*, 253-258.

(20) Heisenberg, W., On the Theory of Ferromagnetism. *Z. Phys.* **1928,** *49* (9-10), 619-636.

(21) Onsager, L., Crystal statistics I A two-dimensional model with an order-disorder transition. *Phys. Rev.* **1944,** *65* (3-4), 117-149.

(22) Mermin, N. D.; Wagner, H., Absence of ferromagnetism or antiferromagnetism in one- or two-dimensional isotropic Heisenberg models. *Phys. Rev. Lett.* **1966,** *17* (22), 1133-1136.

(23) Fisher, M. E., The perpendicular susceptibility of an anisotropic antiferromagnet. *Physica* **1960,** *26* (8), 618-622.

(24) Barnes, T.; Dagotto, E.; Riera, J.; Swanson, E. S., Excitation spectrum of Heisenberg spin ladders. *Phys. Rev. B* **1993,** *47* (6), 3196-3203.

(25) White, S. R.; Noack, R. M.; Scalapino, D. J., Resonating valence-bond theory of coupled Heisenberg-chains. *Phys. Rev. Lett.* **1994,** *73* (6), 886-889.

(26) Noack, R. M.; White, S. R.; Scalapino, D. J., Correlations in a two-chain Hubbard-model. *Phys. Rev. Lett.* **1994,** *73* (6), 882-885.

(27) Azzouz, M.; Chen, L.; Moukouri, S., Calculation of the Singlet-triplet gap of the antiferromagnetic Heisenberg-model on a ladder. *Phys. Rev. B* **1994,** *50* (9), 6233-6237.

(28) Buschow, K. J.; De Boer, F. R. *Physics of Magnetism and Magnetic Materials*; Springer, **2003**; pp 105−128.

(29) Cullity, B. D.; Graham, C. D. *Introduction to Magnetic Materials*; John Wiley & Sons, **2011**; pp 369−371

(30) Nakajima, N.; Koide, T.; Shidara, T.; Miyauchi, H.; Fukutani, I.; Fujimori, A.; Iio, K.; Katayama, T.; Nyvlt, M.; Suzuki, Y., Perpendicular magnetic anisotropy caused by interfacial hybridization *via* enhanced orbital moment in Co/Pt multilayers: magnetic circular x-ray dichroism study. *Phys. Rev. Lett.* **1998,** *81* (23), 5229-5232.

(31) Pal, S.; Rana, B.; Hellwig, O.; Thomson, T.; Barman, A., Tunable magnonic frequency and damping in [Co/Pd]$_8$ multilayers with variable Co layer thickness. *Appl. Phys. Lett.* **2011,** *98* (8), 082501.

(32) Vezquez, M., Ed. *Magnetic Nano- and Microwires: Design, Synthesis, Properties and Applications*; Woodhead Publishing, **2015**; pp 43-70.

(33) Vezquez, M., Ed. *Magnetic Nano- and Microwires: Design, Synthesis, Properties and Applications*; Woodhead Publishing, **2015**; pp 112-115.

(34) Stano, M.; Fruchart, O.; Bruck, E., Chapter 2-Magnetic Nanowires and Nanotubes. In *Handbook of Magnetic Materials*, Elsevier: Amsterdam, **2018**; Vol. 27, pp 11-12.

(35) Vezquez, M., Ed. *Magnetic Nano- and Microwires: Design, Synthesis, Properties and Applications*; Woodhead Publishing, **2015**; pp 479.

(36) Stano, M.; Fruchart, O.; Bruck, E., Chapter 2-Magnetic Nanowires and Nanotubes. In *Handbook of Magnetic Materials*, Elsevier: Amsterdam, **2018**; Vol. 27, pp 10-11.

(37) Yoon, H.; Kang, T.; Lee, J. M.; Kim, S. I.; Seo, K.; Kim, J.; Won, I.; Kim, B., Epitaxially integrating ferromagnetic $Fe_{1.3}Ge$ nanowire arrays on few-layer graphene. *J. Phys. Chem. Lett.* **2011,** *2* (9), 956-960.

(38) Kohno, M.; Starykh, O. A.; Balents, L., Spinons and triplons in spatially anisotropic frustrated antiferromagnets. *Nat. Phys.* **2007,** *3* (11), 790-795.

(39) Dutton, S. E.; Kumar, M.; Mourigal, M.; Soos, Z. G.; Wen, J. J.; Broholm, C. L.; Andersen, N. H.; Huang, Q.; Zbiri, M.; Toft-Petersen, R.; Cava, R. J., Quantum spin liquid in frustrated one-dimensional $LiCuSbO_4$. *Phys. Rev. Lett.* **2012,** *108* (18), 187206.

(40) Mourigal, M.; Enderle, M.; Fak, B.; Kremer, R. K.; Law, J. M.; Schneidewind, A.; Hiess, A.; Prokofiev, A., Evidence of a bond-nematic phase in $LiCuVO_4$. *Phys. Rev. Lett.* **2012,** *109* (2), 027203.

(41) Bosiocic, M.; Bert, F.; Dutton, S. E.; Cava, R. J.; Baker, P. J.; Pozek, M.; Mendels, P., Possible quadrupolar nematic phase in the frustrated spin chain $LiCuSbO_4$: an NMR investigation. *Phys. Rev. B* **2017,** *96* (22), 224424.

(42) Glazkov, V.; von Nidda, H. A. K., Magnetic phase diagram and structure of the magnetic phases in the quasi-one-dimensional antiferromagnet $BaCu_2Si_2O_7$: a symmetry analysis. *Phys. Rev. B* **2004,** *69* (21), 212405.

(43) Tennant, D. A.; Perring, T. G.; Cowley, R. A.; Nagler, S. E., Unbound spinons in the S = 1/2 antiferromagnetic chain $KCuF_3$. *Phys. Rev. Lett.* **1993,** *70* (25), 4003-4006.

(44) Ramirez, A. P.; Wolf, W. P., Specific heat of $CsNiF_3$ - evidence for spin solitons. *Phys. Rev. Lett.* **1982,** *49* (3), 227-230.

(45) Hase, M.; Terasaki, I.; Uchinokura, K., Observation of the Spin-Peierls transition in linear Cu^{2+} (spin-1/2) chains in an inorganic compound $CuGeO_3$. *Phys. Rev. Lett.* **1993,** *70* (23), 3651-3654.

(46) Nishi, M.; Fujita, O.; Akimitsu, J., Neutron-scattering study on the spin-Peierls transition in a quasi-one-dimensional magnet $CuGeO_3$. *Phys. Rev. B* **1994,** *50* (9), 6508-6510.

(47)Matsuda, M.; Katsumata, K.; Eisaki, H.; Motoyama, N.; Uchida, S.; Shapiro, S. M.; Shirane, G., Magnetic excitations from the singlet ground state in the S=1/2 quasi-one-dimensional system $Sr_{14-x}Y_xCu_{24}O_{41}$. *Phys. Rev. B* **1996,** *54* (17), 12199-12206.

(48) Matsuda, M.; Katsumata, K., Observation of a dimerized state in the S=1/2 quasi-one-dimensional antiferromagnet $Sr_{14}Cu_{24}O_{41}$. *Phys. Rev. B* **1996,** *53* (18), 12201-12205.

(49) Azuma, M.; Hiroi, Z.; Takano, M.; Ishida, K.; Kitaoka, Y., Observation of a spin gap in $SrCu_2O_3$ comprising spin-1/2 quasi-1D 2-leg ladders. *Phys. Rev. Lett.* **1994,** *73* (25), 3463-3466.

(50) Magishi, K.; Matsumoto, S.; Kitaoka, Y.; Ishida, K.; Asayama, K.; Uehara, M.; Nagata, T.; Akimitsu, J., Spin gap and dynamics in $Sr_{14-x}Ca_xCu_{24}O_{41}$ comprising hole-doped two-leg spin ladders: Cu NMR study on single crystals. *Phys. Rev. B* **1998,** *57* (18), 11533-11544.

(51) Harcombe, D. R.; Welch, P. G.; Manuel, P.; Saines, P. J.; Goodwin, A. L., One-dimensional magnetic order in the metal-organic framework $Tb(HCOO)_3$. *Phys. Rev. B* **2016,** *94* (17), 174429.

(52) Brookes, N. B.; Chang, Y.; Johnson, P. D., Magnetic interface states and finite-size effects. *Phys. Rev. Lett.* **1991,** *67* (3), 354-357.

(53) Shores, M. P.; Nytko, E. A.; Bartlett, B. M.; Nocera, D. G., A structurally perfect S = 1/2 Kagome antiferromagnet. *J. Am. Chem. Soc.* **2005,** *127* (39), 13462-13463.

(54) Wang, M. C.; Huang, C. C.; Cheung, C. H.; Chen, C. Y.; Tan, S. G.; Huang, T. W.; Zhao, Y.; Zhao, Y. F.; Wu, G.; Feng, Y. P.; Wu, H. C.; Chang, C. R., Prospects and opportunities of 2D van der Waals magnetic systems. *Ann. Phys.* **2020***, 532,* 1900452.

(55) Joy, P. A.; Vasudevan, S., Magnetism in the layered transition-metal thiophosphates MPS_3 (M = Mn, Fe, and Ni). *Phys. Rev. B* **1992,** *46* (9), 5425-5433.

(56) Brec, R., Review on Structural and chemical-properties of transition-metal phosphorus trisulfides MPS_3. *Solid State Ion.* **1986,** *22* (1), 3-30.

(57) Gibertini, M.; Koperski, M.; Morpurgo, A. F.; Novoselov, K. S., Magnetic 2D materials and heterostructures. *Nat. Nanotechnol.* **2019,** *14* (5), 408-419.

(58) Gong, C.; Li, L.; Li, Z. L.; Ji, H. W.; Stern, A.; Xia, Y.; Cao, T.; Bao, W.; Wang, C. Z.; Wang, Y. A.; Qiu, Z. Q.; Cava, R. J.; Louie, S. G.; Xia, J.; Zhang, X., Discovery of intrinsic ferromagnetism in two-dimensional van der Waals crystals. *Nature* **2017,** *546* (7657), 265-269.

(59) Huang, B.; Clark, G.; Navarro-Moratalla, E.; Klein, D. R.; Cheng, R.; Seyler, K. L.; Zhong, D.; Schmidgall, E.; McGuire, M. A.; Cobden, D. H.; Yao, W.; Xiao, D.; Jarillo-Herrero, P.; Xu, X. D., Layer-dependent ferromagnetism in a van der Waals crystal down to the monolayer limit. *Nature* **2017,** *546* (7657), 270-273.

(60 Li, H.; Ruan, S. C.; Zeng, Y. J., Intrinsic Van Der Waals magnetic materials from bulk to the 2D Limit: New frontiers of spintronics. *Adv. Mater.* **2019,** *31* (27), 1900065.

(61) Shen, J. F.; He, Y. M.; Wu, J. J.; Gao, C. T.; Keyshar, K.; Zhang, X.; Yang, Y. C.; Ye, M. X.; Vajtai, R.; Lou, J.; Ajayan, P. M., Liquid phase exfoliation of two-dimensional materials by directly probing and matching surface tension components. *Nano Lett* **2015,** *15* (8), 5449-5454.

(62) Chae, S.; Oh, S.; Choi, K. H.; Lee, J. W.; Jeon, J.; Liu, Z. X.; Wang, C.; Woo, C.; Shi, L. Y.; Kang, J.; Song, S. Y.; Kim, S. J.; Lee, J. H.; Yu, H. K.; Choi, J. Y., Aqueous dispersion of 1D van der Waals $Mo_6S_3I_6$ crystal using biocompatible tri-block copolymer. *Ceram. Int.* **2021,** *47* (9), 11935-11941.

(63) Chae, S.; Siddiqa, A. J.; Kim, B. J.; Oh, S.; Choi, K. H.; Lee, K. H.; Kim, H. Y.; Yu, H. K.; Choi, J. Y., Isolation of inorganic molecular chains from rod-like bulk V_2Se_9 crystal by liquid exfoliation. *RSC Adv.* **2018,** *8* (62), 35348-35352.

(64) Kim, B. J.; Jeong, B. J.; Oh, S.; Chae, S.; Choi, K. H.; Nasir, T.; Lee, S. H.; Kim, K. W.; Lim, H. K.; Choi, I. J.; Chi, L.; Hyun, S. H.; Yu, H. K.; Lee, J. H.; Choi, J. Y., Mechanical exfoliation and electrical characterization of a one-dimensional Nb_2Se_9 atomic crystal. RSC *Adv.* **2018,** *8* (66), 37724-37728.

(65) Yoon, S. O.; Jeon, J.; Choi, K. H.; Jeong, B. J.; Chae, S.; Kim, B. J.; Oh, S.; Woo, C.; Lee, B.; Cho, S.; Kim, T. Y.; Jang, H. E.; Ahn, J.; Dong, X.; Ghulam, A.; Park, J. H.; Lee, J. H.; Yu, H. K.; Choi, J. Y., High breakdown current density in quasi-1D van der Waals layered material Ta_2NiSe_7. *ACS Appl. Mater. Inter.* **2021,** *13* (44), 52871-52879.

(66) Tarascon, J. M.; Disalvo, F. J.; Chen, C. H.; Carroll, P. J.; Walsh, M.; Rupp, L., First Example of Monodispersed $(Mo_3Se_3)^{1\infty}$ Clusters. *J. Solid. State. Chem.* **1985,** *58* (3), 290-300.

(67) Kong, T.; Stolze, K.; Ni, D. R.; Kushwaha, S. K.; Cava, R. J., Anisotropic magnetic properties of the ferromagnetic semiconductor $CrSbSe_3$. *Phys. Rev. Mater.* **2018,** *2* (1), 014410.

(68) Odink, D. A.; Carteaux, V.; Payen, C.; Ouvrard, G., Synthesis and Structure of $CrSbSe_3$ - a Pseudo-One-Dimensional Ferromagnet. *Chem. Mater.* **1993,** *5* (2), 237-240.

(69) Feng, Q. Q.; Li, X. Y.; Li, X. X.; Yang, J. L., $CrSbS_3$ monolayer: a potential phase transition ferromagnetic semiconductor. *Nanoscale* **2021,** *13* (33), 14067-14072.

(70) Mathew, T.; Rahul, K. S.; Mathew, V., Density functional study of magnetic, structural and electronic properties of quasi-one-dimensional compounds $CrSbX_3$ (X = S, Se). *Comput. Condens. Matter* **2020,** *23*, e00467.

(71) Volkov, V. V.; VanTendeloo, G.; VanLanduyt, J.; Amelinckx, S.; Busheva, E. E.; Shabunina, G. G.; Aminov, T. G.; Novotortsev, V. M., HREM image analysis up to structure determination of $SbCrSe_3$: a new 1D ferromagnet. *J. Solid State Chem.* **1997,** *132* (2), 257-266.

(72) Djieutedjeu, H.; Lopez, J. S.; Lu, R. M.; Buchanan, B.; Zhou, X. Y.; Chi, H.; Ranmohotti, K. G. S.; Uher, C.; Poudeu, P. F. P., Charge Disproportionation Triggers Bipolar Doping in $FeSb_{2-x}Sn_xSe_4$ Ferromagnetic Semiconductors, Enabling a Temperature-Induced Lifshitz Transition. *J. Am. Chem. Soc.* **2019,** *141* (23), 9249-9261.

(73) Djieutedjeu, H.; Poudeu, P. F. P.; Takas, N. J.; Makongo, J. P. A.; Rotaru, A.; Ranmohotti, K. G. S.; Anglin, C. J.; Spinu, L.; Wiley, J. B., Structural-Distortion-Driven Cooperative Magnetic and Semiconductor-to-Insulator Transitions in Ferromagnetic $FeSb_2Se_4$. *Angew. Chem. Int. Edit.* **2010,** *49* (51), 9977-9981.

(74) Djieutedjeu, H.; Makongo, J. P. A.; Rotaru, A.; Palasyuk, A.; Takas, N. J.; Zhou, X. Y.; Ranmohotti, K. G. S.; Spinu, L.; Uher, C.; Poudeu, P. F. P., Crystal Structure, Charge Transport, and Magnetic Properties of $MnSb_2Se_4$. *Eur. J. Inorg. Chem.* **2011,** (26), 3969-3977.

(75) Ranmohotti, K. G. S.; Djieutedjeu, H.; Poudeu, P. F. P., Chemical Manipulation of Magnetic Ordering in $Mn_{1-x}Sn_xBi_2Se_4$ Solid-Solutions. *J. Am. Chem. Soc.* **2012,** *134* (34), 14033-14042.

(76) Ranmohotti, K. G. S.; Djieutedjeu, H.; Lopez, J.; Page, A.; Haldolaarachchige, N.; Chi, H.; Sahoo, P.; Uher, C.; Young, D.; Poudeu, P. F. P., Coexistence of High-Tc Ferromagnetism and n-Type Electrical Conductivity in $FeBi_2Se_4$. *J. Am. Chem. Soc.* **2015,** *137* (12), 4274-4274.

Chapter 2

Ultrathin, High-Aspect Ratio, and Free-Standing Magnetic Nanowires by Exfoliation of Ferromagnetic Quasi-One-Dimensional van der Waals Lattices

2.1 Abstract

Driven by numerous discoveries of novel physical properties and integration into functional devices, interest in one-dimensional (1D) magnetic nanostructures has grown tremendously. Traditionally, such structures are accessed with bottom-up techniques, but these require increasing sophistication to allow precise control over crystallinity, branching, aspect-ratio, and surface termination, especially when approaching the sub-nanometer regime in magnetic phases. Here, we show that mechanical exfoliation of bulk quasi-one-dimensional crystals, a method similar to those popularized for two-dimensional van der Waals (vdW) lattices, serves as an efficient top-down method to produce ultrathin freestanding nanowires that are both magnetic and semiconducting. We use $CrSbSe_3$ as a representative quasi-1D van der Waals crystal with strong magnetocrystalline anisotropy, and show that it can be exfoliated into nanowires with average cross-section of 10 ± 2.8 nm. The $CrSbSe_3$ nanowires display reduced Curie-Weiss temperature, but higher coercivity and remanence than the bulk phase. The methodology developed here for $CrSbSe_3$, a representative for a vast class of 1D vdW lattices, serves as a blueprint for investigating confinement effects for 1D materials and accessing functional nanowires that are difficult to produce *via* traditional bottom-up methods.

2.2 Introduction

Nanoscale low-dimensional magnetic devices have enabled studies of a vast range of exotic physical phenomena[1-3] such as spin-Peierls transitions in spin chains[4] and superconductivity in spin-ladder systems,[5] and have given rise to technologies spanning magnetic refrigeration,[6-7] implantable bioelectronics,[8-9] and data storage devices.[10-14] Many of these technologies benefit from the use of one-dimensional (1D) magnetic nanostructures, which have smaller footprints, greater sensitivity towards external stimuli, and enhanced coercivity enabled by their inherent shape anisotropy.[15] The advantages conferred by nanowires have led to numerous advances in bottom-up synthetic routes, such as vapor- and solution-phase growth,[16-18] electrodeposition,[19-21] and lithographic methods,[22-23] which can yield freestanding magnetic nanowires with well-defined diameters, lengths, compositions, and phase purity. Challenges remain, however, because these traditional bottom-up methods often do not allow for precise control over the long-range nanowire morphologies, and they typically lead to surface passivation and the formation of defects.[24-29] Alternatively, one can employ top-down approaches to isolate wires from bulk crystals, as demonstrated with $Mo_6S_3I_6$,[30-33] $SnIP$,[34] and V_2Se_9,[35-36] which comprise strong covalently-bonded molecular chains connected by van der Waals (vdW) inter-chain interactions. This approach has shown great promise because starting from ostensibly more highly ordered and surface defect-free bulk crystals yields nanowires whose structural and physical properties enable potential applications in transistors and photovoltaic devices.[30, 37-47] To our knowledge, however, these softer methodologies have not been extended to magnetic vdW phases and, critically, their utility in accessing highly desirable ultrathin magnetic nanowires remains largely unexplored.

Here, we describe a top-down approach to fabricating semiconducting magnetic nanowires from bulk crystals comprised of one-dimensional inorganic magnetic chains held together predominantly by vdW interactions. Contrasting with related methods pioneered for instance with the solution stabilization of $Li_2Mo_6Se_6$ highly polar solvents,[48-49] this method is distinct because it does not require cation solvation and produces free-standing nanowires that do not require solution or surface stabilization. In fact, the methodology reported here is most closely related to the mechanical exfoliation of 2D vdW phases popularized with graphene and transition metal dichalcogenides. Indeed, although exfoliation is obviously widely used with bulk 2D vdW lattices, including for producing free-standing ultrathin magnetic sheets,[50-57] it has rarely, if ever, been used

on bulk 1D vdW magnetic lattices, whose magnetic behavior upon dimensional reduction to the nanowire regime likewise remains poorly understood.

To highlight the potential utility of 1D vdW exfoliation in the production of magnetic nanowires, we chose $CrSbSe_3$ as a representative example. Although there are numerous bulk phases that can be described as 1D vdW crystals, exceedingly few show magnetic ordering.[58-62] Featuring weakly associated double-rutile chains of covalently bonded atoms, bulk $CrSbSe_3$ exhibits robust ferromagnetic ordering below 71 K. [63-64] The Sb atoms are critical: their lone pairs provide steric repulsion that separate individual $CrSbSe_3$ chains and open vdW gaps. We used time-of-flight (T.O.F.) powder neutron diffraction to establish the ferromagnetic ground state and the apparent magnetocrystalline anisotropy of $CrSbSe_3$ and show that as-synthesized $CrSbSe_3$ crystals can be readily exfoliated into 10 ± 2.8 nm thick nanowires. Importantly, the exfoliated $CrSbSe_3$ nanowires are resistant to oxidation under ambient conditions. Exfoliation of the bulk crystals into long and thin nanowires significantly decreases the Curie-Weiss temperature (θ_{CW}) and simultaneously increases their coercivity and remanence. Exfoliation thus produces a harder ferromagnetic phase than bulk $CrSbSe_3$, as has also been seen upon nanostructuring traditional ferromagnets such as Ni and Fe_2O_3.[65-66] These findings demonstrate that well-established exfoliation methods can be adapted to new classes of functional vdW lattices, particularly for the creation of 1D magnetic nanostructures.

2.3 Results and Discussions

2.3.1 Structural Characterization

As reported previously, $CrSbSe_3$ crystallizes in the orthorhombic *Pnma* space group and features double-rutile chains of covalently bonded atoms extending along the *b* axis (**Figure 2.1a**).[63-64] The Sb atoms occupying the edge of the double-rutile chains bind three Se atoms in trigonal pyramidal geometry. Owing to the close electronegativity values of Sb and Se, the lone pair on Sb provides steric repulsion and forms a vdW gap with Se orbitals on neighboring chains. Indeed, the nearest neighbor distance between a Sb atom on one chain and a Se atom on an adjacent

chain, 3.2494(9) Å, is much longer than the Sb–Se bond distances within a chain: 2.6473(8) Å and 2.6679(11) Å (**Figure 2.1a, Table S4**). Bulk CrSbSe$_3$ is grown either by typical solid state melt synthesis, which yields polycrystalline powders, or by flux growth, which yields needle-like millimeter-sized single crystals with fibrous morphology, a macroscopic indication of the quasi-1D vdW nature of the crystals (**Figure 2.1b,c,** see **2.5.1** for synthesis details). Elemental mapping by energy-dispersive X-ray spectroscopy (EDS) confirmed the homogeneous distribution of Cr, Sb, and Se throughout the crystals (**Figure 1d**).
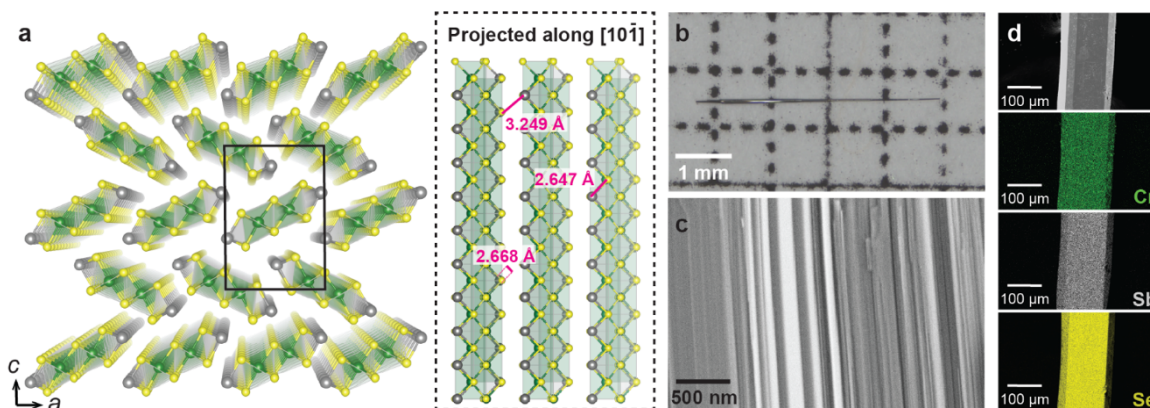
Figure 2.1. Structure and characterization of CrSbSe$_3$. a) X-ray crystal structure of CrSbSe$_3$ at 298 K, with the unit cell outlined in black (left) and the double-rutile chains extending along the **b** axis labeled with three relevant of Sb-Se distances (right). Green, grey and yellow spheres represent Cr, Sb, and Se, respectively. **b)** A single crystal of flux-grown CrSbSe$_3$. **c)** Scanning electron microscopy (SEM) micrograph of an as-synthesized CrSbSe$_3$ single crystal after mechanical cleavage. **d)** SEM micrograph with the corresponding EDS elemental maps of CrSbSe$_3$.

2.3.2 Magnetic Structure Analysis

We used T.O.F. powder neutron diffraction to determine the magnetic structure and correlate structural parameters in CrSbSe$_3$ with its established bulk ferromagnetic behavior. It had been shown that the ferromagnetic transition temperature (T_C) of bulk CrSbSe$_3$ is at approximately 71 K. As such, we refined neutron diffraction data above and below T_C. Significantly, data

collected at 10 K displayed increased intensity for several Bragg peaks at the high T.O.F. (> 100,000 μsec) or d-spacing region (**Figure 2.2a**). Indexing and refinement of this data revealed that the magnetic unit cell has the same parameters as the crystallographic unit cell (**Figure 2.2b, see 2.5.2** for the detailed results of the Rietveld refinement). Rietveld refinement of the neutron diffraction patterns revealed ferromagnetic order with spin moments aligned along the a axis (**Figure 2.2c**). Because magnetic neutron scattering is sensitive only to the magnetic moment components that are perpendicular to the scattering vector, the absence of the magnetic (100) peak indicates a perfect alignment of the ferromagnetically ordered moments along the a axis, without spin canting. These data confirm the magneto-crystalline anisotropy and the magnetic easy axis, previously suggested solely on the basis of magnetic susceptibility measurements of oriented crystals.[63] Similarly, the neutron diffraction-derived magnetic moment of 3.06(7) μ_B/Cr is consistent with the ground spin state of S = 3/2 for Cr(III), determined from magnetization data.
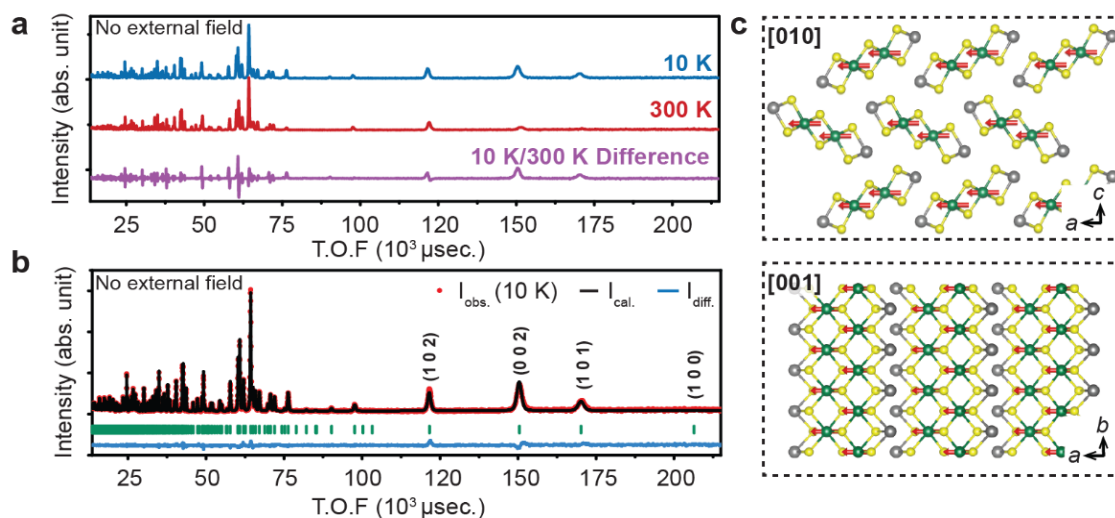

Figure 2.2. Magnetic structure of the CrSbSe$_3$ lattice. a) Comparison of the neutron diffraction profiles at 10 K (ferromagnetic state) and 300 K (paramagnetic state) in the absence of an external magnetic field. b) Final observed (red dots), fitted (black curve) and difference (blue curve) powder neutron diffractograms of bulk CrSbSe$_3$. Several zone axes of interest are labeled with their respective Miller indices. c) The refined magnetic structure of CrSbSe$_3$ derived from the powder neutron diffraction profile projected along the [010] (top) and [001] (bottom) axes.

2.3.3 Exfoliation of CrSbSe$_3$ into Nanowires

With evidence in hand that CrSbSe$_3$ presents as a quasi-1D vdW crystal that shows both magnetic ordering and significant anisotropy, we sought to investigate changes to these properties upon isolating nanowires from the bulk. To do so, we employed a solution technique pervasive in 2D vdW materials that involves systematic tuning of polarity and dispersity of solvent mixtures to optimize exfoliation.[67-70] To this end, the isopropanol (iPrOH)-water mixture covers a wide range of both dispersive and polar parameters and was also used here.[70-71] When subjecting CrSbSe$_3$ suspensions after ultrasonication to liquid cascade centrifugation (**Figure 2.3a** and see **2.5.3** for exfoliation details) which removes the large and unexfoliated chunks and keeps the efficiently exfoliated nanoparticles, we found that a volumetric 30:70 iPrOH:water mixture and the 100% iPrOH yield the highest concentration of dispersed CrSbSe$_3$ nanoparticles (**Figure 2.3b, Table**
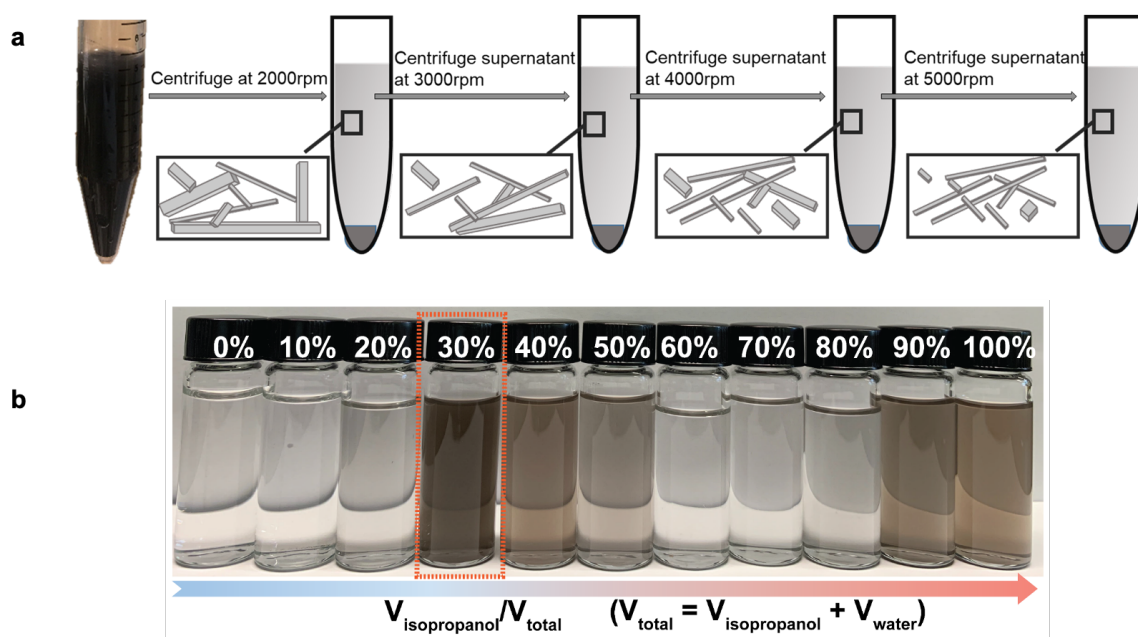

Figure 2.3. Exfoliation and liquid cascade sonication of CrSbSe$_3$. a) An illustration of the liquid cascade centrifugation process for the separation exfoliated nanowires from not efficiently exfoliated particles in the colloidal solutions after sonication. **b)** CrSbSe$_3$ dispersions in iPrOH/H$_2$O solvent mixtures with increasing iPrOH volume ratios (%V$_{iPrOH}$/V$_{total}$) and decreasing polarity from left to right. V$_{total}$ denotes the total volume of iPrOH and H$_2$O.
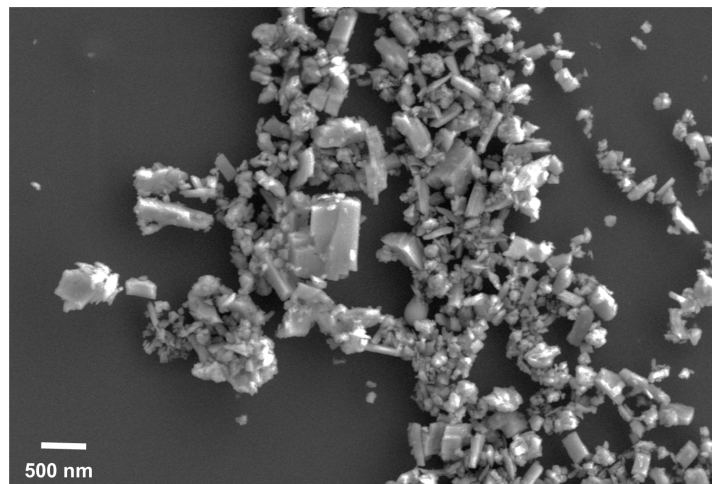
Figure 2.4. Representative SEM micrograph of the drop-casted exfoliated CrSbSe$_3$ nanoparticles in 100% *i*PrOH.

2.1). When checked under SEM, the exfoliated nanoparticles of bulk CrSbSe$_3$ powder in 100% *i*PrOH are isotropic nanoparticles of CrSbSe$_3$ rather than nanowires (**Figure 2.4**), but the exfoliation of CrSbSe3 in 30:70 *i*PrOH:water mixture yields beautiful ultrathin nanowires (Figure **2.5** and **2.6**). Measurement of 70 individual randomly oriented nanowires using atomic force microscopy (AFM) gave an average cross-section of 10 ± 2.8 nm (**Figure 2.7**). Thus, the exfoliation-centrifugation method is particularly efficient at producing ultrathin and long wires with a narrow cross-sectional distribution. Indeed, three-dimensional AFM topographical view of single nanowires revealed uniform thickness along the length of the nanowire, with no tapering, branching, or kinking that are often seen in nanowires grown by bottom-up methods (**Figure 2.7** bottom). Furthermore, nanowires produced by our method are smooth, with surface roughness of ± 0.2 nm over 1 μm, further highlighting the absence of morphological distortions, discontinuities, or cracks along the nanowire surface (**Figure 2.8**). This successful exfoliation process demonstrates that concepts and techniques in traditional top-down exfoliation in 2D vdW materials can be extended and translated to magnetic vdW materials with lower dimensionalities.

Table 2.1. Concentrations of the CrSbSe$_3$ nanowire dispersions in isopropanol (iPrOH)/H$_2$O cosolvent system.

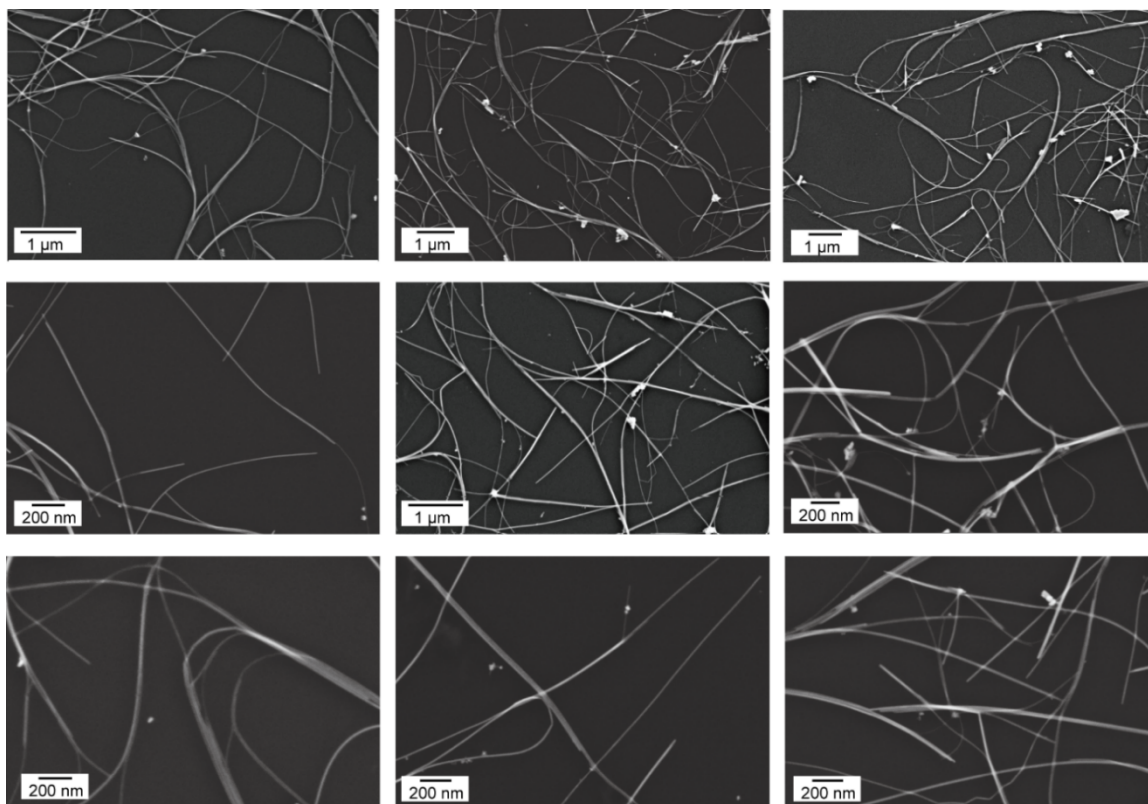| V$_{i\text{PrOH}}$/V$_{\text{total}}$	Concentration (mg/mL)
30%	0.043
40%	0.033
50%	0.031
90%	0.025
100%	0.025

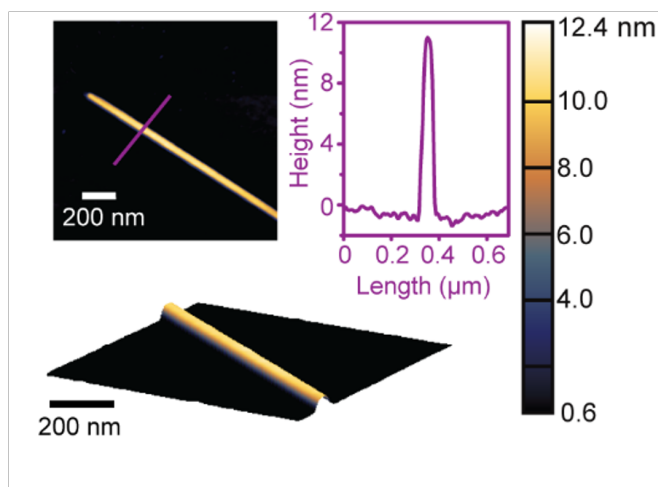**Figure 2.5.** Representative SEM micrograph of the drop-casted CrSbSe$_3$ nanowires on 300 nm SiO$_2$/Si.

Figure 2.6. AFM image of a single CrSbSe$_3$ nanowire with the corresponding line profile (top) and 3D topographical view (bottom).
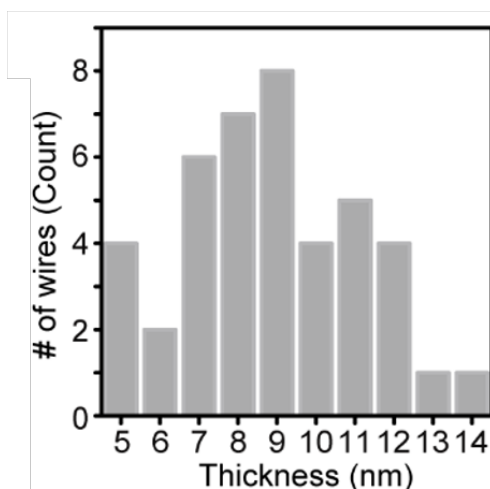

Figure 2.7. Cross-section distributions of CrSbSe$_3$ nanowires determined by AFM imaging. corresponding line profile
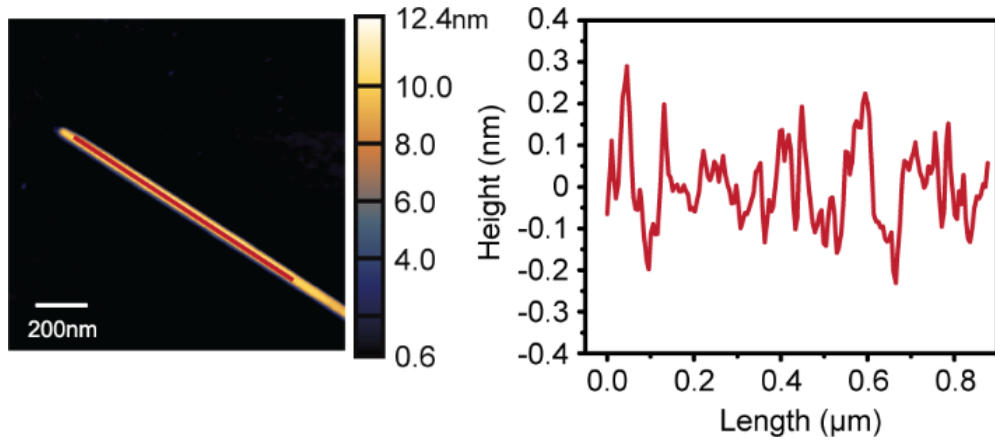
Figure 2.8. Surface roughness of one CrSbSe$_3$ nanowire on 300nm SiO$_2$/Si substrate determined by linear roughness measurement in AFM.

2.3.4 Stability of the Exfoliated CrSbSe$_3$ Nanowires

Raman spectroscopy and X-ray photoelectron spectroscopy (XPS) confirmed the phase identity, crystallinity, and surface stability of the exfoliated CrSbSe$_3$ nanowires. Because phonon modes are directly correlated to the structural identity and inherent crystallinity of a material, we
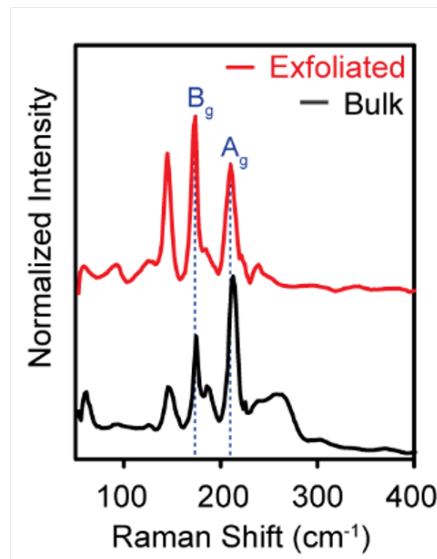

Figure 2.9. Micro-Raman spectra of the bulk and exfoliated CrSbSe$_3$. The symmetries of the phonon modes corresponding to directions perpendicular (A$_g$) and parallel (B$_g$) to the crystal long axis are labeled in blue and purple, respectively.

probed the evolution of these modes in CrSbSe$_3$ upon its exfoliation from bulk into nanowires. As shown in **Figure 2.9** (See also **2.5.4** for detailed Raman analysis), all Raman modes present in bulk CrSbSe$_3$ are also found in exfoliated nanowires, including the most prominent bands at 212.8 cm^{-1} and 174.4 cm^{-1}, whose narrow full-width half-max of 10.0 cm^{-1} and 6.3 cm^{-1}, respectively, remain nearly unchanged and indicate a high degree of crystallinity. We attribute lower energy shifts of approximately 2 cm^{-1} to phonon confinement effects as the lattice is reduced from bulk to nanowires.[72] XPS of CrSbSe$_3$ single crystals and exfoliated nanowires, shown in **Figure 2.10**, revealed two energy bands for Cr, at 575.2 eV (*2p$_{3/2}$*) and 584.6 eV (*2p$_{1/2}$*), which agree well with the reported binding energy of Cr *2p* in similar coordination environments.[73] The broad non-symmetric peak shape of the Cr *2p* peaks can be attributed to multiplet splitting, which is common for Cr(III) compounds.[74] Similarly, the Sb *3d* spectra of bulk crystals and exfoliated nanowires both show two bands at 529.3 eV (*3d$_{5/2}$*) and 538.8 eV (*3d$_{3/2}$*), in good agreement with literature values for Sb (See **2.5.5** for detailed peak fitting).[75] Notably, there are no signs of oxidation upon exfoliation, as evidenced by the absence of higher binding energy peaks in both the Cr *2p* and the Sb *3d* regions.
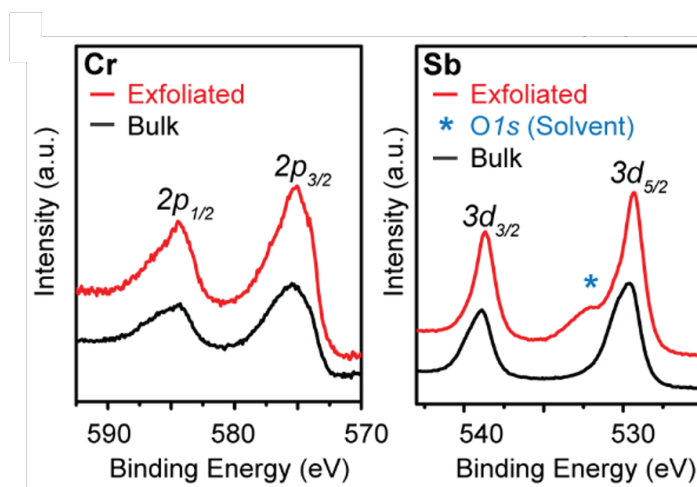

Figure 2.10. XPS spectra of the Cr *2p* and the Sb *3d* of both bulk crystals and exfoliated nanowires of CrSbSe$_3$. In Sb 3d spectrum, the peak marked by an asterisk corresponds to the O 1s contribution from the exfoliation solvent.

2.3.5 Magnetic Properties of Bulk and Exfoliated CrSbSe$_3$

Exfoliating bulk crystals into nanowires allows systematic studies for understanding the evolution of magnetic properties of CrSbSe$_3$ upon nanosizing. We first confirmed the magnetic properties of bulk CrSbSe$_3$ by susceptibility measurements from 2 K to 300 K under an applied field of 1 kOe. A linear fit of this data in the high temperature region gives an effective moment of 4.2 μ_B/Cr, in agreement with the spin-only value expected for Cr(III) (3.9 μ_B). Fitting this data to the Curie-Weiss law gives θ_{CW} ~ 133 K, indicating ferromagnetic coupling between the Cr^{3+} centers, with T$_C$ around 70 K (See fitting details in **2.5.6**). The field-dependent magnetization curve at 2 K collected at fields up to 80 kOe saturates at 3 μ_B/Cr, further confirming both the phase purity and ferromagnetic ordering of the Cr^{3+} spins in the bulk CrSbSe$_3$ lattice (**Figure 2.11a**). Close inspection of the magnetic hysteresis loop indicates that both the coercivity, H$_c$, and the remanence are very low (H$_c$ = 140 Oe), in agreement with previous reports classifying bulk CrSbSe$_3$ as a soft ferromagnet.[63-64]

Generally, the magnetization behavior of nanostructures tends to minimize the total free energy in terms of exchange energy, Zeeman energy, magnetoelastic energy, and anisotropy energy. Among these, the variation of the anisotropy term with particle shape has been experimentally and theoretically investigated extensively,[20, 76-77] and has been found to significantly influence fundamental magnetic properties including the coercivity, remanence, saturation magnetization, easy axis, and magnetic reversal process.[20, 77-78] Naturally, particle size also affects physical properties, especially when reaching the nanometer regime.[79] In magnetism, these finite-size effects are evident, for instance, when the particle size reaches that of the excitation wavelength of magnons, the domain wall width, or the spin-spin correlation length. Given the significantly altered morphology and particle size upon exfoliation, it is therefore reasonable to expect that nanowires of CrSbSe$_3$ should show different magnetic properties from the bulk.

Directly probing the magnetic properties of a single nanowire by magnetic force microscopy or magnetic-optical methods such as Kerr microscopy is challenging due to the low magnetic ordering temperature of $CrSbSe_3$ and the extreme thinness of the exfoliated nanowires that are well below the optical diffraction limit. An alternative method, demonstrated previously for exfoliated 2D hematite crystals, involves collecting the exfoliated particles and interpreting their collective magnetic properties.[66] Here, we filtered the final supernatant after the liquid cascade centrifugation and collected about 1 mg of exfoliated $CrSbSe_3$ nanowires. The shape of the magnetization curve for these nanowires (**Figure 2.11a**) suggests that the long-range ferromagnetic ordering present in bulk $CrSbSe_3$ persists upon exfoliation. However, the hysteresis loop demonstrates that the coercivity is significantly enhanced by as much as one order of magnitude, from $H_c = 0.14$ kOe in the bulk to $H_c = 1.5$ kOe in the exfoliated nanowires, and that the remanence increases from 0.2 μ_B/Cr in the bulk to 0.5 μ_B/Cr in the exfoliated nanowires. Notably, these results suggest that upon exfoliation into ultrathin nanowires, $CrSbSe_3$ transitions
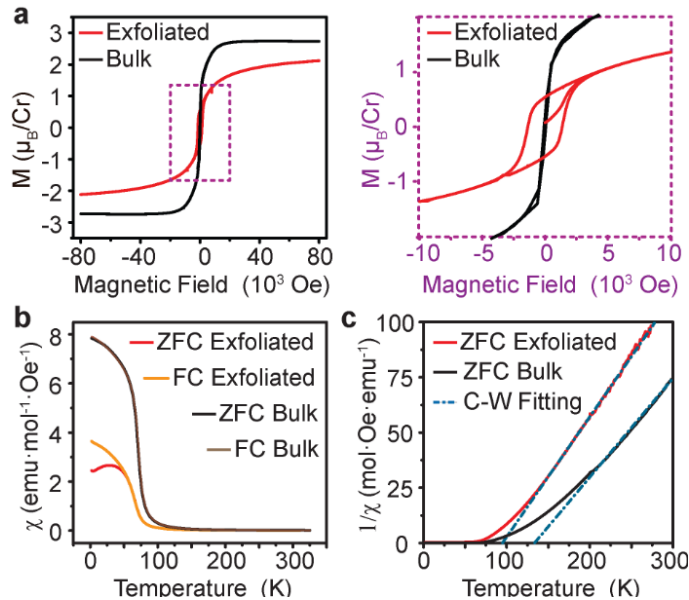

Figure 2.11. Magnetic properties of bulk polycrystalline powder and exfoliated nanowires of $CrSbSe_3$. a) Comparison of the M-H data for bulk and exfoliated nanowires of $CrSbSe_3$ at 2 K. (b) Temperature dependent field-cooled (FC) and zero field-cooled (ZFC) molar magnetic susceptibility curves of bulk and exfoliated $CrSbSe_3$ under an applied field of 1 kOe (c) Curie-Weiss fits of the temperature-dependent inverse susceptibilities for bulk and exfoliated $CrSbSe_3$.

from a soft to a hard ferromagnet. Similar transitions have been observed for other low-dimensional magnetic systems and are often assigned to increasing anisotropy.[80-84] In bulk $CrSbSe_3$, although the spins prefer to align along the *a* axis, the magneto-crystalline anisotropy is relatively weak, as manifested by the low coercivity and low remanence. However, exfoliation into nanowires greatly changes the aspect ratio whereby the wire dimension along the crystallographic *b* direction is much longer than along *a* and *c*, giving rise to strong shape anisotropy. Consequently, the anisotropy energy increases, which imposes a greater barrier to spin flipping and induces a greater hysteresis.

Further understanding of the evolution of magnetic properties upon exfoliation came from analyzing the temperature-dependent magnetic susceptibility from 2 K to 300 K under an external field of 1 kOe. The zero-field cooled (ZFC) and field cooled (FC) magnetization curves bifurcate at low temperatures, consistent with the expected behavior of hard magnets (**Figure 2.11b**).[85] The susceptibility data above 140 K can be fitted to the Curie-Weiss law to give a Curie constant of 3.9 μ_B/Cr and θ_{CW} of approximately 95 K. This θ_{CW} is 38 K lower than the value for the bulk crystal (**Figure 2.11c**) and can be ascribed to finite-size effects: in bulk $CrSbSe_3$, which is a 3D ferromagnet, the spin-spin correlation length ξ is expected to increase with temperature and diverge at the ordering temperature.[86] Upon exfoliation, where the dimensions along the crystallographic *a* and *c* directions become significantly smaller, the growth of the correlation length with temperature is constrained by the wire diameter d, resulting in a reduced θ_{CW}. Although similar finite-size effects have been established both experimentally and theoretically in 2D thin films as well as zero-dimensional nanoparticles,[79, 87-90] they are much less investigated in 1D or quasi-1D nanowires, with several theoretical and experimental reports nevertheless showing strong size dependence of θ_{CW}.[91]

2.4 Conclusions

The foregoing results demonstrate that solution exfoliation is an efficient technique for accessing ultrathin ferromagnetic nanowires with high aspect ratio from bulk crystals of 1D vdW-connected lattices. As proof-of-principle, we showed that $CrSbSe_3$, a bulk ferromagnet made from vdW-connected 1D chains, serves as a good precursor for obtaining air-stable, free-standing nanowires that show increased coercivity and remanence compared to the bulk. These results

provide a blueprint for additional studies with other bulk 1D vdW crystals. They further motivate studies aimed at understanding how magnetic interactions in bulk crystals evolve upon nanostructuring.

2.5 Methods and Supplementary Details

2.5.1 Synthesis of CrSbSe₃.

Single crystals of $CrSbSe_3$, used in electron-dispersive X-ray spectroscopy (EDS) mapping, Raman spectroscopy and X-ray photoelectron spectroscopy (XPS), were grown *via* a modified high temperature flux method.[63] Elemental Cr, Sb, and Se were mixed in a molar ratio of Cr:Sb:Se = 7:33:60. Excess Sb and Se were used as flux, and the mixture was sealed into fused quartz tubes under a pressure of ~ 50 mTorr. The sealed ampoule was first ramped to 600 °C over 3 hours, kept at 600 °C for 3 hours, then ramped to 800 °C over 2 hours, and kept at this temperature for 3 days. The mixture was then cooled down to 680 °C slowly over 5 days and subsequently centrifuged at this temperature to remove the flux. The small amount of flux remaining on the surface of the crystals was removed by keeping the as-grown crystals at 500 °C for 3 days in a sealed fused quartz ampoule while leaving the cold end of the ampoule at room temperature. Polycrystalline powders of $CrSbSe_3$, used for time-of-flight (T.O.F.) powder neutron diffraction, magnetometry and exfoliation, were synthesized via a typical solid state melt reaction.[64] Starting elements were finely ground, mixed in stoichiometric ratio, and sealed into fused quartz tube under ~50 mTorr. Ampoules were heated to 800 °C over 3 hours and kept at this temperature for 2 days, followed by cooling to room temperature slowly over 5 days. The preparation and handling of all reagents was done under ambient conditions. Chromium (Sigma-Aldrich, 99.5%), antimony (STREM Chemicals, 99.5%) and selenium (STREM Chemicals, 99.99%) were purchased and used without further purification.

2.5.2 Liquid-Phase Exfoliation and Liquid Cascade Centrifugation.

Liquid-phase exfoliation was carried out *via* sonication (Branson 8800, 230 W, 25 °C) on finely ground samples dispersed in an isopropanol (*i*PrOH) and H_2O mixture with an optimized *i*PrOH volume fraction (V_{iPrOH} /V_{total}; V_{total} denotes the total volume of *i*PrOH and H_2O) and a starting concentration of 1 mg/mL for 2 hours. To eliminate large, unexfoliated solids, the resulting dispersion was first separated by centrifugation at 2000 r.p.m. for 10 minutes. The sediment from this centrifugation was removed and the supernatant was subjected to further centrifugation at 3000 r.p.m. for 5 minutes. This procedure was repeated at 4000 r.p.m. (3 minutes) and 5000 r.p.m. (3 minutes). Finally, the supernatant after centrifugation at 5000 r.p.m. was collected and used for subsequent measurements and characterization. The resulting supernatant was filtered under vacuum onto pre-weighed Millipore nitrocellulose filters with 25 nm pore size.

2.5.3 Characterization Details

The single crystal structure of $CrSbSe_3$ was confirmed *via* single crystal X-ray diffraction (SXRD) of sizeable micron-sized crystals using a Bruker D8 diffractometer which is coupled to a Bruker APEX-II CCD detector and a Mo Kα radiation ($\lambda = 0.71073$ Å), performing ϕ- and ω-scans. The refinement of the structure was performed using direct methods in the SHELX package and refined against F^2 on all data by full-matrix least squares with SHELXL-13.[92] The T.O.F. powder neutron diffraction data were collected on polycrystalline samples loaded into thin-walled vanadium cans, on the T.O.F. powder diffractometer POWGEN at the Spallation Neutron Source, Oak Ridge National Laboratory. Structural and magnetic refinements were performed using the FullProf package.[93] The symmetry-allowed magnetic structures were derived using SARAH representational analysis program.[94] Magnetic susceptibility measurements were performed on powders using a Quantum Design Physical Property Measurement System (PPMS) Dynacool, equipped with a vibrating sample magnetometer (VSM) option. The polarized and unpolarized Raman spectra were collected on a Horiba Multiline Raman spectrometer with a 100x long working distance objective, 532 nm excitation line, and 600 gr/mm grating with a spot size of ~3 μm. The X-ray photoelectron spectra (XPS) were collected using a Thermo Nexsa X-ray photoelectron spectrometer with a monochromated Al X-ray source. Scanning electron microscopy (SEM) micrographs were acquired using a Zeiss Field Emission SEM Ultra55

equipped with an electron-dispersive X-ray spectroscopy (EDS) detector. Atomic force microscopy (AFM) images were acquired on a Cypher Atomic Force Microscope from Asylum Research using silicon probing tips with mid-range mechanical properties (f = 300 kHz, k = 26 N/m) from Oxford Instruments. The scan rates are 0.5-2 Hz depending on the scan size.

2.5.4 Crystal Structure and Magnetic Structure Details of Bulk CrSbSe₃

Table 2.2. Details of the structure determination of $CrSbSe_3$ based on single-crystal experiments measured at 300 K

Sum Formula	$CrSbSe_3$
Radiation	λ (Mo-$K\alpha$ = 0.71073 Å)
Thera range for data collection	$2\theta \leq 61.004°$
Index ranges	$-13 \leq h \leq 13, -5 \leq k \leq 5, -19 \leq 1 \leq 19$
Absorption coefficient /mm^{-1}	31.590
Measured reflections	11064
Independent reflections	805
No. of parameters	31
Goodness-of-fit on F^2	1.218
Final R indices [$I > 2\sigma\ (I)$]	0.0716
$R(int)$	0.0564
$R(\sigma)$	0.0255
R indices (all data)	0.0720
ωR_2 (all data)	0.1662
Largest diff. peak and hole (e$^-$/ Å^3)	3.651 to -3.729

Table 2.3. Selected crystallographic data of CrSbSe3 derived from Single-crystal X-ray Diffraction (SXRD) measured at 298 K, Time-of-Flight Powder Neutron Diffraction (T.O.F. PND) measured at 300 K and measured at 10 K.

	SXRD at 298 K	T.O.F. PND at 300 K	T.O.F. PND at 10 K
Crystal system	Orthorhombic	Orthorhombic	Orthorhombic
Space group	P n m a	P n m a	P n m a
Lattice parameter (Å)			
a	9.1552(3)	9.14356(14)	9.15077
b	3.78460(10)	3.78477 (5)	3.78376
c	13.3542(4)	13.41741(19)	13.33229
Cell volume (Å^3)	462.56(2)	464.326	461.621

Table 2.4. Atomic coordinates for CrSbSe$_3$ derived from SXRD at 298 K, T.O.F. PND measured at 300 K and 10 K.

SXRD at 298 K			
Atom	*x*	*y*	*z*
Cr	0.34320(14)	0.2500	0.45537(10)
Sb	0.02882(6)	0.7500	0.34153(5)
Se(1)	0.17119(9)	-0.2500	0.51586(6)
Se(2)	0.49948(9)	0.2500	0.60836(7)
Se(3)	0.21424(9)	0.2500	0.28611(6)

T.O.F. PND at 10 K			
Atom	*x*	*y*	*z*
Cr	0.15685(0)	0.25000(0)	0.04389(0)
Sb	0.02884(0)	0.25000(0)	0.65849(0)
Se(1)	0.17114(0)	0.25000(0)	0.48403(0)
Se(2)	0.50076(0)	0.25000(0)	0.60823(0)
Se(3)	0.28586(0)	0.25000(0)	0.21392(0)

	T.O.F. PND at 300 K		
Atom	***x***	***y***	***z***
Cr	0.15627(41)	0.25000(0)	0.04489(25)
Sb	0.02998(22)	0.25000(0)	0.65809(16)
Se(1)	0.17189(17)	0.25000(0)	0.48436(10)
Se(2)	0.50221(17)	0.25000(0)	0.60906(11)
Se(3)	0.28510(15)	0.25000(0)	0.21295(11)

Table 2.5. Selected bond lengths (or interatomic distances) of the refined $CrSbSe_3$ structure derived from SXRD at 300 K

	d (Å)
Cr-Se(1)	2.5907(11)
Cr-Se(2)	2.5255(11)
Cr-Se(3)	2.5499(16)
Sb-Se(1) (intra-chain covalent bond)	2.6679(11)
Sb-Se(3) (intra-chain covalent bond)	2.6473(8)
Sb-Se(1) (inter-chain vdW interaction)	3.2494(9)
Sb-Se(3) (inter-chain vdW interaction)	3.8439(9)

2.5.5. Symmetry Analysis of Bulk $CrSbSe_3$ Single Crystal for Raman Spectroscopy

We performed polarized Raman measurements in the backscattering geometry in order to probe the phonon modes in the $CrSbSe_3$ lattice. In these measurements, we performed (0°) co- and (90°) cross-polarized scattering measurements where the long axis of the crystal is parallel to the laser polarization. We used the standardized unit cell axes ($a \rightarrow a$, $b \rightarrow c$, $c \rightarrow b$), mainly assigning the high-symmetry principal axis from *b* to *c*, instead of the experimental single crystal unit cell and reported unit cell axes [1-2] for coherence and consistency with the group theory analyses. This measurement setup corresponds to the –X(ZZ)X and –X(YZ)X Porto notations for the co- and cross-polarized measurements. Since we are doing only the crystal axes perpendicular to the crystal long axis, in this case, X and Y are interchangeable. This won't affect any of the subsequent selection rules due to the nature of the symmetry. Similar to other orthorhombic crystals that are

comprised of isolated chains, with the same Pnma space group symmetry [95], we adopted the simplified C_{2h} point group instead of the D_{2h} point group. By doing this, we simplify and reduce the Raman-active modes from 30 modes ($2A_g + B_{1g} + 2B_{2g} + B_{3g}$ for 5 atoms occupying the 4c site) to 15 modes in total ($2A_g + B_{1g}$ for 5 atoms occupying the 4c site). In these modes, B_{1g} and A_g modes correspond to the vibrations parallel and perpendicular to the crystal's long axis. We experimentally observe 10 major peak modes of these 15 expected modes. Upon performing co-polarized measurements, we observe the persistence of only five peaks. These vibrational modes should therefore correspond to the A_g (vibrations perpendicular to the chain direction) symmetry based on Raman polarization selection rules. On the other hand, in the cross-polarized spectra, the five peaks that decreased in intensity and disappeared are the only ones that were present, thereby establishing the vibrational modes corresponding to these Raman shifts to be in the B_{1g} (vibrations parallel to the chain direction) symmetry.
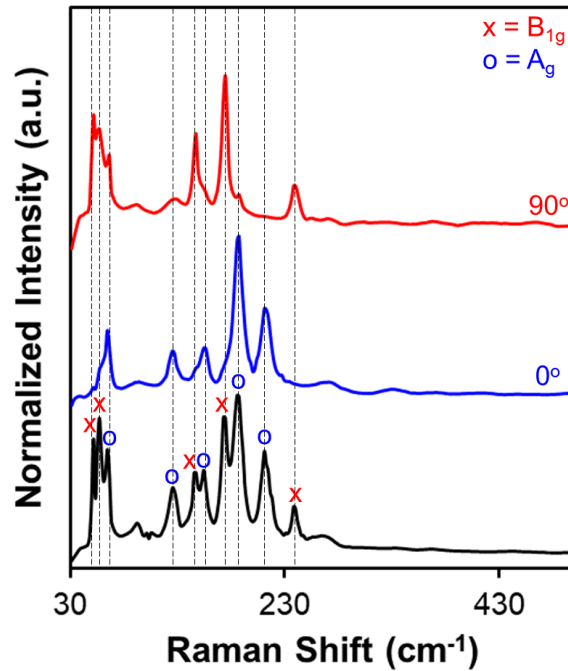
Figure 2.12. Unpolarized, co-polarized, and cross-polarized backscattered Raman spectra of CrSbSe3 single crystal with the symmetry assigned. (A_g: vibrations parallel to the wire direction; B_g: vibrations perpendicular to the wire direction)

57

Table 2.6. Fitting results of major Raman peaks of bulk and exfoliated CrSbSe$_3$.

	Bulk single crystal				Exfoliated nanowires			
Peak position (cm^{-1})	147.2	174.4	186.4	212.8	145.2	172.6	184.5	210.3
FWHM (cm^{-1})	9.86	6.32	13.05	10.05	8.23	7.07	10.48	10.67
Symmetry mode	A$_g$+B$_g$	B$_g$	A$_g$	A$_g$	A$_g$+B$_g$	B$_g$	A$_g$	A$_g$

2.5.7 Fitting details of the XPS spectra of bulk and exfoliated CrSbSe$_3$
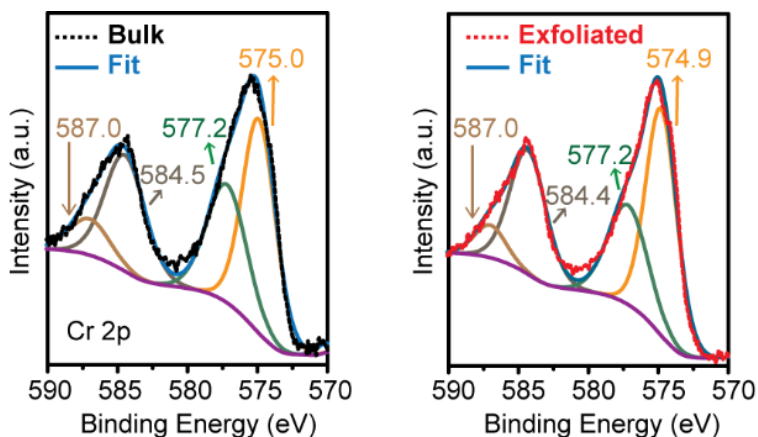
Figure 2.13. Fitting of the Cr *2p* XPS spectra of bulk and exfoliated CrSbSe$_3$
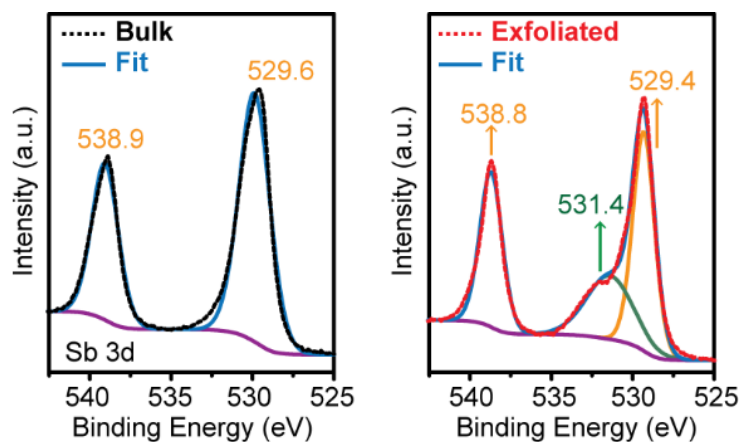
Figure 2.14. Fitting of the Sb *3d* XPS spectra of bulk and exfoliated CrSbSe$_3$

Note: The Sb 3d$_{3/2}$ region of the exfoliated nanowires shows a miniscule shoulder at 532.0 eV which we ascribe to the O1s peak of the residual solvent.
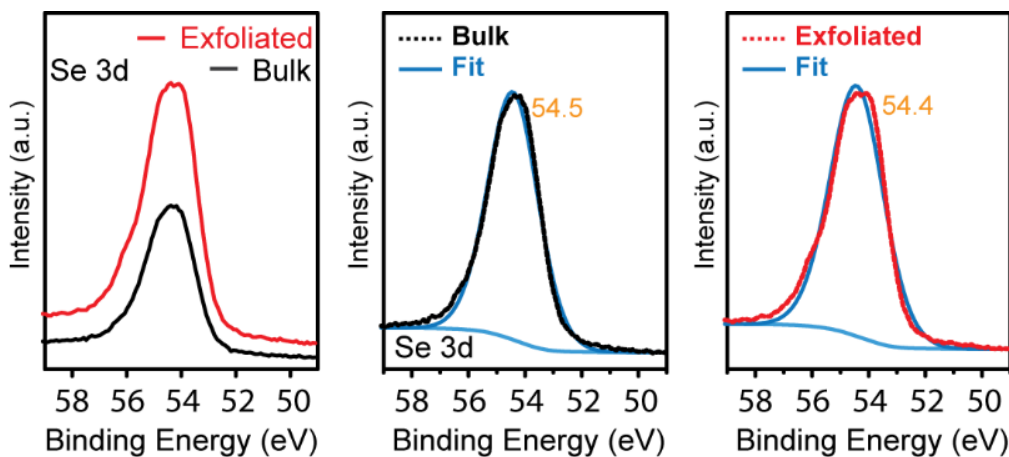
Figure 2.15. Se *3d* XPS spectra of the bulk and exfoliated CrSbSe$_3$ with fitting.

2.5.8. Fitting Details of the Magnetometry Data of Both Bulk and Exfoliated CrSbSe₃

The inverse susceptibility ($1/\chi$) data gathered at low applied field (1000 Oe) were fitted using the modified Curie-Weiss law ($1/\chi = (T-\theta_{cw})/C$). The fitting parameters are shown in **Table 2.7.**

Table 2.7. Parameters derived from the Curie-Weiss fitting of bulk and exfoliated CrSbSe₃.

	Bulk	Exfoliated
Slope	0.4479	0.5436
Intercept	-59.7698	-51.5435
R^2	0.997	0.999
C	2.2326	1.8396
μ_{eff} (μ_B)	4.23	3.84
θ_{cw} (K)	133.4	94.8

References

(1) Dejongh, L. J.; Miedema, A. R., Experiments on Simple Magnetic Model Systems. *Adv. Phys.* **1974,** *23* (1), 1-260.

(2) Steiner, M.; Villain, J.; Windsor, C. G., Theoretical and Experimental Studies on One-Dimensional Magnetic Systems. *Adv. Phys.* **1976,** *25* (2), 87-209.

(3) Li, M. Y. M.; Claire, F. J.; Solomos, M. A.; Tenney, S. M.; Ivanov, S. A.; Siegler, M. A.; Kempa, T. J., Molecular Chains of Coordinated Dimolybdenum Isonicotinate Paddlewheel Clusters. *RSC Adv.* **2019,** *9* (29), 16492-16495.

(4) Bray, J. W.; Hart, H. R.; Interrante, L. V.; Jacobs, I. S.; Kasper, J. S.; Watkins, G. D.; Wee, S. H.; Bonner, J. C., Observation of a Spin-Peierls Transition in a Heisenberg Antiferromagnetic Linear-Chain System. *Phys. Rev. Lett.* **1975,** *35* (11), 744-747.

(5) Maekawa, S., Superconductivity in Spin Ladders. *Science* **1996,** *273* (5281), 1515-1515.

(6) Gschneidner, K. A.; Pecharsky, V. K.; Tsokol, A. O., Recent Developments in Magnetocaloric Materials. *Rep. Prog. Phys.* **2005,** *68* (6), 1479-1539.

(7) Gutfleisch, O.; Willard, M. A.; Bruck, E.; Chen, C. H.; Sankar, S. G.; Liu, J. P., Magnetic Materials and Devices for the 21st Century: Stronger, Lighter, and More Energy Efficient. *Adv. Mater.* **2011,** *23* (7), 821-842.

(8) Yuan, J. Y.; Xu, Y. Y.; Muller, A. H. E., One-dimensional Magnetic Inorganic-organic Hybrid Nanomaterials. *Chem. Soc. Rev.* **2011,** *40* (2), 640-655.

(9) Long, Y. Z.; Yu, M.; Sun, B.; Gu, C. Z.; Fan, Z. Y., Recent Advances in Large-scale Assembly of Semiconducting Inorganic Nanowires and Nanofibers for Electronics, Sensors and Photovoltaics. *Chem. Soc. Rev.* **2012,** *41* (12), 4560-4580.

(10) Caretta, L.; Mann, M.; Buttner, F.; Ueda, K.; Pfau, B.; Gunther, C. M.; Hessing, P.; Churikoval, A.; Klose, C.; Schneider, M.; Engel, D.; Marcus, C.; Bono, D.; Bagschik, K.; Eisebitt, S.; Beach, G. S. D., Fast Current-driven Domain Walls and Small Skyrmions in a Compensated Ferrimagnet. *Nat. Nanotechnol.* **2018,** *13* (12), 1154-1160.

(11) Sun, S. H.; Murray, C. B.; Weller, D.; Folks, L.; Moser, A., Monodisperse FePt Nanoparticles and Ferromagnetic FePt nanocrystal superlattices. *Science* **2000,** *287* (5460), 1989-1992.

(12) Allwood, D. A.; Xiong, G.; Faulkner, C. C.; Atkinson, D.; Petit, D.; Cowburn, R. P., Magnetic domain-wall logic. *Science* **2005,** *309* (5741), 1688-1692.

(13) Zhou, B. H.; Rinehart, J. D., A Size Threshold for Enhanced Magnetoresistance in Colloidally Prepared $CoFe_2O_4$ Nanoparticle Solids. *ACS Cent. Sci.* **2018,** *4* (9), 1222-1227.

(14) Zhou, B. H.; Rinehart, J. D., Pseudo Spin Valve Behavior in Colloidally Prepared Nanoparticle Films. *ACS. Appl. Electron. Mater.* **2019,** *1* (7), 1065-1069.

(15) Stano, M.; Fruchart, O.; Bruck, E., Chapter 3-Magnetic Nanowires and Nanotubes. In *Handbook of Magnetic Materials,* Elsevier: Amsterdam, **2018**; Vol. 27, pp 155-267.

(16) Dasgupta, N. P.; Sun, J. W.; Liu, C.; Brittman, S.; Andrews, S. C.; Lim, J.; Gao, H. W.; Yan, R. X.; Yang, P. D., 25th Anniversary Article: Semiconductor Nanowires Synthesis, Characterization, and Applications. *Adv. Mater.* **2014,** *26* (14), 2137-2184.

(17) Duan, X. F.; Lieber, C. M., General synthesis of compound semiconductor nanowires. *Adv. Mater.* **2000,** *12* (4), 298-302.

(18) Chowdhury, T.; Sadler, E. C.; Kempa, T. J., Progress and Prospects in Transition-Metal Dichalcogenide Research Beyond 2D. *Chem. Rev.* **2020,** *120* (22), 12563-12591.

(19) Cao, G. Z.; Liu, D. W., Template-based synthesis of nanorod, nanowire, and nanotube arrays. *Adv. Colloid. Interfac. Sci.* **2008,** *136* (1-2), 45-64.

(20) Sellmyer, D. J.; Zheng, M.; Skomski, R., Magnetism of Fe, Co and Ni nanowires in self-assembled arrays. *J. Phys.-Condens. Mat.* **2001,** *13* (25), R433-R460.

(21) Kohli, S.; McCurdy, P. R.; Johnson, D. C.; Das, J.; Prieto, A. L.; Rithner, C. D.; Fisher, E. R., Template-Assisted Chemical Vapor Deposited Spinel Ferrite Nanotubes. *J. Phys. Chem. C* **2010,** *114* (46), 19557-19561.

(22) Ross, C. A.; Smith, H. I.; Savas, T.; Schattenburg, M.; Farhoud, M.; Hwang, M.; Walsh, M.; Abraham, M. C.; Ram, R. J., Fabrication of patterned media for high density magnetic storage. *J. Vac. Sci. Technol. B* **1999,** *17* (6), 3168-3176.

(23) Gambardella, P.; Dallmeyer, A.; Maiti, K.; Malagoli, M. C.; Eberhardt, W.; Kern, K.; Carbone, C., Ferromagnetism in one-dimensional monatomic metal chains. *Nature* **2002,** *416* (6878), 301-304.

(24) Huang, F.; Kief, M. T.; Mankey, G. J.; Willis, R. F., Magnetism in the Few-Monolayers Limit - a Surface Magnetooptic Kerr-Effect Study of the Magnetic-Behavior of Ultrathin Films of Co, Ni, and Co-Ni Alloys on Cu(100) and Cu(111). *Phys. Rev. B* **1994,** *49* (6), 3962-3971.

(25) Kim, T.; Chamberlin, R. V.; Bird, J. P., Large Magnetoresistance of Nickel-Silicide Nanowires: Non-Equilibrium Heating of Magnetically-Coupled Dangling Bonds. *Nano Lett.* **2013,** *13* (3), 1106-1110.

(26) Seo, K.; Varadwaj, K. S. K.; Mohanty, P.; Lee, S.; Jo, Y.; Jung, M. H.; Kim, J.; Kim, B., Magnetic properties of single-crystalline CoSI nanowires. *Nano Lett.* **2007,** *7* (5), 1240-1245.

(27) Hung, S. W.; Wang, T. T. J.; Chu, L. W.; Chen, L. J., Orientation-Dependent Room-Temperature Ferromagnetism of FeSi Nanowires and Applications in Nonvolatile Memory Devices. *J. Phys. Chem. C* **2011,** *115* (31), 15592-15597.

(28) Tanase, M.; Silevitch, D. M.; Hultgren, A.; Bauer, L. A.; Searson, P. C.; Meyer, G. J.; Reich, D. H., Magnetic trapping and self-assembly of multicomponent nanowires. *J. Appl. Phys.* **2002,** *91* (10), 8549-8551.

(29) Jorritsma, J.; Mydosh, J. A., Temperature-dependent magnetic anisotropy in Ni nanowires. *J. Appl. Phys.* **1998,** *84* (2), 901-906.

(30) Topolovsek, P.; Gadermaier, C.; Vengust, D.; Strojnik, M.; Strle, J.; Mihailovic, D., Unlocking the Functional Properties in One-Dimensional MoSI Cluster Polymers by Doping and Photoinduced Charge Transfer. *Nano Lett.* **2015,** *15* (2), 813-818.

(31) Celic, N.; Pavlica, E.; Borovsak, M.; Strle, J.; Buh, J.; Zavasnik, J.; Bratina, G.; Denk, P.; Scharber, M.; Sariciftci, N. S.; Mihailovic, D., Factors determining large observed increases in power conversion efficiency of P3HT:PCBM solar cells embedded with $Mo_6S_{9-x}I_x$ nanowires. *Synthetic Met.* **2016,** *212*, 105-112.

(32) Chae, S.; Oh, S.; Choi, K. H.; Jeon, J.; Liu, Z. X.; Wang, C.; Lim, C.; Dong, X.; Woo, C.; Asghar, G.; Chang, J.; Nurunnabi, M.; Kang, J.; Song, S. Y.; Yu, H. K.; Choi, J. Y., Aqueous Dispersion of One-Dimensional van der Waals Material $Mo_6S_3I_6$ with the Charge Type of the Hydrophobic Dispersant Tail. *ACS Appl. Bio. Mater.* **2020,** *3* (7), 3992-3998.

(33) Lin, H.; Cheng, H. M.; Liu, L.; Zhu, Z. W.; Shao, Y. H.; Papakonstantinou, P.; Mihailovic, D.; Li, M. X., Thionin attached to a gold electrode modified with self-assembly of $Mo_6S_{9-x}I_x$ nanowires for amplified electrochemical detection of natural DNA. *Biosens. Bioelectron.* **2011,** *26* (5), 1866-1870.

(34) Pfister, D.; Schafer, K.; Ott, C.; Gerke, B.; Pottgen, R.; Janka, O.; Baumgartner, M.; Efimova, A.; Hohmann, A.; Schmidt, P.; Venkatachalam, S.; van Wullen, L.; Schurmann, U.; Kienle, L.; Duppel, V.; Parzinger, E.; Miller, B.; Becker, J.; Holleitner, A.; Weihrich, R.; Nilges, T., Inorganic Double Helices in Semiconducting SnIP. *Adv. Mater.* **2016,** *28* (44), 9783-9791.

(35) Chae, S.; Siddiqa, A. J.; Kim, B. J.; Oh, S.; Choi, K. H.; Lee, K. H.; Kim, H. Y.; Yu, H. K.; Choi, J. Y., Isolation of inorganic molecular chains from rod-like bulk V_2Se_9 crystal by liquid exfoliation. *RSC Adv.* **2018,** *8* (62), 35348-35352.

(36) Lee, W. G.; Sung, D.; Lee, J.; Chung, Y. K.; Kim, B. J.; Choi, K. H.; Lee, S. H.; Jeong, B. J.; Choi, J. Y.; Huh, J., Tuning the electronic properties of highly anisotropic 2D dangling-bond-free sheets from 1D V_2Se_9 chain structures. *Nanotechnology* **2021,** *32* (9), 095203.

(37) Ploscaru, M. I.; Kokalj, S. J.; Uplaznik, M.; Vengust, D.; Turk, D.; Mrzel, A.; Mihailovic, D., Mo6S9-xIx nanowire recognitive molecular-scale connectivity. *Nano Lett.* **2007,** *7* (6), 1445-1448.

(38) Vrbanic, D.; Pejovnik, S.; Mihailovic, D.; Kutnjak, Z., Electrical conductivity of $Mo_6S_3I_6$ and $Mo_6S_{4.5}I_{4.5}$ nanowires. *J. Eur. Ceram. Soc.* **2007,** *27* (2-3), 975-978.

(39) Andzane, J.; Prikulis, J.; Dvorsek, D.; Mihailovic, D.; Erts, D., Two-terminal nanoelectromechanical bistable switches based on molybdenum-sulfur-iodine molecular wire bundles. *Nanotechnology* **2010,** *21* (12), 125706.

(40) Uplaznik, M.; Bercic, B.; Remskar, M.; Mihailovic, D., Quantum charge transport in $Mo_6S_3I_6$ molecular wire circuits. *Phys. Rev. B* **2009**, *80* (8), 085402.

(41) Strle, J.; Vengust, D.; Mihailovic, D., Inorganic Molecular-Scale MoSI Nanowire-Gold Nanoparticle Networks Exhibit Self-Organized Critical Self-Assembly. *Nano Lett.* **2009**, *9* (3), 1091-1095.

(42) Chae, S.; Oh, S.; Choi, K. H.; Lee, J. W.; Jeon, J.; Liu, Z. X.; Wang, C.; Woo, C.; Shi, L. Y.; Kang, J.; Song, S. Y.; Kim, S. J.; Lee, J. H.; Yu, H. K.; Choi, J. Y., Aqueous dispersion of 1D van der Waals $Mo_6S_3I_6$ crystal using biocompatible tri-block copolymer. *Ceram. Int.* **2021**, *47* (9), 11935-11941.

(43) Lee, J. W.; Chae, S.; Oh, S.; Kim, S. H.; Choi, K. H.; Meeseepong, M.; Chang, J.; Kim, N.; Kim, Y. H.; Lee, N. E.; Lee, J. H.; Choi, J. Y., Single-Chain Atomic Crystals as Extracellular Matrix-Mimicking Material with Exceptional Biocompatibility and Bioactivity. *Nano Lett.* **2018**, *18* (12), 7619-7627.

(44) Itzhaik, Y.; Niitsoo, O.; Page, M.; Hodes, G., Sb_2S_3-Sensitized Nanoporous TiO_2 Solar Cells. *J. Phys. Chem. C* **2009**, *113* (11), 4254-4256.

(45) Majkic, A.; Gadermaier, C.; Celic, N.; Topolovsek, P.; Bratina, G.; Mihailovic, D., $Mo_6S_{9-x}I_x$ nanowires as additives for enhanced organic solar cell performance. *Sol. Energ. Mat. Sol. C* **2014**, *127*, 63-66.

(46) Webber, D. H.; Brutchey, R. L., Alkahest for V2VI3 Chalcogenides: Dissolution of Nine Bulk Semiconductors in a Diamine-Dithiol Solvent Mixture. *J. Am. Chem. Soc.* **2013**, *135* (42), 15722-15725.

(47) Webber, D. H.; Buckley, J. J.; Antunez, P. D.; Brutchey, R. L., Facile dissolution of selenium and tellurium in a thiol-amine solvent mixture under ambient conditions. *Chem. Sci.* **2014**, *5* (6), 2498-2502.

(48) Sayettat, J.; Bull, L. M.; Jobic, S.; Gabriel, J. C. P.; Fourmigue, M.; Batail, P.; Brec, R.; Inglebert, R. L.; Sourisseau, C., Behaviour of the one-dimensional, inorganic polymer $^{1\infty}[MPS_4]^-$ anions (M = Ni, Pd) in organic solutions. *J. Mater. Chem.* **1999**, *9* (1), 143-153.

(49) Tarascon, J. M.; Disalvo, F. J.; Chen, C. H.; Carroll, P. J.; Walsh, M.; Rupp, L., First Example of Monodispersed $(Mo_3Se_3)^{1\infty}$ Clusters. *J. Solid. State. Chem.* **1985**, *58* (3), 290-300.

(50) Gong, C.; Li, L.; Li, Z. L.; Ji, H. W.; Stern, A.; Xia, Y.; Cao, T.; Bao, W.; Wang, C. Z.; Wang, Y. A.; Qiu, Z. Q.; Cava, R. J.; Louie, S. G.; Xia, J.; Zhang, X., Discovery of intrinsic ferromagnetism in two-dimensional van der Waals crystals. *Nature* **2017**, *546* (7657), 265-269.

(51) Huang, B.; Clark, G.; Navarro-Moratalla, E.; Klein, D. R.; Cheng, R.; Seyler, K. L.; Zhong, D.; Schmidgall, E.; McGuire, M. A.; Cobden, D. H.; Yao, W.; Xiao, D.; Jarillo-Herrero, P.; Xu, X. D., Layer-dependent ferromagnetism in a van der Waals crystal down to the monolayer limit. *Nature* **2017**, *546* (7657), 270-273.

(52) Burch, K. S.; Mandrus, D.; Park, J. G., Magnetism in two-dimensional van der Waals materials. *Nature* **2018,** *563* (7729), 47-52.

(53) O'Hara, D. J.; Zhu, T. C.; Trout, A. H.; Ahmed, A. S.; Luo, Y. K.; Lee, C. H.; Brenner, M. R.; Rajan, S.; Gupta, J. A.; McComb, D. W.; Kawakami, R. K., Room Temperature Intrinsic Ferromagnetism in Epitaxial Manganese Selenide Films in the Monolayer Limit. *Nano Lett.* **2018,** *18* (5), 3125-3131.

(54) Bonilla, M.; Kolekar, S.; Ma, Y. J.; Diaz, H. C.; Kalappattil, V.; Das, R.; Eggers, T.; Gutierrez, H. R.; Phan, M. H.; Batzill, M., Strong room-temperature ferromagnetism in VSe$_2$ monolayers on van der Waals substrates. *Nat. Nanotechnol.* **2018,** *13* (4), 289-293.

(55) Lee, J. U.; Lee, S.; Ryoo, J. H.; Kang, S.; Kim, T. Y.; Kim, P.; Park, C. H.; Park, J. G.; Cheong, H., Ising-Type Magnetic Ordering in Atomically Thin FePS$_3$. *Nano Lett.* **2016,** *16* (12), 7433-7438.

(56) Song, X. Y.; Yuan, F.; Schoop, L. M., The properties and prospects of chemically exfoliated nanosheets for quantum materials in two dimensions. *Appl. Phys. Rev.* **2021,** *8* (1), 011312.

(57) Song, X. Y.; Cheng, G. M.; Weber, D.; Pielnhofer, F.; Lei, S. M.; Klemenz, S.; Yeh, Y. W.; Filsinger, K. A.; Arnold, C. B.; Yao, N.; Schoop, L. M., Soft Chemical Synthesis of H$_x$CrS$_2$: An Antiferromagnetic Material with Alternating Amorphous and Crystalline Layers. *J. Am. Chem. Soc.* **2019,** *141* (39), 15634-15640.

(58) Djieutedjeu, H.; Lopez, J. S.; Lu, R. M.; Buchanan, B.; Zhou, X. Y.; Chi, H.; Ranmohotti, K. G. S.; Uher, C.; Poudeu, P. F. P., Charge Disproportionation Triggers Bipolar Doping in FeSb$_{2-x}$Sn$_x$Se$_4$ Ferromagnetic Semiconductors, Enabling a Temperature-Induced Lifshitz Transition. *J. Am. Chem. Soc.* **2019,** *141* (23), 9249-9261.

(59) Djieutedjeu, H.; Poudeu, P. F. P.; Takas, N. J.; Makongo, J. P. A.; Rotaru, A.; Ranmohotti, K. G. S.; Anglin, C. J.; Spinu, L.; Wiley, J. B., Structural-Distortion-Driven Cooperative Magnetic and Semiconductor-to-Insulator Transitions in Ferromagnetic FeSb$_2$Se$_4$. *Angew. Chem. Int. Edit.* **2010,** *49* (51), 9977-9981.

(60) Djieutedjeu, H.; Makongo, J. P. A.; Rotaru, A.; Palasyuk, A.; Takas, N. J.; Zhou, X. Y.; Ranmohotti, K. G. S.; Spinu, L.; Uher, C.; Poudeu, P. F. P., Crystal Structure, Charge Transport, and Magnetic Properties of MnSb$_2$Se$_4$. *Eur. J. Inorg. Chem.* **2011,** (26), 3969-3977.

(61) Ranmohotti, K. G. S.; Djieutedjeu, H.; Poudeu, P. F. P., Chemical Manipulation of Magnetic Ordering in Mn$_{1-x}$Sn$_x$Bi$_2$Se$_4$ Solid-Solutions. *J. Am. Chem. Soc.* **2012,** *134* (34), 14033-14042.

(62) Ranmohotti, K. G. S.; Djieutedjeu, H.; Lopez, J.; Page, A.; Haldolaarachchige, N.; Chi, H.; Sahoo, P.; Uher, C.; Young, D.; Poudeu, P. F. P., Coexistence of High-Tc Ferromagnetism and n-Type Electrical Conductivity in FeBi$_2$Se$_4$. *J. Am. Chem. Soc.* **2015,** *137* (12), 4274-4274.

(63) Kong, T.; Stolze, K.; Ni, D. R.; Kushwaha, S. K.; Cava, R. J., Anisotropic magnetic properties of the ferromagnetic semiconductor CrSbSe$_3$. *Phys. Rev. Mater.* **2018,** *2* (1), 014410.

(64) Odink, D. A.; Carteaux, V.; Payen, C.; Ouvrard, G., Synthesis and Structure of CrSbSe$_3$ - a Pseudo-One-Dimensional Ferromagnet. *Chem. Mater.* **1993,** *5* (2), 237-240.

(65) OBarr, R.; Schultz, S., Switching field studies of individual single domain Ni columns. *J. Appl. Phys.* **1997,** *81* (8), 5458-5460.

(66) Balan, A. P.; Radhakrishnan, S.; Woellner, C. F.; Sinha, S. K.; Deng, L. Z.; de los Reyes, C.; Rao, B. M.; Paulose, M.; Neupane, R.; Apte, A.; Kochat, V.; Vajtai, R.; Harutyunyan, A. R.; Chu, C. W.; Costin, G.; Galvao, D. S.; Marti, A. A.; van Aken, P. A.; Varghese, O. K.; Tiwary, C. S.; Iyer, A. M. M. R.; Ajayan, P. M., Exfoliation of a non-van der Waals material from iron ore hematite. *Nat. Nanotechnol.* **2018,** *13* (7), 602-609.

(67) Backes, C.; Higgins, T. M.; Kelly, A.; Boland, C.; Harvey, A.; Hanlon, D.; Coleman, J. N., Guidelines for Exfoliation, Characterization and Processing of Layered Materials Produced by Liquid Exfoliation. *Chem. Mater.* **2017,** *29* (1), 243-255.

(68) Shen, J. F.; He, Y. M.; Wu, J. J.; Gao, C. T.; Keyshar, K.; Zhang, X.; Yang, Y. C.; Ye, M. X.; Vajtai, R.; Lou, J.; Ajayan, P. M., Liquid Phase Exfoliation of Two-Dimensional Materials by Directly Probing and Matching Surface Tension Components. *Nano Lett.* **2015,** *15* (8), 5449-5454.

(69) Wang, M.; Xu, X. W.; Ge, Y. C.; Dong, P.; Baines, R.; Ajayan, P. M.; Ye, M. X.; Shen, J. F., Surface Tension Components Ratio: An Efficient Parameter for Direct Liquid Phase Exfoliation. *ACS Appl. Mater. Inter.* **2017,** *9* (10), 9168-9175.

(70) Halim, U.; Zheng, C. R.; Chen, Y.; Lin, Z.; Jiang, S.; Cheng, R.; Huang, Y.; Duan, X., A rational design of cosolvent exfoliation of layered materials by directly probing liquid-solid interaction. *Nat. Commun.* **2013,** *4*, 2213.

(71) Shen, J. F.; Wu, J. J.; Wang, M.; Dong, P.; Xu, J. X.; Li, X. G.; Zhang, X.; Yuan, J. H.; Wang, X. F.; Ye, M. X.; Vajtai, R.; Lou, J.; Ajayan, P. M., Surface Tension Components Based Selection of Cosolvents for Efficient Liquid Phase Exfoliation of 2D Materials. *Small* **2016,** *12* (20), 2741-2749.

(72) Jia, X.; Lin, Z.; Zhang, T.; Puthen-Veettil, B.; Yang, T.; Nomoto, K.; Ding, J.; Conibeer, G.; Perez-Wurfl, I., Accurate analysis of the size distribution and crystallinity of boron doped Si nanocrystals via Raman and PL spectra. *RSC Adv.* **2017,** *7* (54), 34244-34250.

(73) Ramaraj, S.; Mani, S.; Chen, S. M.; Palanisamy, S.; Velusamy, V.; Hall, J. M.; Chen, T. W.; Tseng, T. W., Hydrothermal Synthesis of Cr$_2$Se$_3$ Hexagons for Sensitive and Low-level Detection of 4-Nitrophenol in Water. *Sci. Rep.* **2018,** *8*, 4839.

(74) Biesinger, M. C.; Payne, B. P.; Grosvenor, A. P.; Lau, L. W. M.; Gerson, A. R.; Smart, R. S., Resolving surface chemical states in XPS analysis of first row transition metals, oxides and hydroxides: Cr, Mn, Fe, Co and Ni. *Appl. Surf. Sci.* **2011,** *257* (7), 2717-2730.

(75) Liu, X. S.; Chen, J.; Luo, M.; Leng, M. Y.; Xia, Z.; Zhou, Y.; Qin, S. K.; Xue, D. J.; Lv, L.; Huang, H.; Niu, D. M.; Tang, J., Thermal Evaporation and Characterization of Sb$_2$Se$_3$ Thin Film for Substrate Sb$_2$Se$_3$/CdS Solar Cells. *ACS Appl. Mater. Inter.* **2014,** *6* (13), 10687-10695.

(76) Park, B. C.; Kim, Y. K., Synthesis, microstructure, and physical properties of metallic barcode nanowires. *Met. Mater. Int.* **2017,** *23* (3), 413-425.

(77) Sun, L.; Hao, Y.; Chien, C. L.; Searson, P. C., Tuning the properties of magnetic nanowires. *IBM J. Res. Dev.* **2005,** *49* (1), 79-102.

(78) Pignard, S.; Goglio, G.; Radulescu, A.; Piraux, L.; Dubois, S.; Declemy, A.; Duvail, J. L., Study of the magnetization reversal in individual nickel nanowires. *J. Appl. Phys.* **2000,** *87* (2), 824-829.

(79) Zhang, R. J.; Willis, R. F., Thickness-dependent Curie temperatures of ultrathin magnetic films: Effect of the range of spin-spin interactions. *Phys. Rev. Lett.* **2001,** *86* (12), 2665-2668.

(80) Tan, C.; Lee, J.; Jung, S. G.; Park, T.; Albarakati, S.; Partridge, J.; Field, M. R.; McCulloch, D. G.; Wang, L.; Lee, C., Hard magnetic properties in nanoflake van der Waals Fe_3GeTe_2. *Nat. Commun.* **2018,** *9,* 1554.

(81) Londono-Calderon, C. L.; Moscoso-Londono, O.; Muraca, D.; Arzuza, L.; Carvalho, P.; Pirota, K. R.; Knobel, M.; Pampillo, L. G.; Martinez-Garcia, R., Synthesis and magnetic properties of cobalt-iron/cobalt-ferrite soft/hard magnetic core/shell nanowires. *Nanotechnology* **2017,** *28* (24), 245605.

(82) Schlorb, H.; Uhlemann, M.; Haehnel, V.; Iselt, D.; Gebert, A., Electrodeposition of Fe-based Magnetic Alloy Nanowires. *Z. Phys. Chem.* **2013,** *227* (8), 1071-1082.

(83) Yang, W.; Cui, C. X.; Sun, J. B.; Wang, B. L., Fabrication and magnetic properties of Fe_3Co_7 alloy nanowire arrays. *J. Mater. Sci.* **2010,** *45* (6), 1523-1527.

(84) Li, C. L.; Wu, Q.; Yue, M.; Xu, H. H.; Palaka, S.; Elkins, K.; Liu, J. P., Manipulation of morphology and magnetic properties in cobalt nanowires. *AIP Adv.* **2017,** *7* (5), 056422.

(85) Tejada, J.; Zhang, X. X.; Hernandez, J. M., Magnetic Viscosity and Hysteresis Phenomena. In *Magnetic Hysteresis in Novel Magnetic Materials;* Hadjipanayis, G. C., Eds.; Springer: Dordrecht, **1997**; Vol. 338, pp 221-232.

(86) Kardar, M., *Statistical Physics of Fields*. Cambridge University Press: 2012.

(87) Tang, Z. X.; Sorensen, C. M.; Klabunde, K. J.; Hadjipanayis, G. C., Size-Dependent Curie-Temperature in Nanoscale $MnFe_2O_4$ Particles. *Phys. Rev. Lett.* **1991,** *67* (25), 3602-3605.

(88) Koon, N. C.; Jonker, B. T.; Volkening, F. A.; Krebs, J. J.; Prinz, G. A., Direct Evidence for Perpendicular Spin Orientations and Enhanced Hyperfine Fields in Ultrathin Fe(100) Films on Ag(100). *Phys. Rev. Lett.* **1987,** *59* (21), 2463-2466.

(89) Childress, J. R.; Chien, C. L.; Jankowski, A. F., Magnetization, Curie-Temperature, and Magnetic-Anisotropy of Strained (111) Ni/Au Superlattices. *Phys. Rev. B* **1992,** *45* (6), 2855-2862.

(90) Li, Y.; Baberschke, K., Dimensional Crossover in Ultrathin Ni(111) Films on W(110). *Phys. Rev. Lett.* **1992,** *68* (8), 1208-1211.

(91) Lopez-Ruiz, R.; Magen, C.; Luis, F.; Bartolome, J., High temperature finite-size effects in the magnetic properties of Ni nanowires. *J. Appl. Phys.* **2012,** *112* (7) 073906.

(92) Sheldrick, G. M., Crystal structure refinement with SHELXL. *Acta. Crystallogr. C: Struct. Chem.* **2015,** *71* (Pt 1), 3-8.

(93) Rodríguez-Carvajal, J., Recent advances in magnetic structure determination by neutron powder diffraction. *Phys. Rev. B: Condens. Mat.* **1993,** *192*, 55-69.

(94) Wills, A. S., A new protocol for the determination of magnetic structures using simulated annealing and representational analysis (SARAh). *Physica B* **2000,** *276*, 680-681.

(95) Perry, C. H.; Agrawal, D. K., Raman Spectrum of Ferroelectric SbSI. *Solid State Commun.* **1970,** *8* (4), 225-230.

Chapter Specific Acknowledgement

Chapter 3

Metamagnetic Transitions in CrSbS$_3$: A Quasi-One-Dimensional van der Waals Antiferromagnet

3.1 Abstract

One-dimensional (1D) or quasi-1D antiferromagnetic (AFM) phases have attracted much attention because of the potential emergence of exotic quantum phenomena (e.g., superconductivity) therein and their promises for spintronic applications. The "ideal" 1D or quasi-1D AFM system, which is free from magnetic exchange pathways between the 1D spin motifs, has not been reported yet. To address this, we designed and synthesized an AFM spin ladder phase CrSbS$_3$ with large van der Waals (vdW) gaps between the quasi-1D spin ladders, where the vdW gaps preclude potential inter-ladder magnetic couplings, give a real quasi-1D magnetic sublattice, and give a 1D crystallographic lattice. Herein, we report the crystal and magnetic structure of CrSbS$_3$, its magnetic responses to varied temperatures and fields, and its structure-magnetism interplay. With powder neutron diffraction, we established the AFM spin ladder feature of CrSbS$_3$ in its ground state. With a systematic magnetometry study, we demonstrated the field-induced ferromagnetic correlations and the metamagnetic transition in CrSbS$_3$. To further understand the metamagnetic transition in CrSbS$_3$, we studied the interplay between the lattice and the magnetic ordering of CrSbS$_3$ through high-resolution Raman spectroscopy and demonstrated a strong spin-phonon coupling therein. Our results suggest the potential of CrSbS$_3$ as a promising platform to study spin ladder phases with AFM ordering, the structure-magnetism relationships of such spin ladder phases, and their physical properties at the nanoscale.

3.2 Introduction

One-dimensional (1D) or quasi-1D antiferromagnetic (AFM) phases (e.g., AFM spin-chains or spin-ladders) are significant for testing various theoretical models such as

superconductivity and quantum spin liquid and for applications such as racetrack memory devices and sensors.[1-4] Ideal 1D AFM systems should feature isolated chains or ladders of spins wherein spin-spin interactions are particularly strong along only one well-defined direction of the space. Currently, people approach such phases by inserting nonmagnetic spacers such as counter ions or organic linkers in between magnetic chains or ladders, which confines the magnetic coupling in 1D spatial units under certain approximations.[5-6] However, strictly speaking, these compounds are not structurally 1D, which may raise problems. From the theoretical point of view, potential magnetic exchange pathways through nonmagnetic separators are still possible and can break the "ideal" 1D magnetism.[7] For technological applications, the strong ionic or covalent interactions between magnetic units in these phases complicate their structural miniaturization and potential nanocomposite fabrication, hindering their applications as spintronics or sensors at the nanoscale.[8]

Recently, by using van der Waals (vdW) gaps rather than ionic or covalent linkers to isolate magnetic motifs, similar limitations have been circumvented in the field of two-dimensional (2D) magnets. The vdW gaps rule out the interlayer superexchange pathways due to the lack of any interlayer bonding and minimize the direct exchanges due to the long interlayer distances. As a result, 2D vdW magnets can be viewed as "ideal" 2D systems both magnetically and structurally and have provided fertile testbeds for theories and precursors for nanostructured devices.[9-10] Inspired by these breakthroughs, we seek to overcome the limitations mentioned above in current 1D or quasi-1D AFM systems by inserting vdW gaps between the antiferromagnetically ordered 1D structural units.

Then the question is how to construct each antiferromagnetically ordered 1D unit. According to the Mermin-Wagner theorem, long-range magnetic ordering at finite temperature is precluded in 1D spin chains and can only be achieved in 2D spin layers when thermal fluctuations are blocked by strong magnetocrystalline anisotropy.[11] Therefore, we seek to obtain an AFM phase where each 1D structural unit is an array of two single chains of magnetic ions (i.e., spin-ladder) and with strong magnetocrystalline anisotropy. The dimensionality of the spin-spin interactions and the magnetic couplings in such a quasi-1D compound is between 1D and 2D and therefore is expected to give more robust magnetic ordering compared to strictly 1D single spin chains. Meanwhile, the lattice is composed of structurally 1D units separated by vdW gaps, allowing for miniaturizations and nanowire fabrications.

A robust ferromagnet $CrSbSe_3$, which has double-rutile chains of edge-sharing $CrSe_6$ octahedra separated by vdW gaps and has Ising-type spins in the ground state, provides a promising lattice framework to start with. Therefore, we aim to create AFM ordering therein. In this lattice, the sign of magnetic coupling between Cr^{3+} is determined by the relative strength of AFM Cr^{3+}–Cr^{3+} direct exchange and ferromagnetic (FM) Cr^{3+}–chalcogen–Cr^{3+} superexchange interactions. Because both the Cr^{3+}–Cr^{3+} distances and the Cr^{3+}–chalcogen–Cr^{3+} bond angles are directly affected by the bridging chalcogen anion, chemical modification of the chalcogen anion can significantly alter the competition between direct exchange and superexchange interactions and consequently, alter the magnetic ground state.[12] With this in mind, we seek to substitute Se in $CrSbSe_3$ with S to decrease the Cr–Cr distances, enhance the AFM direct exchange coupling, and achieve an AFM ground state. Although $CrSbS_3$ was first synthesized in 1994, there is no conclusive study of its magnetic structure, and in fact, this material has been reported as both AFM and FM.[13-16] Such contradictory claims suggest the complication of the magnetic properties of $CrSbS_3$, which, together with the significance and promises of $CrSbS_3$ as a vdW spin-ladder system, calls for a systematic study of its magnetic structure and transitions.

Here, we conducted complementary structural, magnetic, and neutron diffraction measurements on $CrSbS_3$ to elucidate its magnetic ground states and its magnetic behaviors in response to temperature and external field. We demonstrated that $CrSbS_3$ is a zigzag spin ladder system possessing AFM ground state, with superexchange-dominated FM coupling along each rutile chain (leg direction) and direct-exchange-dominated AFM coupling across rutile chains (rug direction). Such a delicate balance between direct exchange and superexchange interactions also results in the sensitivity of the spin alignments of $CrSbS_3$ towards external field. For example, despite the uncanted alignment of spins in the ground state, external field can generate canted spins and short-range FM correlations in $CrSbS_3$ and trigger metamagnetic transitions. Accompanying this metamagnetic transition, we observed discontinuous changes of the phonon energies in $CrSbS_3$, which reveals the strong spin-phonon coupling in this material. In addition, we demonstrated that $CrSbS_3$ could be exfoliated into nanowires with well-defined morphology and high aspect ratios. These findings collectively make $CrSbS_3$ a unique platform for studying the magnetic structure, metamagnetic transitions, and magneto-lattice coupling in 1D antiferromagnets and exploring their potential spintronic applications at the nanoscale.

3.3 Results and Discussions
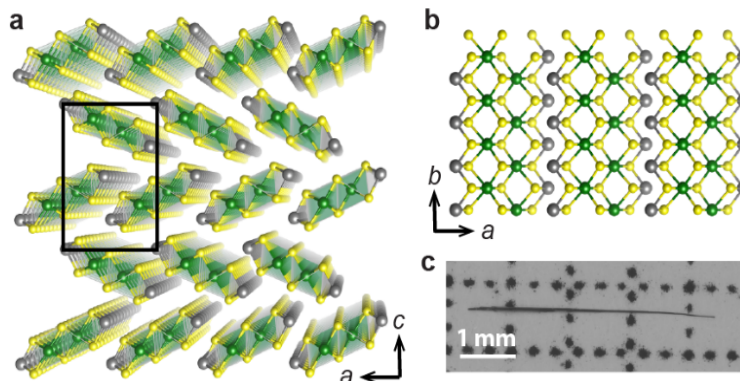
3.3.1 Structure of CrSbS$_3$

Figure 3.1. Crystal Structure of CrSbS$_3$. a) X-ray crystal structure of CrSbS$_3$ at 298 K, with the unit cell outlined in black. **b)** A view of CrSbS$_3$ crystal structure along the *c* direction. **c)** A single crystal of flux-grown CrSbS$_3$. Green, grey, and yellow spheres represent Cr, Sb, and S, respectively.

CrSbS$_3$ crystallizes in the orthorhombic *Pnma* space group and features double-rutile chains of covalently bonded atoms extending along the *b* axis (**Figure 3.1a, b**). The nearest neighbor distance between one Sb atom and the S atom on an adjacent chain, 2.9735(6) Å, is much longer than the sum of their covalent radii 2.43 Å (Sb: 1.40 Å, S: 1.03 Å),[17] evidence of the vdW nature of inter-chain interactions. Bulk CrSbS$_3$ is grown either by typical solid-state melt synthesis, which yields polycrystalline powder, or by flux growth with Sb$_2$S$_3$ as flux, which yields needle-like millimeter-sized single crystals (**Figure 3.1c**, see **3.5.1** for synthesis details). These results collectively demonstrate that CrSbS$_3$, isostructural with CrSbSe$_3$, belongs to the family of quasi-1D vdW materials.[18-19]

3.3.2 Magnetic Structure of CrSbS$_3$

For these quasi-1D vdW magnets, the vdW gaps preclude direct exchange interactions and superexchange pathways between Cr^{3+} belonging to adjacent quasi-1D units. Consequently, their

magnetic ordering is dominated by the exchange coupling within each double-rutile chain. Therefore, to understand the magnetic properties of $CrSbS_3$, we investigated the relationship between the magnetic Cr^{3+} within one double-rutile chain, namely, a single spin ladder. Compared to $CrSbSe_3$, $CrSbS_3$ has significantly shorter Cr–Cr distances both along the rutile chain (leg direction) and across the rutile chain (rug direction) while having similar Cr–chalcogen–Cr bond angles. Such changes are crucial because the magnetic ordering in the quasi-1D units is mediated by two processes: direct exchange through t_{2g} orbitals on Cr^{3+}, which is AFM and sensitive to Cr–Cr distances, and the Cr–chalcogen–Cr superexchange, which is FM and sensitive to the Cr–chalcogen–Cr bond angles, according to the Goodenough-Kanamori-Anderson rule. More importantly, the critical Cr–Cr distance below which AFM direct exchange prevails over FM superexchange has been found to be around 3.6 Å,[12] and the intra-rutile-chain and inter-rutile-chain Cr–Cr distances in $CrSbS_3$ lie on two sides of this critical distance. As a result, we expect AFM coupling across the single rutile chains and an FM coupling along the single rutile chains, which gives an overall AFM ground state of $CrSbS_3$.

To verify this hypothesis, we performed time-of-flight (TOF) powder neutron diffraction to establish the magnetic structure of bulk $CrSbS_3$. The TOF neutron diffraction patterns at 300 K and 11 K, across the ordering temperature of $CrSbS_3$, show significant differences in peak intensities, especially at the high TOF region, suggesting the magnetic contributions to the neutron patterns in bulk $CrSbS_3$ at 11 K. All the magnetic reflections can be indexed on the room-temperature nuclear unit cell with a magnetic propagation vector $\mathbf{k} = (0,0,0)$. Rietveld refinement of these patterns revealed an overall AFM order with magnetic space group $Pnm'a$ (No. 62.444). This magnetic structure consists of FM coupling along each rutile chain and AFM coupling across the rutile chains, agreeing well with our hypothesis based on structural analysis. There is no obvious broadening of the magnetic peaks at 11 K, indicative of a long-range AFM order. Therefore, $CrSbS_3$ can be viewed as a quasi-1D zigzag spin-ladder system, with FM coupling along the leg and AFM coupling along the rug. The absence of the magnetic (100) peak suggests the perfect alignment of all spin moments on Cr^{3+} along the a axis without spin canting, indicative of the magneto-crystalline anisotropy in $CrSbS_3$ and justifies the magnetic ordering therein. The refined moment on Cr ions is 2.66(3) μ_B/Cr, consistent with the ground spin state of Cr^{3+} ($S = 3/2$).
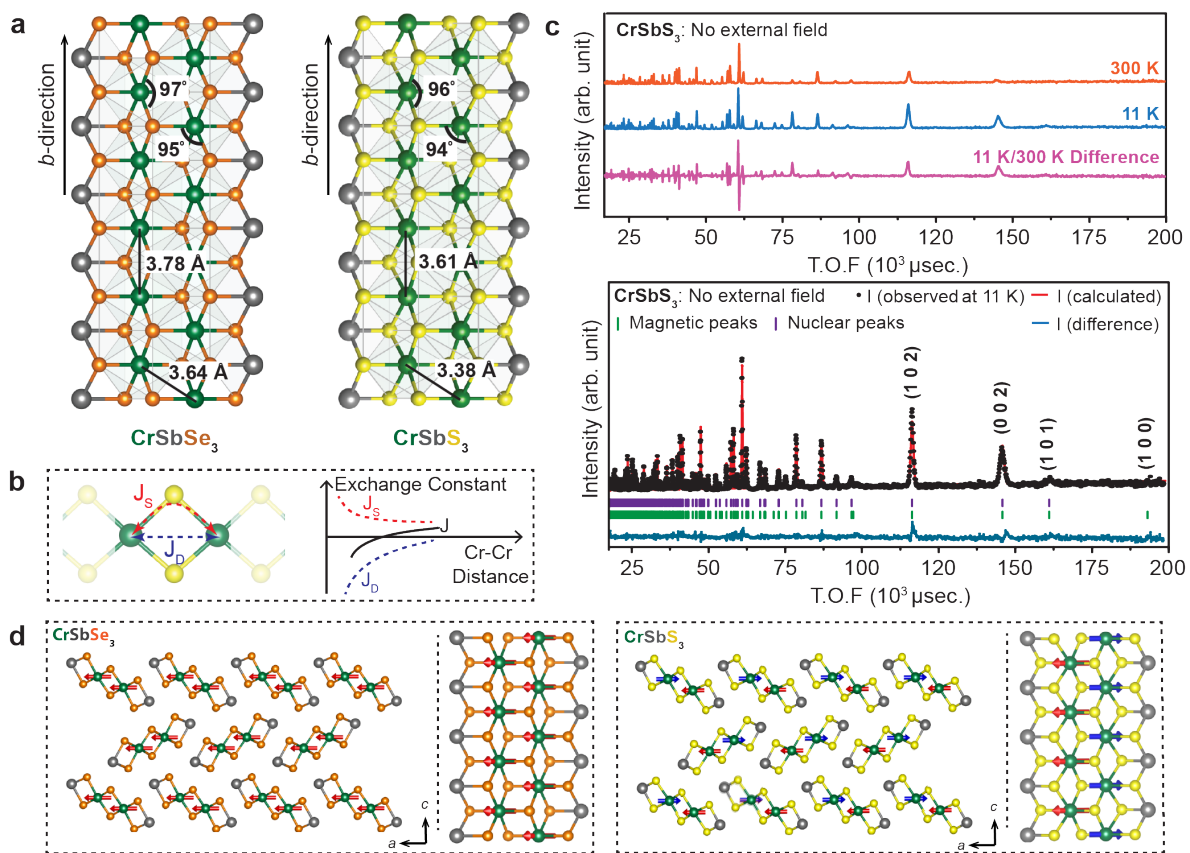
Figure 3.2. Structural relationship between Cr^{3+} and the magnetic structure of the CrSbS₃ lattice. a) Comparison of the Cr^{3+} connections between $CrSbSe_3$ and $CrSbS_3$. **b)** A schematic view of the competition between direct exchange and super-exchange. **c)** Upper panel: Comparison of the neutron diffraction profiles at 11 K (ordered state) and 300 K (paramagnetic state) in the absence of an external magnetic field (up). Lower panel: the final observed (red dots), fitted (black curve) and difference (blue curve) powder neutron diffractograms of bulk $CrSbS_3$ (bottom). Several zone axes of interest are labeled with their respective Miller indices. **d)** The refined magnetic structure of $CrSbS_3$ derived from the powder neutron diffraction profile in comparison to that of $CrSbSe_3$.

This refined moment, together with the XPS data (**Figure 3.3**), reveal that the change of magnetic ground state from $CrSbSe_3$ to $CrSbS_3$ is not induced by the change of electron density on Cr but by structural alteration of the spin-ladder unit, further suggesting the potential of engineering the magnetic states by systematic structural modification in such quasi-1D magnetic lattices.
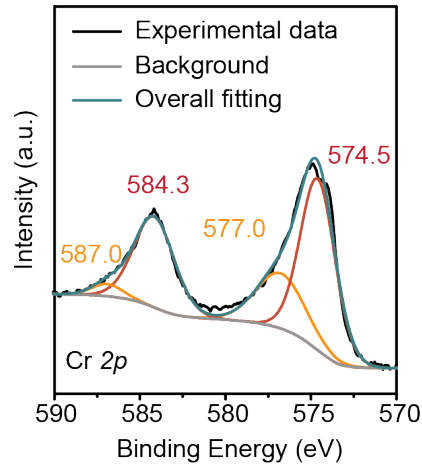
Figure 3.3. Fitting of the Cr *2p* X-ray photoelectron spectroscopy (XPS) data of $CrSbS_3$

3.3.3 Magnetic Properties of CrSbS₃

After establishing the magnetic ground state of $CrSbS_3$, we then studied the magnetic transition of $CrSbS_3$ in response to temperature and field. The temperature-dependent heat capacity of polycrystalline $CrSbS_3$ under no external magnetic field shows a distinct λ-type anomaly at 85 K, indicating the onset of long-range magnetic ordering at 85 K (**Figure 3.4a**). The magnetic susceptibility of polycrystalline $CrSbS_3$ was measured at two different fields over a temperature range of 1.8 K – 300 K. From 120 K to 300 K, both the χ–T curves under 1 kOe and 10 kOe exhibit a Curie-Weiss behavior with a Curie-Weiss constant of +52 K (**Figure 3.4b**). The positive Curie-Weiss constant suggests an external-field-induced FM correlation above the ordering temperature despite the AFM ground state under zero field. Approaching lower temperatures, the susceptibility under 1 kOe increases sharply at ~ 110 K, while this sharp increase of susceptibility disappears with stronger applied field (10 kOe) (**Figure 3.4b**). Such behaviors point to the presence of short-range FM correlations in paramagnetic (PM) matrix. At high external field (10 kOe), the magnetization of the PM matrix in response to the high field prevails over the magnetization of
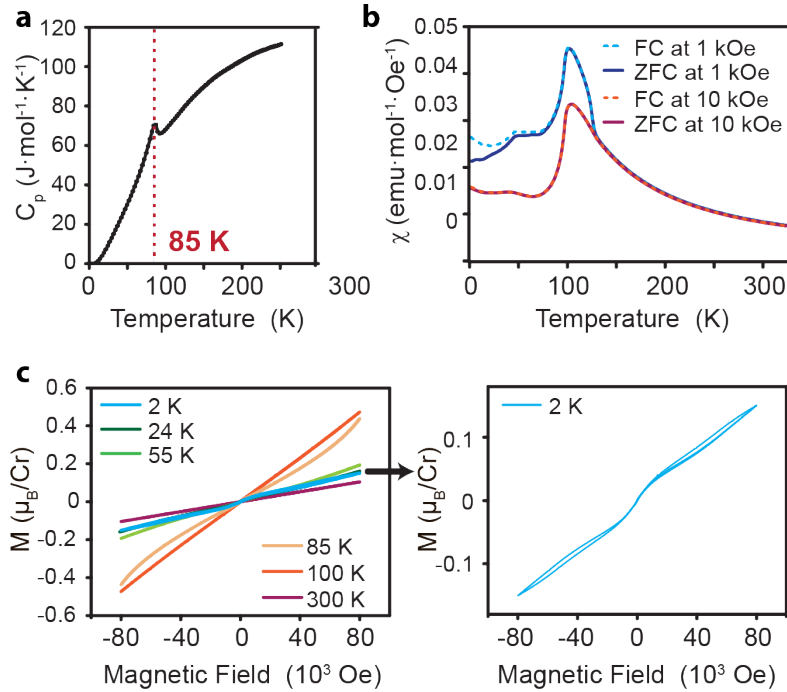
Figure 3.4. Phase transition and magnetic properties of polycrystalline CrSbS₃. a) Heat capacity curve of $CrSbS_3$ under no external field. **b)** Temperature dependence of the field-cooled (FC) and zero field-cooled (ZFC) molar magnetic susceptibility of $CrSbS_3$ under an applied field of 1 kOe and 10 kOe. The dashed lines correspond to the Curie-Weiss fits of the temperature-dependent inverse susceptibilities under 1 kOe. **c)** The M-H data of $CrSbS_3$ under different temperatures with a zoom-in view of the M-H data at 2 K.

the FM clusters, and consequently, no sharp increase of susceptibility is observed, even when FM cluster start to appear. However, at lower field (1 kOe), the magnetization from the PM matrix decreases by roughly 10-fold with the external field, and the FM clusters dominates the magnetization response. Therefore, a sharp transition at ~110 K, corresponding to the turning on of FM short range ordering, is observed in the χ–T. curve. Similar behaviors have been observed in various magnetic systems with short range FM clusters, such as the Griffith phases.[20-22] Moving further to lower temperatures, an onset of a decreasing susceptibility was observed at ~ 85 K, which, together with the heat capacity measurement, suggests the emergence of long-range AFM ordering at 85 K. The observed plateau of χ–T curves below the phase transition temperature 85 K can be attributed to the frozen canted spins or short-range FM clusters, which have higher magnetic moments and mask the lower moments from AFM couplings.[23-25] The formation of these

canted spins and FM are sensitive to the material measurement history and external field. As a result, different bifurcation behaviors between the zero-field-cooled (ZFC) and field-cooled (FC) susceptibilities are observed under different external fields (**Figure 3.4b**). During the cooling process, the application of an external field affects the degree of spin canting and leads to different ordering states at low temperatures. When the sample is warmed up under 1 kOe, this external field is not strong enough to alter the frozen magnetic state, so the difference between ZFC and FC states can be observed. However, an external field of 10 kOe is strong enough to re-arrange the canted spins at low temperatures, thereby diminishing the pre-existing differences between the ZFC state and FC state. As a result, no bifurcation is observed between ZFC and FC χ–T curves under 10 kOe. [23, 26-27]

To further study the formation of FM correlations in $CrSbS_3$ under various fields and temperatures, we measured the isothermal magnetization as a function of magnetic field up to 8 T at several temperatures (**Figure 3.4c**). At 2 K, the magnetization shows a linear-shape increase with increasing field, indicative of an overall AFM ground state (**Figure 3.4c**, right). However, an abrupt increase at low fields (< 1000 Oe) and the wasp-waist hysteresis loops at higher fields suggest the existence of local FM coupling or canted spins and the onset of metamagnetic transitions at higher fields. Similar field dependences and metamagnetic transition can be observed up to 85 K, while at 100 K, the M-H curve becomes almost linear with a higher slope (i.e., susceptibility). This further confirms the onset of AFM coupling below 85 K, the existence of FM clusters between 85 K and 120 K, and the metamagnetic nature of the magnetic transition at 85 K.

3.3.4 Spin-Phonon Coupling in $CrSbS_3$

Such a strong correlation between the magnetic properties of $CrSbS_3$ and external stimuli (e.g., field, temperature) and the potential strain-tunable magnetism theoretically predicted for $CrSbS_3$[13] motivated us to further investigate the interplay between the metamagnetic transition and lattice vibrations (phonons) of $CrSbS_3$. Encouragingly, a strong coupling between phonon dynamics and magnetic ordering has been observed in many 2D AFM phases, leading to a myriad of applications ranging from spintronic devices to quantum information technologies. However, spin-phonon coupling has not been directly demonstrated in quasi-1D vdW antiferromagnets. Such studies are crucial for understanding the magneto-elastic effects and the heat dissipation in quasi-
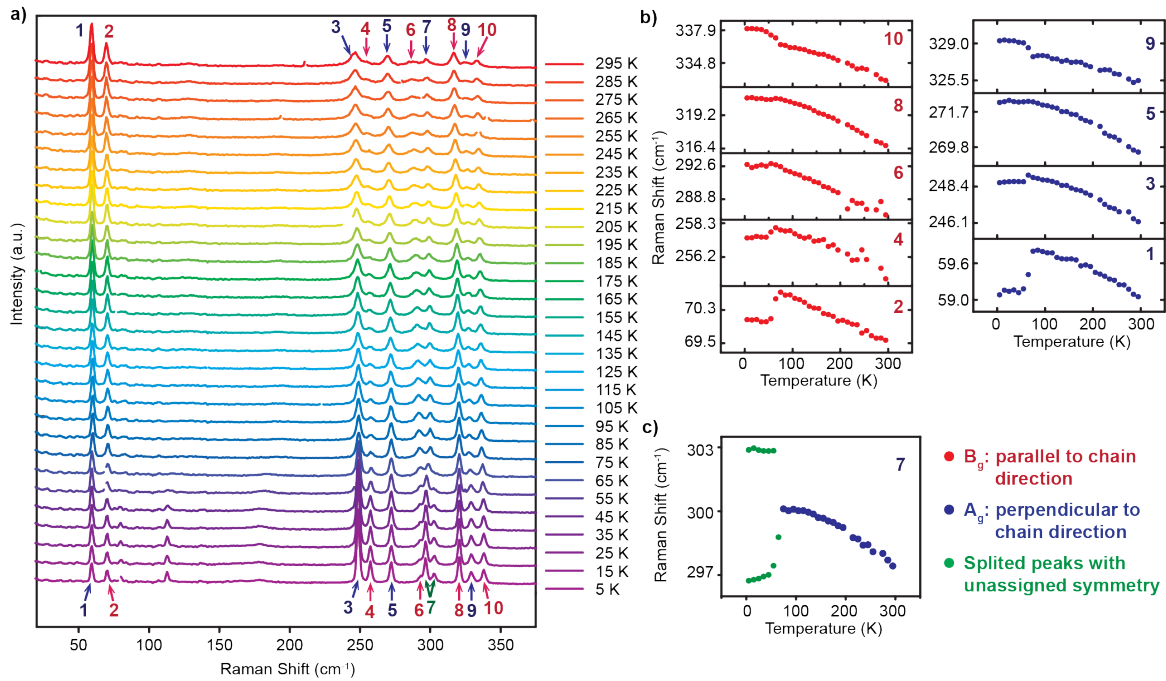
Figure 3.5. Temperature-dependent Raman spectra and the spin-phonon coupling of CrSbS₃. a) Temperature-dependent Raman spectra of $CrSbS_3$ measured in the temperature range of 5 K to 295 K. **b)** Temperature dependence of phonon frequency shifts with the B_g mode on the left and the A_g modes on the right. The number on each panel corresponds to the peak number in **a)**. **c)** The phonon energy splitting of a Raman peak under the ordering temperature.

1D vdW antiferromagnets and developing functional devices based on them such as mechanical sensors. In addition, a demonstrative study of the spin-phonon coupling in bulk $CrSbS_3$ single crystal can provide a spectroscopic tool to elucidate the magnetic transitions of $CrSbS_3$. This is extremely meaningful for antiferromagnetic materials due to their low magnetization, especially at the nanoscale.

For this purpose, we collected high-resolution Raman spectra from 5 K to 295 K to understand the influence of magnetic ordering on lattice vibrational energies. We first probed the vibrational modes and assigned their symmetries by polarized room-temperature Raman spectroscopy (see **3.5.5** for detailed analysis). Then we measured the Raman spectra well above

and below the magnetic transition temperature 85 K (**Figure 3.5a**) and extracted the mode frequencies (i.e., phonon energies) at different temperatures by fitting the Raman spectra (**Figure 3.5b**). The energies of the resolved Raman modes increase gradually with decreasing temperature because the anharmonic phonon-phonon interaction is suppressed at lower temperatures, which typically leads to the hardening of a mode.[28-29] However, on top of this background, we also observed a significant discontinuity in the phonon energy changes as the temperature approaches T_C (**Figure 3.5b**). Such a sudden change of phonon energy upon cooling to T_C is evidence of spin-phonon coupling.[30-31] Another evidence comes from the emergence of an additional mode near T_C (**Figure 3.5c**). Although the exact temperature at which this splitting occurs is difficult to determine precisely due to our spectral resolution, the splitting clearly grows as the temperature is lowered, when the magnetic ordering sets in. This is frequently observed in 3D or 2D magnets when the lifting of time-reversal symmetry upon magnetic ordering leads to the splitting of the phonon modes.[30-31] We want to note that structural transitions induced by magnetic ordering may also trigger discontinuous changes of Raman modes at T_C, but this is not likely in our case because neutron diffraction studies in both the paramagnetic (300 K) and the magnetically ordered phases (11 K) showed no significant differences in the structure (**Table 3.2, Table 3.3**). A significant structural transition at T_C can be further ruled out by the absence of additional phonons or major changes in the spectral symmetries with decreasing temperature. Therefore, these discontinuous changes in phonon energies and the split of a phonon mode at 85 K can be attributed to the spin-phonon coupling in $CrSbS_3$, which allows for the study of magnetism in $CrSbS_3$ from the perspective of phonon behaviors using Raman spectroscopy.

3.3.5 Mechanical Exfoliation of CrSbS₃

Owing to the vdW gaps between the $CrSbS_3$ chain units, single crystals of $CrSbS_3$ can be easily exfoliated by scotch tape into nanowires with uniform morphologies and high aspect ratios. A representative nanowire resulting from such exfoliation measures 20 μm long with a cross-section of 58 nm and has uniform morphology and smooth surface (**Figure 3.6**), similar to the exfoliated nanowires of $CrSbSe_3$. The successful exfoliation of $CrSbS_3$ not only demonstrates the structural uniqueness of this quasi-1D vdW magnet but also shows the prospect of $CrSbS_3$ for nano-scale applications such as antiferromagnet racetrack memories.
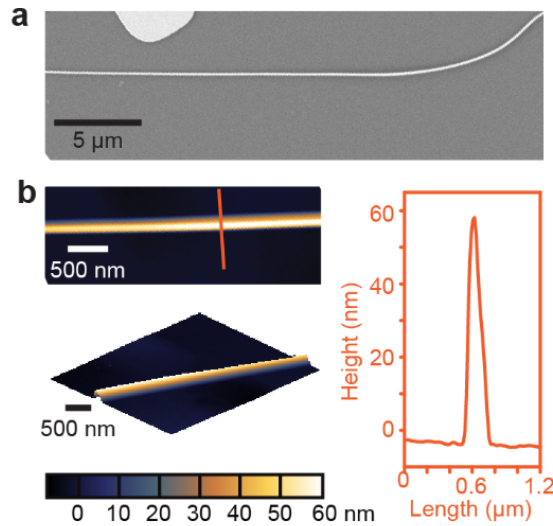
Figure 3.6. A mechanically exfoliated nanowire of CrSbS₃. a) Representative SEM micrograph of the mechanically exfoliated $CrSbS_3$ nanowire on 300 nm SiO_2/Si. **b)** AFM image of a single $CrSbS_3$ nanowire with the corresponding line profile and 3D topographical view.

3.4 Conclusions

In summary, we, for the first time, demonstrated the zero-field magnetic structure of $CrSbS_3$ and unequivocally proved its antiferromagnetic ground state. By carefully studying its structure, we attributed such antiferromagnetic couplings to the short inter-rutile chain Cr^{3+}– Cr^{3+} distances and, thus, the dominant antiferromagnetic Cr^{3+}–Cr^{3+} direct exchange interactions. $CrSbS_3$ exhibits long-range antiferromagnetic ordering below the phase transition temperature of 85 K. At the same time, external magnetic field can generate canted spins or short-range ferromagnetic correlations and disturb the long-range ordering. Such sensitivity to external field

also leads to a metamagnetic transition under external field or at higher temperatures. The magnetic transition of $CrSbS_3$ is closely related to its lattice vibration energies, suggesting a strong spin-phonon coupling therein. These results collectively demonstrate the potential of $CrSbS_3$ as a promising platform to study spin ladder phases with AFM ordering, their multiferroic applications, and their magnetism at the nanoscale.

3.5 Methods

3.5.1 Synthesis of $CrSbS_3$

Single crystals of $CrSbS_3$, used in Raman spectroscopy and mechanical exfoliation, were grown *via* a modified high temperature flux method. Elemental Cr, Sb, and S were mixed in a molar ratio of Cr:Sb:S = 7:33:60. Excess Sb and Se were used as flux, and the mixture was sealed into fused quartz tubes under a pressure of ~ 50 mTorr. The sealed ampoule was first ramped to 550 °C over 3 hours, kept at 550 °C for 6 hours, then ramped to 800 °C over 2 hours, and kept at this temperature for 10 hours. The mixture was then cooled down to 660 °C slowly over 5 days and subsequently centrifuged at this temperature to remove the flux. The small amount of flux remaining on the surface of the crystals was removed by keeping the as-grown crystals at 500 °C for 3 days in a sealed fused quartz ampoule while leaving the cold end of the ampoule at room temperature. Polycrystalline powders of $CrSbS_3$, used for time-of-flight (TOF) powder neutron diffraction, magnetometry, and X-ray photoelectron spectroscopy (XPS), were synthesized via a typical solid-state melt reaction. Starting elements were finely ground, mixed in stoichiometric ratio, and sealed into fused quartz tube under ~50 mTorr. Ampoules were heated to 800 °C over 3 hours and kept at this temperature for 2 days, followed by cooling to room temperature slowly over 5 days. The preparation and handling of all reagents was done under ambient conditions. Chromium (Sigma-Aldrich, 99.5%), antimony (STREM Chemicals, 99.5%), and sulfur (Sigma-Aldrich, 99.98%) were purchased and used without further purification.

3.5.2 Mechanical Exfoliation of CrSbS$_3$ Single Crystals

A piece of CrSbS$_3$ single crystal was first put on a piece of Scotch tape. The tape was then fold and unfold three times, with the crystal being cleaved for each cycle of folding and unfolding. Then the remaining exfoliated fibers were transferred onto a 300nm SiO$_2$/Si substrate for subsequent characterizations.

3.5.3 Characterization Methods

Single crystal X-ray diffraction (SXRD) data of CrSbS$_3$ was collected on sizeable micron-sized crystals using a Bruker D8 diffractometer which is coupled to a Bruker APEX-II CCD detector and a Mo Kα radiation ($\lambda = 0.71073$ Å), performing ϕ- and ω-scans. **The refinement of the structure** was performed using direct methods in the SHELX package and refined against F^2 on all data by full-matrix least squares with SHELXL-13.[32]

The time-of-flight (TOF) powder neutron diffraction data were collected on polycrystalline samples loaded into thin-walled vanadium cans, on the TOF powder diffractometer POWGEN at the Spallation Neutron Source, Oak Ridge National Laboratory. **Structural and magnetic refinements** were performed using the FullProf package.[33] The symmetry-allowed magnetic structures were derived using SARAH representational analysis program.[34]

Magnetometry and heat capacity measurements were performed on powders using a Quantum Design Physical Property Measurement System (PPMS) Dynacool, equipped with a vibrating sample magnetometer (VSM) and a heat capacity option.

The polarized and unpolarized Raman spectra were collected on a homebulilt Raman spectrometer with a 40X long working distance objective, 488 nm excitation line, and 1200 gr/mm grating with a spot size of ~3 μm.

The X-ray photoelectron spectra (XPS) were collected using a Thermo Nexsa X-ray photoelectron spectrometer with a monochromated Al X-ray source.

Scanning electron microscopy (SEM) micrographs were acquired using a Zeiss Field Emission SEM Ultra55.

Atomic force microscopy (AFM) images were acquired on a Cypher Atomic Force Microscope from Asylum Research using silicon probing tips with mid-range mechanical properties (f = 300 kHz, k = 26 N/m) from Oxford Instruments. The scan rates are 0.5-2 Hz depending on the scan size.

3.5.4 Details of the Crystal Structure and Magnetic Structure of Bulk CrSbS$_3$

Table 3.1. Details of the structure determination of CrSbS$_3$ based on single-crystal experiments measured at 300 K

Sum Formula	CrSbSe$_3$
Radiation	λ (Mo-$K\alpha$ = 0.71073 Å)
Index ranges	-16 ≤ h ≤ 16, -6 ≤ k ≤6, -24 ≤ l ≤ 23
Absorption coefficient /mm^{-1}	10.749
Measured reflections	16901
Independent reflections	1565
No. of parameters	31
Goodness-of-fit on F^2	1.025
Final R indices [$I > 2\sigma (I)$]	0.0187
R(int)	0.0387
R(σ)	0.0199
R indices (all data)	0.0253
ωR_2 (all data)	0.0437
Largest diff. peak and hole (e$^-$/ Å^3)	0.901 to -1.192

Table 3.2. Selected crystallographic data of $CrSbS_3$ derived from single-crystal X-ray diffraction (SXRD) measured at 298 K, time-of-flight powder neutron diffraction (TOF PND) measured at 300 K and 10 K.

	SXRD at 298 K	TOF PND at 300 K	TOF PND at 11 K
Crystal System	Orthorhombic	Orthorhombic	Orthorhombic
Space group	P n m a	P n m a	P n m a
Lattice parameter (Å)			
a	8.6451(4)	8.663032	8.560544
b	3.61830(10)	3.617531	3.616786
c	12.8431(6)	12.869816	12.920414
Cell volume ($Å^3$)	401.74(3)	403.32442	400.0374

Table 3.3. Atomic coordinates for $CrSbS_3$ derived from SXRD at 298 K, TOF PND measured at 300 K and 10 K.

	SXRD at 298 K		
Atom	*x*	*y*	*z*
Cr	0.345871	0.250000	0.454653
Sb	0.025488	0.750000	0.339178
S (1)	0.496720	0.250000	0.608139
S (2)	0.212893	0.250000	0.288451
S (3)	0.171256	0.250000	0.510770

TOF PND at 300 K			
Atom	*x*	*y*	*z*
Cr	0.15431	0.25000	0.04556
Sb	0.02553	0.25000	0.66088
S (1)	0.17108	0.25000	0.48938
S (2)	0.28678	0.25000	0.21124
S (3)	0.50185	0.25000	0.60673

TOF PND at 10 K		
x	*y*	*z*
0.15123	0.25000	0.04570
0.02435	0.25000	0.65987
0.17232	0.25000	0.49012
0.28671	0.25000	0.21027
0.50487	0.25000	0.60957
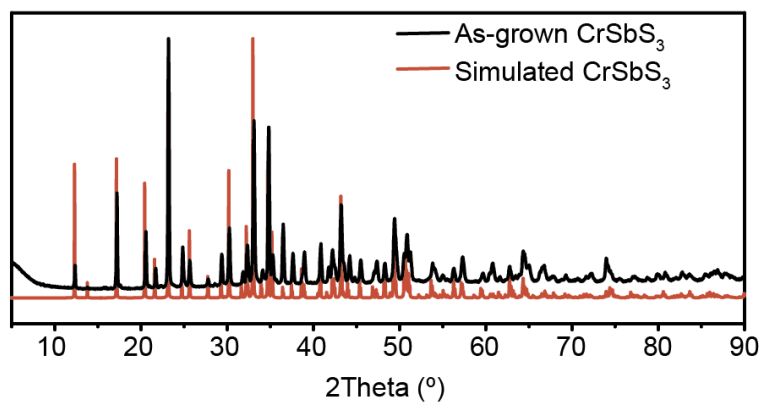
Figure 3.7. Powder X-ray diffraction patterns of as-synthesized $CrSbS_3$ and the theoretical patterns calculated from $CrSbS_3$ single crystal structure.

3.5.5 Symmetry Analysis of Bulk CrSbS$_3$ Single Crystal for Raman Spectroscopy

We performed polarized Raman measurements in the backscattering geometry in order to probe the phonon modes in the CrSbSe$_3$ lattice. In these measurements, we performed (0°) co- and (90°) cross-polarized scattering measurements where the long axis of the crystal is parallel to the laser polarization. We used the standardized unit cell axes ($a \rightarrow a$, $b \rightarrow c$, $c \rightarrow b$), mainly assigning the high-symmetry principal axis from b to c, instead of the experimental single crystal unit cell for coherence and consistency with the group theory analyses. This measurement setup corresponds to the $-X(ZZ)X$ and $-X(YZ)X$ Porto notations for the co- and cross-polarized measurements. Since we are doing only the crystal axes perpendicular to the crystal long axis, in this case, X and Y are interchangeable. This won't affect any of the subsequent selection rules due to the nature of the symmetry. Similar to other orthorhombic crystals that are comprised of isolated chains, with the same *Pnma* space group symmetry,[35] we adopted the simplified C$_{2h}$ point group instead of the D$_{2h}$ point group. By doing this, we simplify and reduce the Raman-active modes from 30 modes ($2A_g + B_{1g} + 2B_{2g} + B_{3g}$ for 5 atoms occupying the 4c site) to 15 modes in total ($2A_g + B_{1g}$ for 5 atoms occupying the 4c site). In these modes, B$_{1g}$ and A$_g$ modes correspond to the vibrations parallel and perpendicular to the crystal's long axis. We experimentally observe 10 major peak modes of these 15 expected modes. Upon performing co-polarized measurements, we observe the persistence of only five peaks. These vibrational modes should therefore correspond to the A$_g$ (vibrations perpendicular to the chain direction) symmetry based on Raman polarization selection rules. On the other hand, in the cross-polarized spectra, we observe the persistence of

only five peaks. These vibrational modes should therefore correspond to the B_{1g} (vibrations parallel to the chain direction) symmetry.
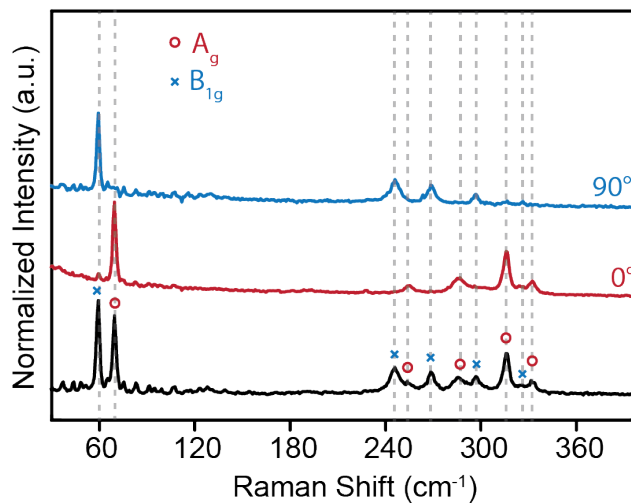
Figure 3.8. Unpolarized, co-polarized, and cross-polarized backscattered Raman spectra of $CrSbSe_3$ single crystal with the symmetry assigned. (A_g: vibrations parallel to the wire direction; B_g: vibrations perpendicular to the wire direction)

References

(1) Tomasello, R.; Puliafito, V.; Martinez, E.; Manchon, A.; Ricci, M.; Carpentieri, M.; Finocchio, G., Performance of synthetic antiferromagnetic racetrack memory: domain wall versus skyrmion. *J. Phys. D: Appl. Phys.* **2017,** *50* (32), 325302.

(2) Caretta, L.; Mann, M.; Buttner, F.; Ueda, K.; Pfau, B.; Gunther, C. M.; Hessing, P.; Churikoval, A.; Klose, C.; Schneider, M.; Engel, D.; Marcus, C.; Bono, D.; Bagschik, K.; Eisebitt, S.; Beach, G. S. D., Fast current-driven domain walls and small skyrmions in a compensated ferrimagnet. *Nat. Nanotechnol.* **2018,** *13* (12), 1154-1160.

(3) Vuletic, T.; Korin-Hamzic, B.; Ivek, T.; Tomic, S.; Gorshunov, B.; Dressel, M.; Akimitsu, J., The spin-ladder and spin-chain system $(La,Y,Sr,Ca)_{14}Cu_{24}O_{41}$: Electronic phases, charge and spin dynamics. *Phys. Rep.* **2006,** *428* (4), 169-258.

(4) Castella, H.; Zotos, X.; Prelovsek, P., Integrability and Ideal Conductance at Finite Temperatures. *Phys. Rev. Lett.* **1995,** *74* (6), 972-975.

(5) Chen, M.; Zhao, H.; Sanudo, E. C.; Liu, C. S.; Du, M., Two isostructural coordination polymers showing diverse magnetic behaviors: weak coupling (Ni-II) and an ordered array of single-chain magnets (Co-II). *Inorg. Chem.* **2016,** *55* (8), 3715-3717.

(6) Masuda, T.; Zheludev, A.; Manaka, H.; Regnault, L. P.; Chung, J. H.; Qiu, Y., Dynamics of composite Haldane spin chains in $IPA-CuCl_3$. *Phys. Rev. Lett.* **2006,** *96* (4), 047210.

(7) Kobayashi, S.; Mitsuda, S.; Ishikawa, M.; Miyatani, K.; Kohn, K., Three-dimensional magnetic ordering in the quasi-one-dimensional Ising magnet $CoNb_2O_6$ with partially released geometrical frustration. *Phys. Rev. B* **1999,** *60* (5), 3331-3345.

(8) Joy, P. A.; Vasudevan, S., Magnetism in the Layered Transition-Metal Thiophosphates MPS_3 (M = Mn, Fe, and Ni). *Phys. Rev. B* **1992,** *46* (9), 5425-5433.

(9) Huang, B.; Clark, G.; Navarro-Moratalla, E.; Klein, D. R.; Cheng, R.; Seyler, K. L.; Zhong, D.; Schmidgall, E.; McGuire, M. A.; Cobden, D. H.; Yao, W.; Xiao, D.; Jarillo-Herrero, P.; Xu, X. D., Layer-dependent ferromagnetism in a van der Waals crystal down to the monolayer limit. *Nature* **2017,** *546* (7657), 270-273.

(10) Gong, C.; Li, L.; Li, Z. L.; Ji, H. W.; Stern, A.; Xia, Y.; Cao, T.; Bao, W.; Wang, C. Z.; Wang, Y. A.; Qiu, Z. Q.; Cava, R. J.; Louie, S. G.; Xia, J.; Zhang, X., Discovery of intrinsic ferromagnetism in two-dimensional van der Waals crystals. *Nature* **2017,** *546* (7657), 265-269.

(11) Mermin, N. D.; Wagner, H., Absence of ferromagnetism or antiferromagnetism in one- or two-dimensional isotropic Heisenberg models. *Phys. Rev. Lett.* **1966,** *17* (22), 1133-1136.

(12) Kobayashi, S.; Ueda, H.; Michioka, C.; Yoshimura, K., Competition between the direct exchange interaction and superexchange interaction in layeredc $LiCrSe_2$, $LiCrTe_2$, and $NaCrTe_2$ with a triangular lattice. *Inorg. Chem.* **2016,** *55* (15), 7407-7413.

(13) Feng, Q. Q.; Li, X. Y.; Li, X. X.; Yang, J. L., $CrSbS_3$ monolayer: a potential phase transition ferromagnetic semiconductor. *Nanoscale* **2021,** *13* (33), 14067-14072.

(14) Mathew, T.; Rahul, K. S.; Mathew, V., Density functional study of magnetic, structural and electronic properties of quasi-one-dimensional compounds $CrSbX_3$ (X = S, Se). *Comput. Condens. Matter* **2020,** *23*, e00467.

(15) Volkov, V. V.; VanTendeloo, G.; VanLanduyt, J.; Amelinckx, S.; Busheva, E. E.; Shabunina, G. G.; Aminov, T. G.; Novotortsev, V. M., HREM image analysis up to structure determination of $SbCrSe_3$: a new 1D ferromagnet. *J Solid State Chem.* **1997,** *132* (2), 257-266.

(16) Jiang, X.; Liu, Q. X.; Xing, J. P.; Liu, N. S.; Guo, Y.; Liu, Z. F.; Zhao, J. J., Recent progress on 2D magnets: Fundamental mechanism, structural design and modification. *Appl. Phys. Rev.* **2021,** *8* (3), 031305.

(17) Brese, N. E.; Okeeffe, M., Bond-Valence Parameters for Solids. *Acta. Crystallogr. B. Struct. Sci. Cryst. Eng. Mater.* **1991,** *47*, 192-197.

(18) Qu, Y.; Arguilla, M. Q.; Zhang, Q.; He, X.; Dinca, M., Ultrathin, High-aspect ratio, and free-standing magnetic nanowires by exfoliation of ferromagnetic quasi-one-dimensional van der Waals lattices. *J. Am. Chem. Soc.* **2021,** *143* (46), 19551-19558.

(19) Kong, T.; Stolze, K.; Ni, D. R.; Kushwaha, S. K.; Cava, R. J., Anisotropic magnetic properties of the ferromagnetic semiconductor $CrSbSe_3$. *Phys. Rev. Mater.* **2018,** *2* (1), 014410.

(20) Zou, M.; Pecharsky, V. K.; Gschneidner, K. A.; Schlagel, D. L.; Lograsso, T. A., Magnetic phase transitions and ferromagnetic short-range correlations in single-crystal $Tb_5Si_{2.2}Ge_{1.8}$. *Phys. Rev. B* **2008,** *78* (1), 014435.

(21) Palakkal, J. P.; Sankar, C. R.; Varma, M. R., Multiple magnetic transitions, Griffiths-like phase, and magnetoresistance in La_2CrMnO_6. *J. Appl. Phys.* **2017,** *122* (7), 073907.

(22) Ouyang, Z. W.; Xia, N. M.; Wu, Y. Y.; Sheng, S. S.; Chen, J.; Xia, Z. C.; Li, L., Short-range ferromagnetic correlations in the spin-chain compound Ca_3CoMnO_6. *Phys Rev B* **2011,** *84* (5), 054435.

(23) Bag, P.; Baral, P. R.; Nath, R., Cluster spin-glass behavior and memory effect in $Cr_{0.5}Fe_{0.5}Ga$. *Phys. Rev. B* **2018,** *98* (14), 144436.

(24) Ederth, J.; Hoel, A.; Johansson, C. I.; Kiss, L. B.; Olsson, E.; Granqvist, C. G.; Nordblad, P., Ag-Mn nanoparticles: Three-dimensional finite size effect of the spin glass state. *J. Appl. Phys.* **1999,** *86* (11), 6571-6575.

(25) Shinaoka, H.; Tomita, Y.; Motome, Y., Effect of magnetoelastic coupling on spin-glass behavior in Heisenberg pyrochlore antiferromagnets with bond disorder (vol 90, 165119, 2014). *Phys. Rev. B* **2014,** *90* (16), 165119.

(26) Zhang, S. Y.; Guo, W. B.; He, Z. Z., Two spin-canted antiferromagnetic orderings and a field-induced metamagnetic transition in $SrMn_2(VO_4)_2(H_2O)_2$. *Dalton T* **2019,** *48* (1), 65-71.

(27) Wu, J.; Zhang, C. L.; Yan, J. M.; Chen, L.; Guo, L.; Chen, T. W.; Gao, G. Y.; Fei, L. F.; Zhao, W. Y.; Chai, Y.; Zheng, R. K., Magnetotransport and magnetic properties of the layered noncollinear antiferromagnetic Cr_2Se_3 single crystals. *J. Phys.: Condens. Matter.* **2020,** *32* (47), 475801.

(28) Upadhyay, U. N.; Sinha, K. P., Phonon-magnon interaction in magnetic crystals. II. Antiferromagnetic systems. *Phys. Rev.* **1963,** *130* (3), 939-944.

(29) Sinha, K. P.; Upadhyaya, U. N., Phonon-magnon Interaction in magnetic crystals. *Phys. Rev.* **1962,** *127* (2), 432-439.

(30) Vermette, J.; Jandl, S.; Gospodinov, M. M., Raman study of spin-phonon coupling in $ErMnO_3$. *J. Phys.: Condens. Matter.* **2008,** *20* (42), 425219.

(31) Tian, Y.; Gray, M. J.; Ji, H. W.; Cava, R. J.; Burch, K. S., Magneto-elastic coupling in a potential ferromagnetic 2D atomic crystal. *2D Mater.* **2016,** *3* (2), 025035.

(32) Sheldrick, G. M., Crystal structure refinement with SHELXL. *Acta. Crystallogr. C: Struct. Chem.* **2015,** *71* (Pt 1), 3-8.

(33) Rodríguez-Carvajal, J., Recent advances in magnetic structure determination by neutron powder diffraction. *Phys. Rev. B: Condens. Mat.* **1993,** *192*, 55-69.

(34) Wills, A. S., A new protocol for the determination of magnetic structures using simulated annealing and representational analysis (SARAh). *Physica B* **2000,** *276*, 680-681.

(35) Perry, C. H.; Agrawal, D. K., Raman Spectrum of Ferroelectric SbSI. *Solid State Commun.* **1970,** *8* (4), 225-230.

Chapter Specific Acknowledgement

Chapter 4

Two Series of Quasi-One-Dimensional van der Waals Magnetic Lattices with Finely Tuned Magnetic Anisotropy

4.1 Abstract

As a consequence of the Mermin-Wagner theorem, a strong magnetic anisotropy is necessary for low-dimensional magnets to display robust long-range magnetic ordering. Despite the diverse set of methods that have been developed to enhance the magnetic anisotropy of two-dimensional (2D) van der Waals (vdW) magnets, there have been no such methodologies applied to quasi-one-dimensional (quasi-1D) vdW magnets. Here, we use the ferromagnetic (FM) $CrSbSe_3$ and antiferromagnetic (AFM) $CrSbS_3$ as representative examples to demonstrate an efficient strategy of tuning magnetic anisotropy in quasi-1D vdW magnets. By partial substitution of Sb by Bi in these phases, we synthesized two series of solid solutions $CrSb_{1-x}Bi_xSe_3$ ($x = 0$, 0.1, 0.2, 0.3, 0.4, 0.5) (**Series 1**) and $CrSb_{1-x}Bi_xS_3$ ($x = 0$, 0.1, 0.2, 0.3, 0.4, 0.5, 0.6) (**Series 2**). While these Bi-alloyed phases maintain the same structure and magnetic ordering as their parent phases, we observe a significant enhancement of magnetic anisotropy with increasing Bi content, as manifested in the increasing coercivity of $CrSb_{1-x}Bi_xSe_3$ and the characteristic spin-flip transitions in $CrSb_{1-x}Bi_xS_3$. These phases have significantly expanded the library of quasi-1D vdW magnets and diversified the magnetic properties exhibited by quasi-1D vdW materials, which are crucial for the systematic investigation of the magnetism within these materials and the realization of quasi-1D magnetic phases with desired magnetic behaviors for technological applications.

4.2 Introduction

Magnetic anisotropy (MA) often plays a central role in various static and dynamic properties of low-dimensional materials. In particular, for two-dimensional (2D) or quasi-one-dimensional (quasi-1D) van der Waals (vdW) magnetic phases, as inferred from the Mermin-Wagner theorem, strong MA is an indispensable prerequisite for magnetic ordering and is crucial for the performance of functional nanodevices based on these materials.[1] Recently, strategies to enhance the magnetic anisotropy of 2D vdW magnets have opened a vast field of possibilities for new physical phenomena and applications such as spintronics and sensors.[2-4] However, such strategies remain rarely explored for quasi-1D vdW magnets, for which enhancing MA is even more critical due to their even lower dimensionality and the much stronger spin fluctuations therein.

Two quasi-1D vdW magnets, the ferromagnetic (FM) $CrSbSe_3$[4-6] and antiferromagnetic (AFM) $CrSbS_3$, provide a promising platform to explore methods for systematically tuning the MA in quasi-1D vdW magnets with distinct magnetic ground states. Both $CrSbSe_3$ and $CrSbS_3$ exhibit MA, evidenced by the uncanted alignment of Ising-type spins along the crystallographic a aixs in their zero-field magnetic ground states, which enables their robust long-range magnetic ordering. However, their magnetic anisotropy is weak.[5] $CrSbSe_3$ displays very low coercivity and remanence despite an FM ground state. In $CrSbS_3$, a weak external field can easily create FM correlations or trigger a spin-flop transition, despite the AFM ground state of $CrSbS_3$ under zero field. Such low magnetic anisotropy energies together with the contrasted types of magnetic couplings in these two phases offer great opportunity for us to explore the strategy to enhance the MA of quasi-1D vdW phases without disturbing their original type magnetic ordering, no matter it is ferromagnetic or antiferromagnetic.

There are two key factors that affect MA: the single-ion anisotropy of Cr^{3+} and the exchange anisotropy of Cr–Ch–Cr superexchange (Ch = S, Se). In an ideal octahedral crystal field, Cr^{3+} (t_{2g}^3 configuration with a $^4A_{2g}$ ground state) has no orbital angular momentum, so is unlikely to be the major source of MA in these materials.[7] In addition, altering the single-ion anisotropy of Cr^{3+} herein is unrealistic without significantly changing the structure or magnetic ground state. As a result, we chose to modify the anisotropy of superexchange interactions. Because direct modification to the superexchange bridge (changing from S to Se) dramatically switches the type

of magnetic ordering (from AFM to FM) (see Chapter 3 for details), we hypothesized that partial substitution of the Sb sites with another pnictogen would affect the exchange anisotropy without disturbing the magnetic ordering or 1D structural nature. Although the Sb site does not directly participate in the superexchange coupling, the composition here determines the covalency of the pnicogen–chalcogen bonds and the energies of the chalcogen p orbitals, which are crucial for the charge transfer between Cr and chalcogen, and thus the superexchange interactions.[8] In addition, the orbital moments on pnictogen still contribute to the overall spin-orbital coupling, therefore affecting MA.[7, 9-11] Such effects have been observed in various systems, especially 2D vdW magnets such as $Cr_2Si_2Te_6$, $Cr_2Ge_2Te_6$,[8] $MnBi_2Se_4$, and $MnSb_2Se_4$.[9] With this in mind, we chose to enhance the MA in quasi-1D vdW magnets $CrSbSe_3$ and $CrSbS_3$ without altering their magnetic ground states by systematically alloying heavier Bi atoms into the Sb sites.

Herein, we report the synthesis, structures, and magnetic properties of $CrSb_{1-x}Bi_xSe_3$ ($x = 0, 0.1, 0.2, 0.3, 0.4, 0.5$) (**Series 1**) and $CrSb_{1-x}Bi_xS_3$ ($x = 0, 0.1, 0.2, 0.3, 0.4, 0.5, 0.6$) (**Series 2**). We found that although the unit cells are slightly altered, both series inherit the quasi-1D structural nature from and remain isostructural with their unalloyed parent phases, indicating a great lattice tolerance of $CrSbSe_3$ and $CrSbS_3$ for heavy atom alloying. Furthermore, all **Series 1** phases exhibit FM ground state and all **Series 2** phases exhibit AFM ground state, suggesting the persistence of magnetic ground states (i.e., type of magnetic ordering) in these phases in response to Bi alloying. Despite the minimally altered structures and ground states, Bi alloying drastically enhances the MA of these phases and changes magnetic behaviors. For example, $CrSb_{0.5}Bi_{0.5}Se_3$ is a ferromagnet with a 10-fold enhanced coercivity compared to $CrSbSe_3$, and $CrSb_{0.4}Bi_{0.6}S_3$ is an antiferromagnet with characteristic spin-flip transitions rather than the spin-flop transitions in $CrSbS_3$. These results not only significantly expand the library of quasi 1D vdW magnets and diversifies their magnetic properties, but also are the signature of efficient control over the MA in quasi-1D vdW magnets while maintaining the structures and magnetic ground states.

4.3. Results and Discussions

4.3.1 Compositions and Structures.

4.3.1.1 Parent Compounds CrSbSe$_3$ and CrSbS$_3$

The parent compounds CrSbSe$_3$ and CrSbS$_3$ are isostructural, crystallizing in the orthorhombic *Pnma* space group, and feature 1D units that propagate down the *b* axis separated by large vdW gaps (**Figure 4.1a**). Each 1D unit is a double-rutile chain of covalently bonded atoms where the magnetic ions (Cr^{3+}) are in the center of the two columns of edge-sharing octahedra. The Sb atoms bind three chalcogenides (S or Se) in a trigonal pyramidal geometry and form the edge of the double-rutile chains (**Figure 4.1b**). The magnetic behaviors of CrSbSe$_3$ and CrSbS$_3$ are dominated by the magnetic exchange interactions within each quas-1D unit while the inter-unit interactions are weak. The intra-unit interactions are determined by the competition between the AFM Cr–Cr direct exchange and the FM Cr–Ch–Cr (Ch = S, Se) superexchange couplings. For CrSbSe$_3$, the Cr–Cr distances along and across rutile chains within each 1D unit are too long for efficient direct exchange, therefore the FM superexchange coupling gives an FM ground state.[5, 12] For CrSbS$_3$, the Cr–S–Cr angle of 94° still gives rise to FM superexchange couplings along the
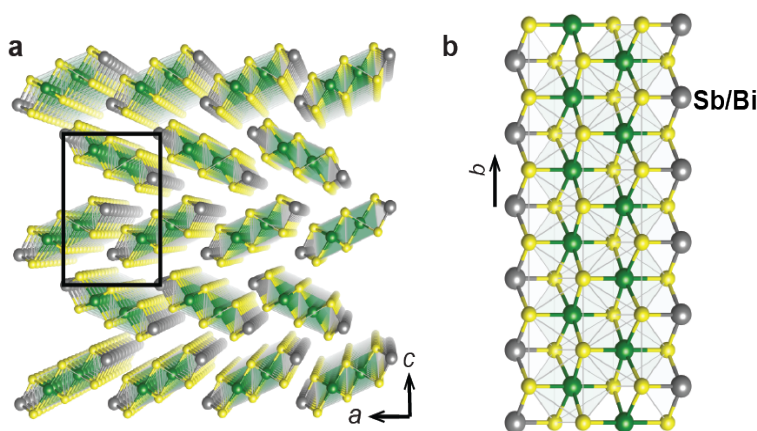
Figure 4.1. Structure and coordination schemes of CrSb$_{1-x}$Bi$_x$Se$_3$ and CrSb$_{1-x}$Bi$_x$S$_3$.
a) Schematic representation of the crystal structure of CrSb$_{1-x}$Bi$_x$Se$_3$ and CrSb$_{1-x}$Bi$_x$S$_3$ with labeled unit cell (black square). **b)** Structure of one quasi-1D unit with labeled Sb/Bi sites.

rutile chains. However, the noticeably shorter Cr–Cr distance across rutile chains enhances an AFM direct exchange and wins over the FM superexchange; therefore, the net ground state of $CrSbS_3$ is AFM. These two quasi 1D compounds, isostructural while with distinct magnetic ground states, offer us unique opportunities to explore general strategies to systematically tune the magnetic anisotropy in quasi-1D vdW magnets.

4.3.1.2 Alloying Bi into Sb Sites in $CrSbSe_3$ (Series 1).

Polycrystalline powders of $CrSb_{1-x}Bi_xSe_3$ (x = 0.1, 0.2, 0.3, 0.4, 0.5) were easily obtained from solid-state reaction of every element in the desired ratio (see **4.5.1** for synthesis details). The single-phase nature of the synthesized phases was first confirmed by comparing the laboratory powder X-ray diffraction (PXRD) patterns of various compositions with the theoretical PXRD pattern calculated from the $CrSbSe_3$ single crystal structure (**Figure 4.2**). The strong agreement between these patterns with the expected systematic peak shifts due to the bigger radius of Bi atom suggests that the synthesized $CrSb_{1-x}Bi_xSe_3$ phases are isostructural up to x = 0.5. To further corroborate this similarity, high-quality single crystals of $CrSb_{0.9}Bi_{0.1}Se_3$ and $CrSb_{0.8}Bi_{0.2}Se_3$ were obtained by annealing the polycrystal powders. The refined crystal structures of these two Bi-alloyed phases are confirmed to be isostructural with the unalloyed $CrSbSe_3$. In addition, the excellent match between their experimental PXRD patterns and the patterns calculated from their refined single-crystal structures further confirmed the purity of these two alloys (**Figure 4.3**). The absence of extra peak splitting or shifting in X-ray photoelectron spectroscopy (XPS) of all **Series 1** phases as x increases also confirm the successful isomorphic substitution of Sb by Bi and the homogeneity of the resulting polycrystalline powders (**Figure 4.4a**). After establishing the phase purity, we then checked the composition of each phase *via* scanning electron microscopy (SEM) built with electron dispersive spectroscopy (EDS) elemental analysis. Due to the small deviation between the actual and the loading compositions (see **4.5.3** for details), we use the loading x value to represent each phase in the following discussions.
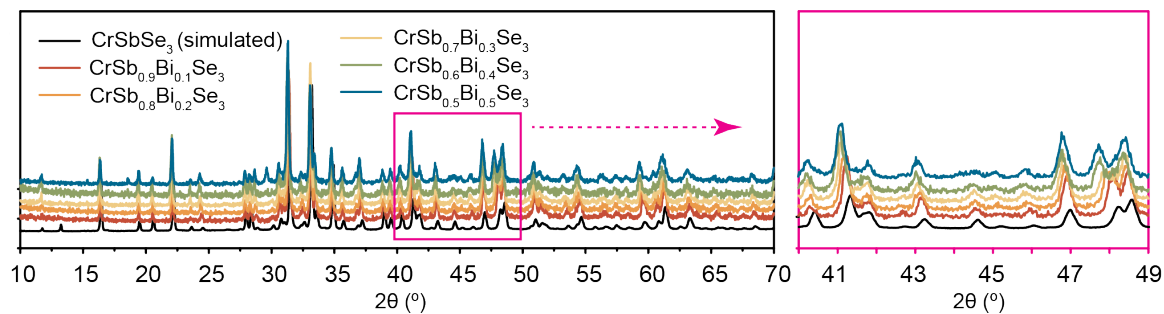
Figure 4.2. PXRD patterns of $CrSb_{1-x}Bi_xSe_3$ (x = 0, 0.1, 0.2, 0.3, 0.4, 0.5) (**Series 1**) phases (left) and a zoom-in view of the systematic PXRD peak shifts (right).
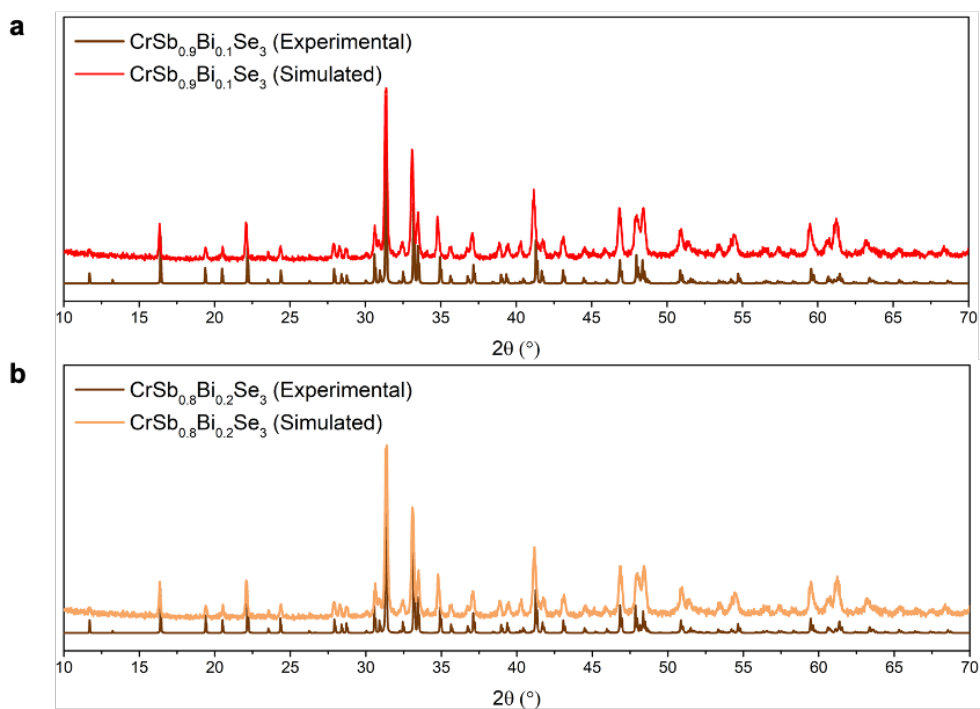

Figure 4.3. a) Experimental PXRD pattern of and the theoretical PXRD patterns calculated from $CrSb_{0.9}Bi_{0.1}Se_3$. b) Experimental PXRD pattern of and the theoretical PXRD patterns calculated from $CrSb_{0.8}Bi_{0.2}Se_3$.

100

To probe the structural evolution with increasing Bi content, we performed Pawley refinements on the high-resolution laboratory PXRD patterns of $CrSb_{1-x}Bi_xSe_3$ with $x = 0 - 0.5$ and obtained the single-crystal structures of $CrSb_{1-x}Bi_xSe_3$ with $x = 0 - 0.2$ by single crystal X-ray diffraction (SXRD) (See **4.5.4** for details). The lattice parameters a and c derived from Pawley refinements differ from the values derived from SXRD by less than 0.007 and 0.08 Å, respectively, which are within acceptable refinement error. Despite such differences, both the Pawley and SXRD refinements reveal similar trends of the variations in the unit cell parameters with different x values. As x increases from 0 to 0.5, the b axis expands ~0.8%, and the c axis expands ~0.3%. In contrast, the a axis exhibits a trend of contraction. The anisotropic change of unit cell dimensions is probably caused by the different nearest pnictogen-pnictogen and pnicotogen-chalcogen distances along a, b, and c axis (See **4.5.5** for details). However, the structural changes are not significant despite the large size differences between Sb^{3+} (76 pm) and Bi^{3+} (103 pm), suggesting the lattice flexibility of quasi-1D vdW phases in response to bigger-atom-alloying. Comparison between single-crystal structures of $CrSbSe_3$, $CrSb_{0.9}Bi_{0.1}Se_3$, and $CrSb_{0.8}Bi_{0.2}Se_3$ shows a slight increase of intra-rutile Cr–Cr distances by 0.0053 Å, a slight increase of inter-rutile Cr–Cr distances by 0.0133 Å, and negligible increases of Cr–Se–Cr superexchange angles by less than 0.4° (**Table 4.7**). However, the changes are quite small and unlikely to alter the type or strength of magnetic couplings significantly.

The XPS spectra for Bi $5d$ and Sb $3d$ shell electrons for the compositions with $x = 0.1 - 0.5$ indicate Bi peak at 24.9 eV ($5d_{5/2}$) 28.0 eV ($5d_{3/2}$) and Sb peak at 529.1 eV ($3d_{5/2}$) and 583.4 eV ($3d_{3/2}$) (**Figure 4.4a**), which are consistent with Bi^{3+} in Bi_2Se_3 and Sb^{3+} in Sb_2Se_3, respectively.[13-14] In addition, the XPS spectra for all $CrSb_{1-x}Bi_xSe_3$ samples show the Cr peak at 575.1 eV ($2p_{3/2}$) and 584.2 eV ($2p_{1/2}$), in consistent with Cr in Cr_2Se_3.[15] This implies that Cr maintains its +3 oxidation state in **Series 1** compounds.
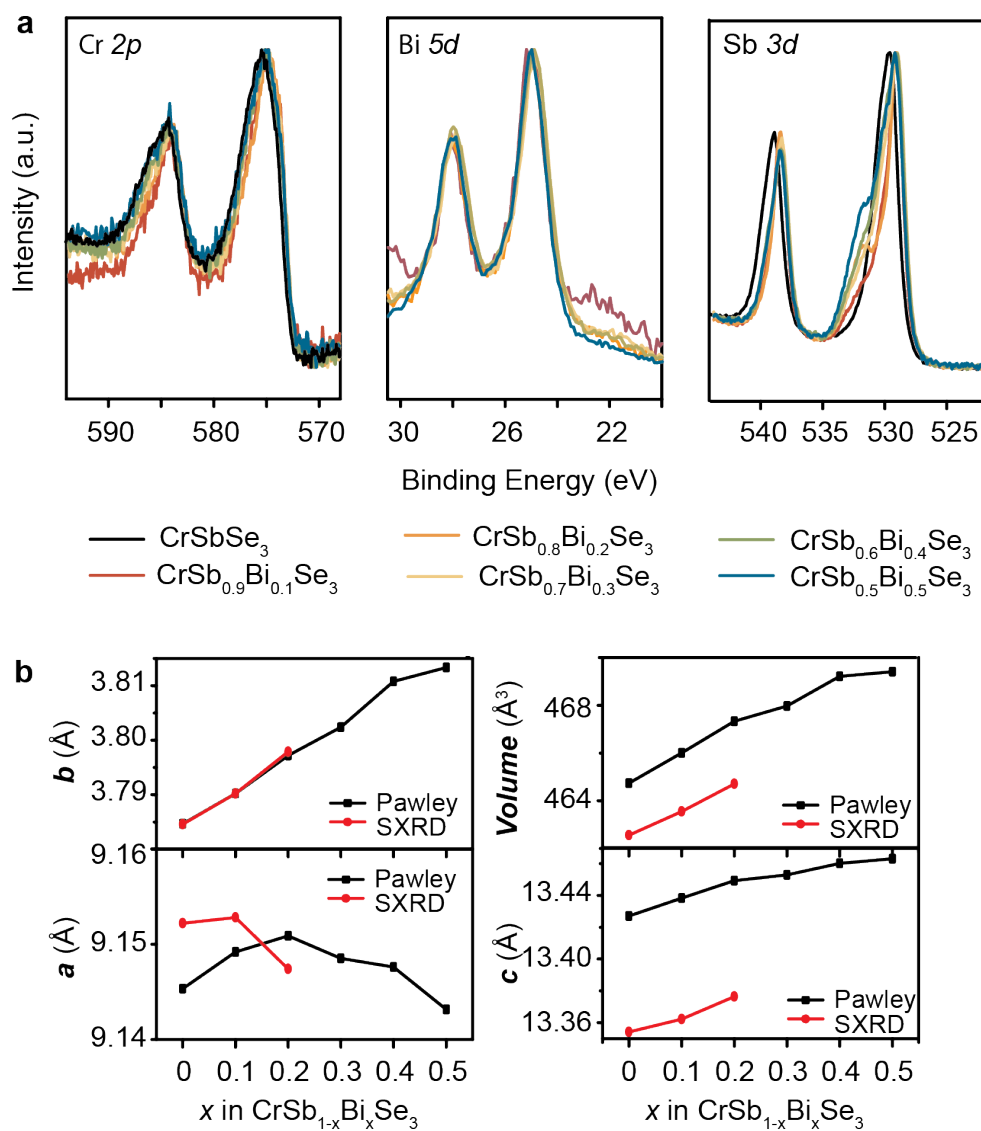
Figure 4.4. Structural evolution of CrSb$_{1-x}$Bi$_x$Se$_3$ (x = 0, 0.1, 0.2, 0.3, 0.4, 0.5) (Series 1). **a)** XPS of Cr *2p*, Bi *5d,* and Sb *3d* shell electrons for **Series 1** phases. **b)** Variation of the lattice parameters as a function of Bi content, obtained through the refinement of single-crystal X-ray diffraction (SXRD) data (red traces) and the Pawley refinement of high-resolution PXRD patterns with LaB$_6$ as internal standard (black traces)

4.3.1.3 Alloying Bi into Sb Sites in CrSbS$_3$ (Series 2).

Polycrystalline powders of CrSb$_{1-x}$Bi$_x$S$_3$ (x = 0, 0.1, 0.2, 0.3, 0.4, 0.5, 0.6) were grown from solid-state reaction of all elements in the desired ratio (see **4.5.1** for synthesis details). Similar to CrSb$_{1-x}$Bi$_x$Se$_3$, the laboratory PXRD patterns of the CrSb$_{1-x}$Bi$_x$S$_3$ exhibit an excellent match with the calculated PXRD pattern of their parent compound CrSbS$_3$, together with systematic peak shifts. According to this, the synthesized CrSb$_{1-x}$Bi$_x$S$_3$ phases are isostructural up to x = 0.6 despite systematic unit cell alterations, further suggesting the structural tolerance to Bi-alloying of these quasi-1D vdW phases. The absence of extra peak splitting or shifting in XPS as x increases also confirms the successful isomorphic substitution of Sb by Bi and the high homogeneity of the resulting polycrystalline powders. Unlike CrSb$_{1-x}$Bi$_x$Se$_3$, no single crystals of the Bi alloyed CrSbS$_3$ have been obtained and the subsequent Rietveld refinements based on the synchrotron PXRD of these **Series 2** compounds reveal the presence of less than 5% of binary impurities Sb$_{2-x}$Bi$_x$S$_3$ (**Table 4.6**). Such an increased synthetic difficulty of CrSb$_{1-x}$Bi$_x$S$_3$ compared to CrSb$_{1-x}$Bi$_x$Se$_3$ is probably due to the larger size difference between Bi^{3+} and S^{2-} and the stronger strain induced by Bi in CrSbS$_3$. The compositions of these **Series 2** compounds were determined by EDS elemental analysis built with SEM imaging tool. Due to the small deviation between the actual and the loading compositions (see **4.5.3** for details), we use the loading x value to represent each phase in the following discussions.

To probe the structural evolution with increasing Bi content, we performed Rietveld refinements on the synchrotron diffraction patterns of CrSb$_{1-x}$Bi$_x$S$_3$ with x = 0 – 0.6 (see **4.5.4** for refinement details). As shown in **Figure 4.5b**, as x increases from 0 to 0.6, the b axis expands ~1.0% and the c axis expands ~0.4% while the a axis contracts ~0.3%. The anisotropic change of unit cell dimensions is probably due to similar reasons as CrSb$_{1-x}$Bi$_x$Se$_3$. Also similar to CrSb$_{1-x}$Bi$_x$Se$_3$, the structural changes are not significant due to the structural versatility of quasi-1D vdW phases. Comparison between the refined structures of CrSb$_{1-x}$Bi$_x$S$_3$ reveals a monotonically elongated intra-rutile chain Cr–Cr distances by 0.03938 Å and fluctuations of inter-rutile chain Cr–Cr distances within 0.02229 Å (**Table 4.8**). Such changes are much smaller than the changes upon chalcogen substitution (decrease ~0.2 Å from CrSbSe$_3$ to CrSbS$_3$) and are unlikely to change the magnetic ordering type significantly.
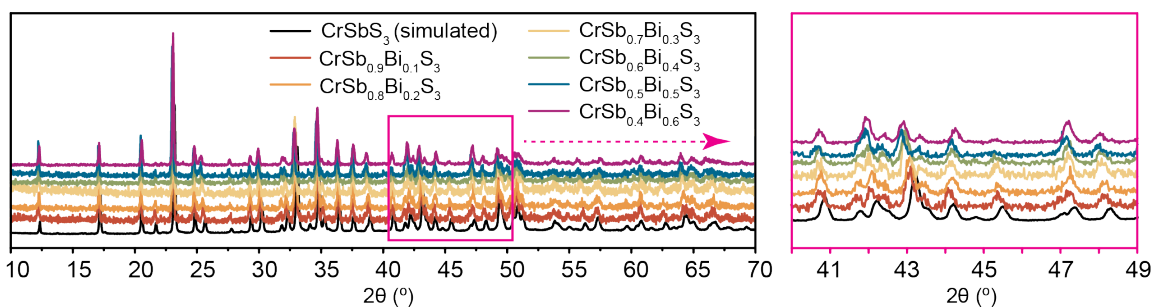
Figure 4.4. PXRD patterns of $CrSb_{1-x}Bi_xS_3$ (x = 0, 0.1, 0.2, 0.3, 0.4, 0.5, 0.6) (**Series 2**) phases (left) and a zoom-in view of the systematic PXRD peak shifts (right).
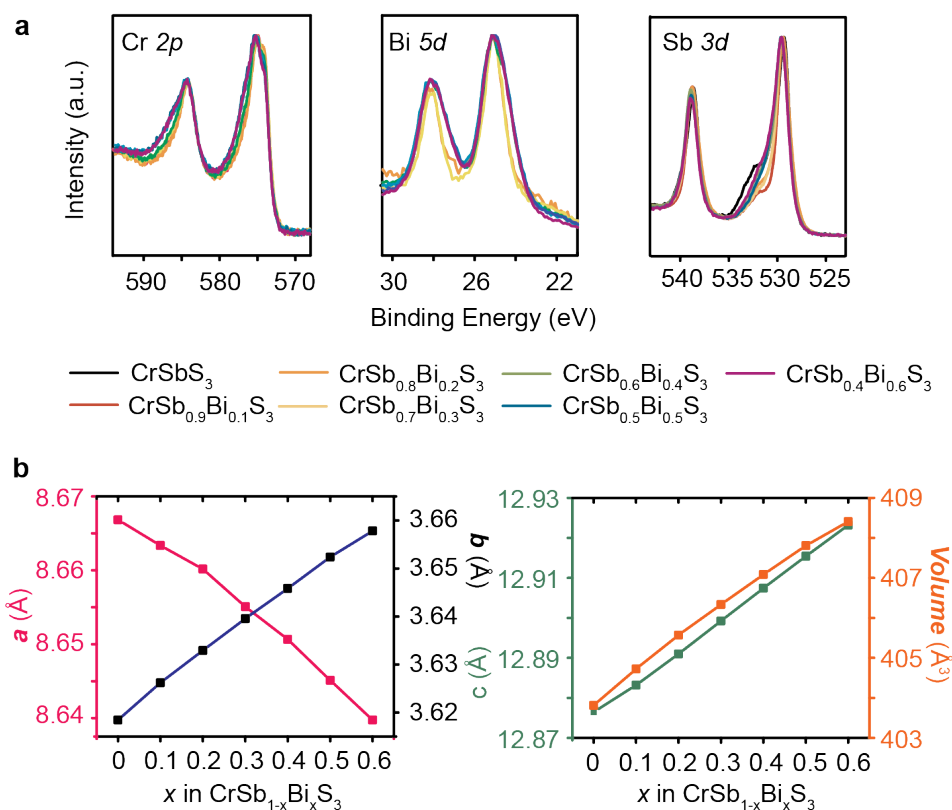

Figure 4.5. Structural evolution of $CrSb_{1-x}Bi_xS_3$ (x = 0, 0.1, 0.2, 0.3, 0.4, 0.5, 0.6) (Series 2). a) XPS of Cr *2p*, Bi *5d* and Sb *3d* shell electrons for **Series 2** phases. **b)** Variation of the lattice parameters as a function of Bi content, obtained through Rietveld refinement of synchrotron diffraction results.

The XPS spectra for Bi $5d$ and Sb $3d$ shell electrons for the compositions with $x = 0.1 -$ 0.6 indicate Bi peak at 25.0 eV ($5d_{5/2}$) 28.1 eV ($5d_{3/2}$) and Sb peak at 529.4 eV ($3d_{5/2}$) and 583.7 eV ($3d_{3/2}$) (**Figure 4.5a**), consistent with Bi^{3+} in Bi_2S_3 and Sb^{3+} in Sb_2S_3, respectively.[16-17] In addition, the XPS spectra for all $CrSb_{1-x}Bi_xS_3$ samples show the Cr peak at 574.7 eV ($2p_{3/2}$) and 584.2 eV ($2p_{1/2}$), in consistent with Cr in Cr_2S_3.[18] This implies that Cr maintains its +3 oxidation state in **Series 2** compounds.

4.3.2 Magnetic Properties

4.3.2.1 Magnetic Properties of CrSb$_{1-x}$Bi$_x$Se$_3$ (Series 1) Alloys

To assess how the substitution of Sb by Bi affects the magnetic behaviors of $CrSb_{1-x}Bi_xSe_3$, field-cooled (FC) and zero-field-cooled (ZFC) temperature-dependent magnetic susceptibility data were collected under 1 kOe applied field in the temperature range from 2 K to 325 K (**Figure 4.6a**). The Curie-Weiss constants θ_{CW}, as well as the effective magnetic moments μ_{eff} of the Bi alloyed samples, were extracted by fitting their $1/\chi$–T curves with the Curie-Weiss law between 120 K and 325 K. No significant variations of either the θ_{CW} or the μ_{eff} on Cr are observed with the increasing Bi contents (**Figure 4.6b**), consistent with the minimally altered structures and electron densities on Cr. The θ_{CW} values for all $CrSb_{1-x}Bi_xSe_3$ phases range from +135 K to +140 K, confirming the dominant ferromagnetic coupling. The μ_{eff} values for all $CrSb_{1-x}Bi_xSe_3$ range from 4.1 μ_B/Cr to 4.2 μ_B/Cr, in agreement with the spin-only value for Cr^{3+} (3.9 μ_B), This not only confirms the +3 oxidation state of Cr but also reveals the weak orbital moments and therefore weak single-ion anisotropy of Cr^{3+} in all the $CrSb_{1-x}Bi_xSe_3$ phases. A paramagnetic (PM) to FM transition is clearly observed for all $CrSb_{1-x}Bi_xSe_3$ phases at ~ 75 K. With increasing Bi content, an increasing discrepancy between FC and ZFC curves was observed at low temperatures (**Figure 4.6a**), which suggests the increased irreversibility of the magnetization process and thus the enhanced magnetic anisotropy. These results collectively indicate the enhanced magnetic anisotropy on top of the same magnetic ordering type in all $CrSb_{1-x}Bi_xSe_3$ phases.

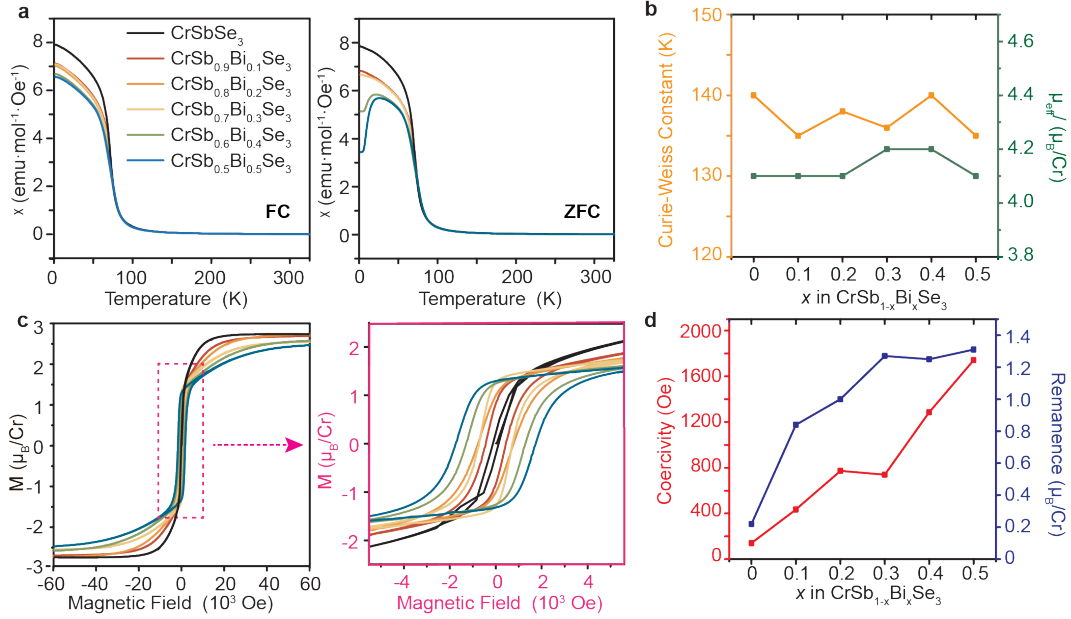**Figure 4.6. Magnetic properties of $CrSb_{1-x}Bi_xSe_3$ (x = 0, 0.1, 0.2, 0.3, 0.4, 0.5) (Series 1). a)** Temperature-dependent magnetic susceptibility curves of **Series 1** phases under FC (left) and ZFC (right) conditions using an external field of 1000 Oe. **b)** Variation of the Curie-Weiss constant and effective moments per Cr as a function of Bi content, obtained by fitting the high-temperature magnetic susceptibility with Curie-Weiss law. **c)** Isothermal field-dependent magnetization of **Series 1** phases at 2 K (left) with the zoom-in view of the hysteresis loops (right). **d)** Variation of coercivity and remanence as a function of Bi content, according to **c)**.

The FM ground state and enhanced magnetic anisotropy of $CrSb_{1-x}Bi_xSe_3$ samples were further confirmed by isothermal magnetization measurements at 2 K. The M-H curves for all samples display a characteristic S-shape hysteresis loop and are nearly saturated to 2.8 μ_B/Cr at 80 kOe, indicating an FM coupling between the Cr^{3+} centers (**Figure 4.6c**). However, a significant increase of coercivity and remanent field was observed as Bi content increases (**Figure 4.6d**). For example, $CrSb_{0.5}Bi_{0.5}Se_3$ shows a nearly 10-fold increase of coercivity and remanence compared to $CrSbSe_3$, suggesting a greatly enhanced magnetic anisotropy. Such a significant influence of Bi alloying on the magnetic anisotropy energy of these quasi 1D vdW phases is surprising because the Sb/Bi site does not directly participate in either the Cr–Cr direct exchange or Cr–Se–Cr superexchange coupling. As a result, we attribute the source of the enhanced anisotropy to the enhanced superexchange anisotropy indirectly induced by Bi alloying. The substitution of Sb by

Bi alters the covalency of the pnictogen-selenium bonds, therefore changing the energies of the p orbitals on Se. Such changes in turn influence the charge transfer and thus the superexchange coupling between Cr and Se, and consequently increase the overall superexchange magnetic anisotropy in the alloyed phases. This indirect effect of heavy element alloying on the superexchange anisotropy has been observed in many 2D magnetic systems and has been corroborated by theoretical calculations.[8] However, this effect has rarely been explored in quasi-1D magnetic systems. Our results here suggest Bi alloying is an effective strategy to finely tune the magnetic anisotropy of quasi 1D vdW magnet $CrSbSe_3$ while minimally changing the structures, oxidation states, and magnetic ordering types.

4.3.2.2 Magnetic Properties of $CrSb_{1-x}Bi_xS_3$ (Series 2) Alloys.

The parent compound of this series, $CrSbS_3$, has been determined to possess uncanted AFM ground state at zero field with field-induced FM correlations and spin-flop transitions (see details in Chapter 3). To probe the effect of isostructural Bi substitution on such magnetic behavior, we first examined the temperature dependence of magnetic susceptibility of $CrSb_{1-x}Bi_xS_3$ phases under 1 kOe (**Figure 4.7a**). As temperature decreases, all these phases show typical Curie-Weiss behavior until ~ 120 K with similar μ_{eff} values of 3.7 μ_B/Cr, in agreement with the spin-only value expected for Cr^{3+} (3.9 μ_B) (**Figure 4.7b**). This agreement, together with the slight variation of μ_{eff} with different Bi contents, suggests the unaltered +3 oxidation state of Cr upon Bi substitution and the weak single-ion anisotropy from Cr^{3+}. However, the θ_{CW} increases from 57 K in $CrSbS_3$ to 80 K in $CrSb_{0.4}Bi_{0.6}S_3$ (**Figure 4.7b**), suggesting a stronger FM correlation in the Bi-alloyed phases. This change is probably due to the slightly weakened AFM direct exchange by the increased inter-rutile-chain distances upon Bi-alloying. A drastic rise in χ happens at around 120 K because of the field-induced FM correlations. With increasing x, this abrupt increase becomes sharper and greater, suggesting a more parallel alignment within the local FM correlations and a lower level of magnetic disorder, which means a stronger anisotropy of the induced FM moments. As temperature further decreases, χ decays drastically in both FC and ZFC curves, indicative of a long-range AFM ordering. The AFM ordering temperature decreases monotonically from 85 K in $CrSbS_3$ to 70 K in $CrSb_{0.4}Bi_{0.6}S_3$, indicative of a weaker AFM ordering in Bi-alloyed phases and consistent with their more positive θ_{CW}. After the drastic decay, χ reaches a plateau. The greater decay and smaller low-temperature value of χ upon Bi-alloying indicate a less disordered

antiparallel alignment spins in the AFM ground state, further suggesting stronger magnetic anisotropy.

The magnetic behaviors of the **Series 2** phases were further checked by isothermal magnetization measurement at 2 K. All phases show wasp-waist hysteresis loops without saturation up to 8 T (**Figure 4.7c**), suggesting the coexistence of strong AFM coupling and the field-induced canted spins (FM correlations).[19] However, phases with higher Bi contents exhibit a greater divergence between the field-increasing and field-decreasing branches and a great area enclosed by the hysteresis loop, indicative of higher irreversibility of the metamagnetic transition and thus stronger magnetic anisotropy.[20] In addition, the increase of magnetization values at 8 T with increasing Bi contents also confirms the more parallel spin alignments in the FM correlations
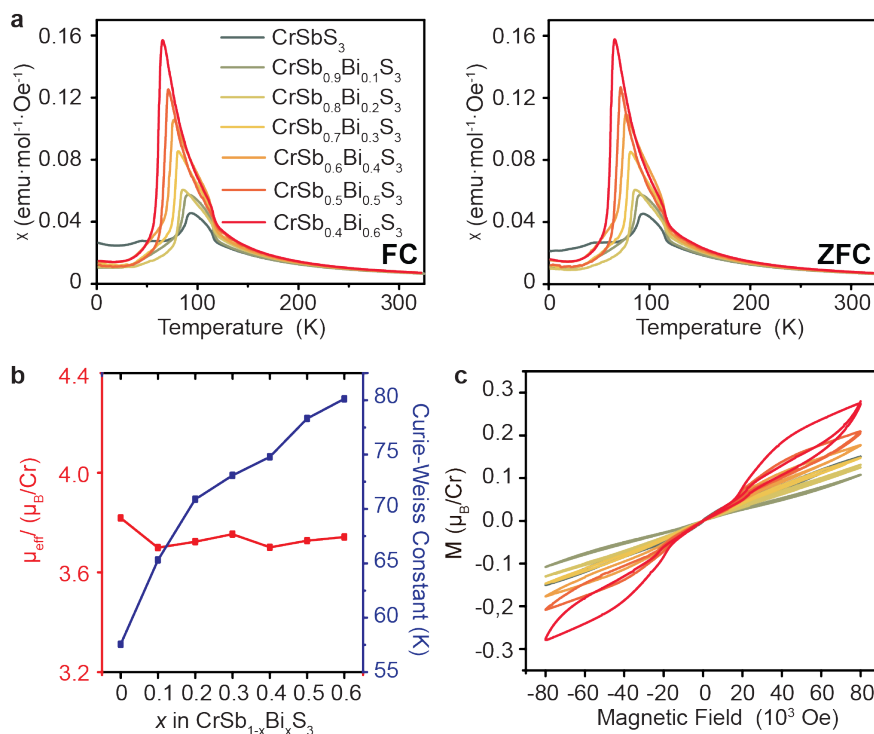
Figure 4.7. Magnetic properties of $CrSb_{1-x}Bi_xS_3$ (x = 0, 0.1, 0.2, 0.3, 0.4, 0.5, 0.6) (Series 2). a) Temperature-dependent magnetic susceptibility curves of **Series 2** phases under FC (left) and ZFC (right) conditions using an external field of 1000 Oe. **b)** Variation of the Curie-Weiss constant and effective moments per Cr as a function of Bi content, obtained by fitting the high-temperature magnetic susceptibility with Curie-Weiss law. **c)** Isothermal field-dependent magnetization of **Series 2** phases at 2 K.

induced by external field, revealing a field-induced magnetic transition more similar to spin-flip rather than spin-flop.[20-22]

To confirm our interpretations of the magnetic behaviors of the **Series 2** phases, we then carefully examined the magnetic transitions of the most heavily Bi-alloyed phase, $CrSb_{0.4}Bi_{0.6}S_3$. We first measured the temperature dependence of heat capacity (C_p) for polycrystalline $CrSb_{0.4}Bi_{0.6}S_3$. The temperature at which a λ-like anomaly is observed in the C_p data is $\sim$ 70 K (**Figure 4.8a**), the same as the temperature in χ -T curve at which χ peaks, confirming the long-range nature of this AFM ordering. To better see the field dependence of C_p, we plotted the temperature dependence of dC_p/dT, which clearly shows lower transition temperature at higher fields (**Figure 4.8a**). This suggests the magnetic transition is highly related to the external field and is typical for field-induced metamagnetic transitions.

We then measured isothermal magnetization curves from – 80 kOe to 80 kOe while heating in the vicinity of the ordering temperature 70 K (**Figure 4.8b**). At 2 K, the AFM ordering is dominant and antiparallel spins are pinned by anisotropy, so only wasp-waist hysteresis loops with low magnetizations are observed. As temperature increases to 10 K, an abrupt transition with hysteresis is observed at 70 kOe, characteristic of spin-flip metamagnetism. Therefore, what happens at this transition is that the magnetization of the two sublattices remains antiparallel up to the critical field 70 kOe, at which a sudden rotation of the spins towards the field direction results in FM alignments. The large coercivity of the hysteresis loops around the critical field is convincing evidence of the strong magnetic anisotropy in this lattice.[21] For example, the coercivity of the double hysteresis loops at $\pm$ 70 kOe is 4700 Oe, clearly revealing the irreversibility of the magnetic transition, which is typical of spin-flip process. As temperature further increases to 24 K and 55 K, the spin-flip transition persists with smaller coercivity due to the weakened magnetic anisotropy at higher temperatures. As the temperature moves above the phase transition temperature, the M-H curves resemble those of ferromagnets, consistent with the existence of short-range FM correlations right above the AFM ordering temperature.
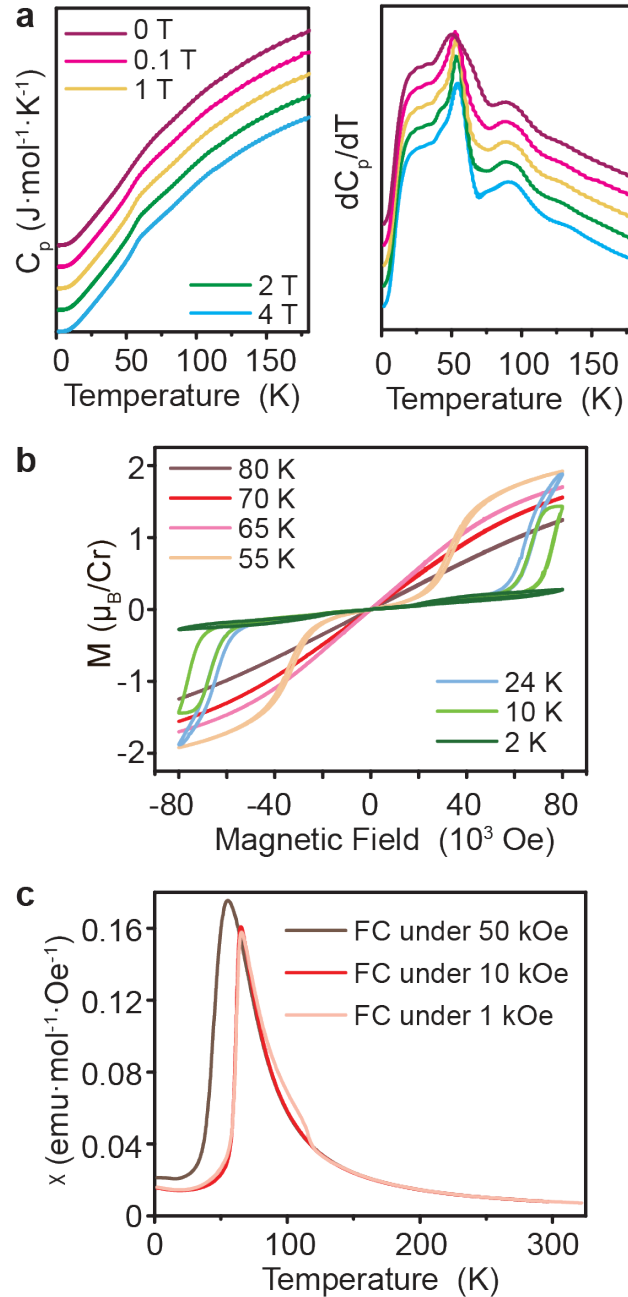
Figure 4.8. Magnetic transition of CrSb$_{0.4}$Bi$_{0.6}$S$_3$. a) Heat capacity (C$_p$) plots (left) and dC$_p$/dT curves (right) of CrSb$_{0.4}$Bi$_{0.6}$S$_3$ under different magnetic fields. **b)** Isothermal field-dependent magnetization of CrSb$_{0.4}$Bi$_{0.6}$S$_3$ at different temperatures. **c)** Temperature-dependent magnetic susceptibility curves of CrSb$_{0.4}$Bi$_{0.6}$S$_3$ under FC conditions using various external fields.

Finally, we checked the FC and ZFC χ-T curves of $CrSb_{0.4}Bi_{0.6}S_3$ under different external fields (**Figure 4.8c**). $CrSb_{0.4}Bi_{0.6}S_3$ has better overlapped ZFC and FC χ-T curves at the low-temperature regime compared to $CrSbS_3$, suggesting the suppression of magnetic disorder by strong anisotropy. Consistent with the dC_p/dT - T curve, the χ-T curves exhibit lower transition temperature at larger external fields. This is also typical for spin-flip transitions. Owning to the strong magnetic anisotropy, there exists a flipping energy barrier. Only at high enough temperature and magnetic fields can the system have enough energy to overcome the barrier and allow the spin-flip to occur. A larger magnetic field provides the energy required for such spin-flip so that less thermal energy (i.e., lower temperature) is required.[23] The C_p-T, M-H, and χ-T curves collectively demonstrate the spin-flip transition in $CrSb_{0.4}Bi_{0.6}S_3$ and the strong magnetic anisotropy therein. These results further support our interpretations of magnetic behaviors of all $CrSb_{1-x}Bi_xS_3$ phases and their stronger magnetic anisotropy with increasing Bi contents.

4.4 Conclusions

The foregoing results demonstrate that Bi alloying is an efficient strategy to systematically tune the magnetic anisotropy in quasi-1D vdW ferromagnet $CrSbSe_3$ and antiferromagnet $CrSbS_3$ while maintaining their structural features and magnetic ordering types. As proof-of-principle, we showed two series of isostructural Bi-alloyed phases $CrSb_{1-x}Bi_xSe_3$ ($x = 0, 0.1, 0.2, 0.3, 0.4, 0.5$) and $CrSb_{1-x}Bi_xS_3$ ($x = 0, 0.1, 0.2, 0.3, 0.4, 0.5, 0.6$) with systematically evolved magnetic behaviors with increasing Bi contents. Most noticeably, Bi alloying significantly enhances the magnetic anisotropy in these phases, no matter the ordering type is ferromagnetic or antiferromagnetic. These results demonstrate the effect of pnictogens on magnetic ordering types and anisotropies of quasi-1D vdW magnets, open a new dimension to tune their magnetism, and further motivate studies to explore the potential of tuning superexchange anisotropy by modifying the indirect bridging sites.

4.5 Methods

4.5.1 Synthesis of $CrSb_{1-x}Bi_xSe_3$ and $CrSb_{1-x}Bi_xS_3$

Polycrystalline powders of $CrSb_{1-x}Bi_xSe_3$ (x = 0, 0.1, 0.2, 0.3, 0.4, 0.5), used for powder X-ray diffraction (PXRD), energy dispersive spectroscopy (EDS), magnetometry, and X-ray photoelectron spectroscopy (XPS) were synthesized by a typical solid-state melt reaction. Starting elements were finely ground, mixed in stoichiometric ratio, and sealed into fused quartz tube under ~50 mTorr. Ampoules were heated to 800 °C over 3 hours and kept at this temperature for 2 days, followed by cooling to room temperature slowly over 66 hours. Single crystals of $CrSb_{0.9}Bi_{0.1}S_3$ and $CrSb_{0.8}Bi_{0.2}S_3$, used in single crystal X-ray diffraction (SXRD) were grown by annealing the polycrystal powders at 800 °C for five days and cooling down the matrix over 60 hours. The preparation and handling of all reagents was done under ambient conditions. Chromium (Sigma-Aldrich, 99.5%), antimony (STREM Chemicals, 99.5%), bismuth (STREM chemicals, 99.5%) and selenium (STREM Chemicals, 99.99%) were purchased and used without further purification.

Polycrystalline powders of $CrSb_{1-x}Bi_xS_3$ (x = 0, 0.1, 0.2, 0.3, 0.4, 0.5, 0.6), used for powder X-ray diffraction (PXRD), energy dispersive spectroscopy (EDS), magnetometry, and X-ray photoelectron spectroscopy (XPS) were synthesized by a typical solid-state melt reaction. Starting elements were finely ground, mixed in stoichiometric ratio, and sealed into fused quartz tube under ~50 mTorr. Ampoules were heated to 550 °C over 3 hours and kept at 550 °C for 6 hours, then heated up to 800 °C, kept at 800 °C for 24 hours followed by cooling to room temperature slowly over 66 hours. The preparation and handling of all reagents was done under ambient conditions. Chromium (Sigma-Aldrich, 99.5%), antimony (STREM Chemicals, 99.5%), bismuth (STREM chemicals, 99.5%) and sulfur (Sigma-Aldrich, 99.98%) were purchased and used without further purification.

4.5.2 Characterization Methods

Single crystal X-ray diffraction (SXRD) data of $CrSb_{0.9}Bi_{0.1}Se_3$ and $CrSb_{0.8}Bi_{0.2}Se_3$ were collected on sizeable micron-sized crystals using a Bruker D8 diffractometer which is coupled to a Bruker APEX-II CCD detector and a Mo Kα radiation (λ = 0.71073 Å), performing ϕ- and ω-

scans. **The refinement of the structure** was performed using direct methods in the SHELX package and refined against F^2 on all data by full-matrix least squares with SHELXL-13.[24]

Laboratory room temperature PXRD data were recorded using a Bruker Advance II diffractometer equipped with a $\theta/2\theta$ reflection geometry and Ni-filtered Cu Kα radiation (Kα1 = 1.5406 Å, Kα2 = 1.5444 Å, Kα2/ Kα1 = 0.5). The tube voltage and current were 40 kV and 40 mA, respectively. Samples for PXRD were prepared by placing a thin layer of the finely grounded material on a zero-background silicon crystal plate. **Pawley refinements** were performed on high resolution (1deg/min) PXRD data of polycrystalline powders of $CrSb_{1-x}Bi_xSe_3$ (x = 0, 0.1, 0.2, 0.3, 0.4, 0.5) mixed together with LaB_6 powder, which is used as an internal standard.

High-resolution synchrotron PXRD data of $CrSb_{1-x}Bi_xS_3$ (x = 0, 0.1, 0.2, 0.3, 0.4, 0.5, 0.6) were collected at 295 K in beamline 11-BM at the Advanced Photon Source (APS), Argonne National Laboratory using the Debye-Scherrer geometry and an average wavelength of 0.457840 Å. Discrete detectors covering an angular range from -6 to 28° 2θ are scanned over a 34° 2θ range, with data points collected every 0.001° 2θ (actual 2θ/step is 0.0009984375°) and scan speed of 0.1 s/step. The 11-BM instrument uses X-ray optics with two platinum-striped mirrors and a double-crystal Si(111) monochromator, where the second crystal has an adjustable sagittal bend.[25] Ion chambers monitor incident flux. A vertical Huber 480 goniometer, equipped with a Heidenhain encoder, positions an analyzer system comprised of twelve perfect Si(111) analyzers and twelve Oxford-Danfysik $LaCl_3$ scintillators, with a spacing of 2° 2θ.[26] Analyzer orientation can be adjusted individually on two axes. A three-axis translation stage holds the sample mounting and allows it to be spun, typically at ~5400 RPM (90 Hz). A Mitsubishi robotic arm is used to mount and dismount samples on the diffractometer.[27] Oxford Cryosystems Cryostream Plus device allows sample temperatures to be controlled over the range 80-500 K when the robot is used. The diffractometer is controlled via EPICS.[27] Data are collected while continually scanning the diffractometer 2θ arm. A mixture of NIST standard reference materials, Si (SRM 640c) and Al_2O_3 (SRM 676) is used to calibrate the instrument, where the Si lattice constant determines the wavelength for each detector. Corrections are applied for detector sensitivity, 2θ offset, small differences in wavelength between detectors, and the source intensity, as noted by the ion chamber before merging the data into a single set of intensities evenly spaced in 2θ. **Rietveld refinements** were performed using the resulting synchrotron diffraction data.

Magnetometry and heat capacity measurements were performed on powders using a Quantum Design Physical Property Measurement System (PPMS) Dynacool, equipped with a vibrating sample magnetometer (VSM) and a heat capacity option. **The X-ray photoelectron spectra (XPS)** were collected using a Thermo Nexsa X-ray photoelectron spectrometer with a monochromated Al X-ray source. **Electron dispersive spectroscopy (EDS)** data of all Bi alloyed samples were collected using a Zeiss Field Emission SEM Ultra55 with EDS detector.

4.5.3 Sample Compositions Determination

The samples compositions were determined by quantification using EDS. The as-synthesized poly-crystals were loaded on carbon tapes and checked under SEM. Ten micro-crystals of each sample were selected randomly on which EDS data were collected. The EDS spectra were fitted and the area under each element's peaks is calculated, which is used for elemental quantifications.

Table 4.1. Loading and the actual compositions of $CrSb_{1-x}Bi_xSe_3$ determined by EDS

Loading elemental ratios				Actual elemental composition
Cr	Sb	Bi	S	*From EDS*
1	0.9	0.1	3	$CrSb_{0.81}Bi_{0.08}S_{2.87}$
1	0.8	0.2	3	$CrSb_{0.68}Bi_{0.15}S_{2.63}$
1	0.7	0.3	3	$CrSb_{0.59}Bi_{0.22}S_{2.61}$
1	0.6	0.4	3	$CrSb_{0.50}Bi_{0.28}S_{2.55}$
1	0.5	0.5	3	$CrSb_{0.41}Bi_{0.40}S_{2.27}$
1	0.4	0.6	3	$CrSb_{0.34}Bi_{0.40}S_{2.47}$

Table 4.2. Loading and the actual compositions of $CrSb_{1-x}Bi_xS_3$ determined by EDS

Loading elemental ratios				Final elemental composition
Cr	Sb	Bi	Se	*From EDS*
1	0.9	0.1	3	$CrSb_{0.96}Bi_{0.11}Se_{3.35}$
1	0.8	0.2	3	$CrSb_{0.82}Bi_{0.21}Se_{3.35}$
1	0.7	0.3	3	$CrSb_{0.78}Bi_{0.29}Se_{3.21}$
1	0.6	0.4	3	$CrSb_{0.59}Bi_{0.35}Se_{2.82}$
1	0.5	0.5	3	$CrSb_{0.52}Bi_{0.52}Se_{3.32}$

4.5.4 Refinement Details

4.5.4.1 Refinement Details of Single-Crystal Structures of $CrSb_{0.9}Bi_{0.1}S_3$ and $CrSb_{0.8}Bi_{0.2}S_3$

Table 4.3. Details of the structure determination of $CrSb_{0.9}Bi_{0.1}S_3$ based on single-crystal experiments measured at 300 K

Sum Formula	$CrSb_{0.9}Bi_{0.1}S_3$
Radiation	λ (Mo-$K\alpha$ = 0.71073 Å)
Index ranges	$-15 \leq h \leq 15, -5 \leq k \leq 6, -22 \leq l \leq 22$
Absorption coefficient /mm^{-1}	34.730
Measured reflections	20541
Independent reflections	1266
No. of parameters	37
Goodness-of-fit on F^2	1.181
Final R indices [$I > 2\sigma (I)$]	0.0411
$R(int)$	0.0533
$R(\sigma)$	0.0197
R indices (all data)	0.0418
ωR_2 (all data)	0.0960
Largest diff. peak and hole (e$^-$/ Å^3)	2.112 to -6.029

Table 4.4. Details of the structure determination of $CrSb_{0.8}Bi_{0.2}S_3$ based on single-crystal experiments measured at 300 K

Sum Formula	$CrSb_{0.9}Bi_{0.1}S_3$
Radiation	λ (Mo-$K\alpha$ = 0.71073 Å)
Index ranges	$-16 \leq h \leq 16, -6 \leq k \leq 6, -22 \leq l \leq 22$
Absorption coefficient /mm^{-1}	37.844
Measured reflections	18220
Independent reflections	1264
No. of parameters	37
Goodness-of-fit on F^2	1.224
Final R indices [$I > 2\sigma (I)$]	0.0334
$R(int)$	0.0478
$R(\sigma)$	0.0206
R indices (all data)	0.0338
ωR_2 (all data)	0.0900
Largest diff. peak and hole (e^-/ Å^3)	1.593to -3.072

4.5.4.2 Fitting Results of Pawley Refinement of CrSb$_{1-x}$Bi$_x$Se$_3$
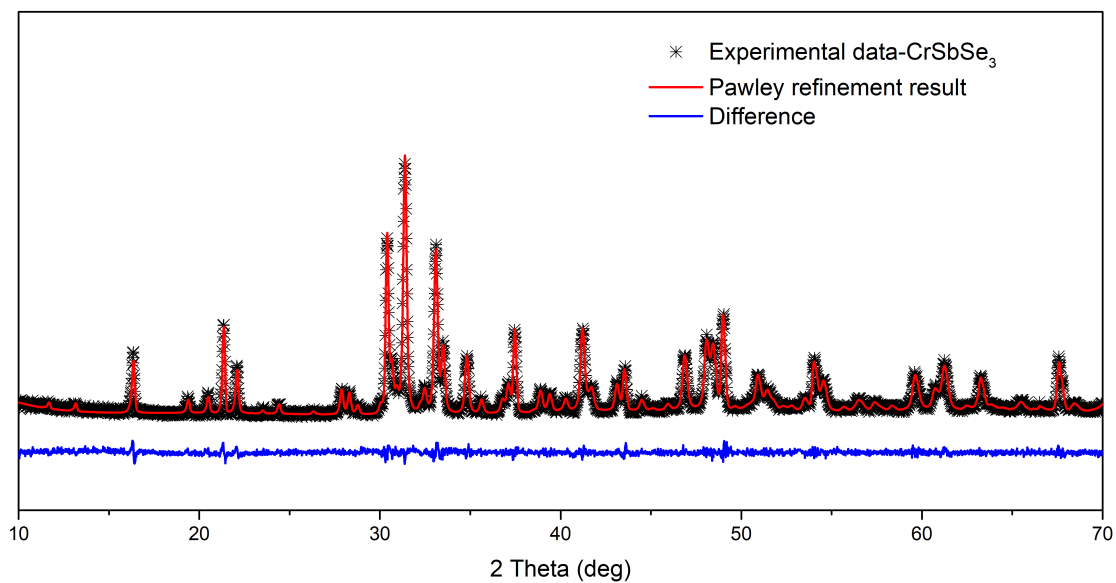
Figure 4.9. Pawley refinement result of CrSbSe$_3$
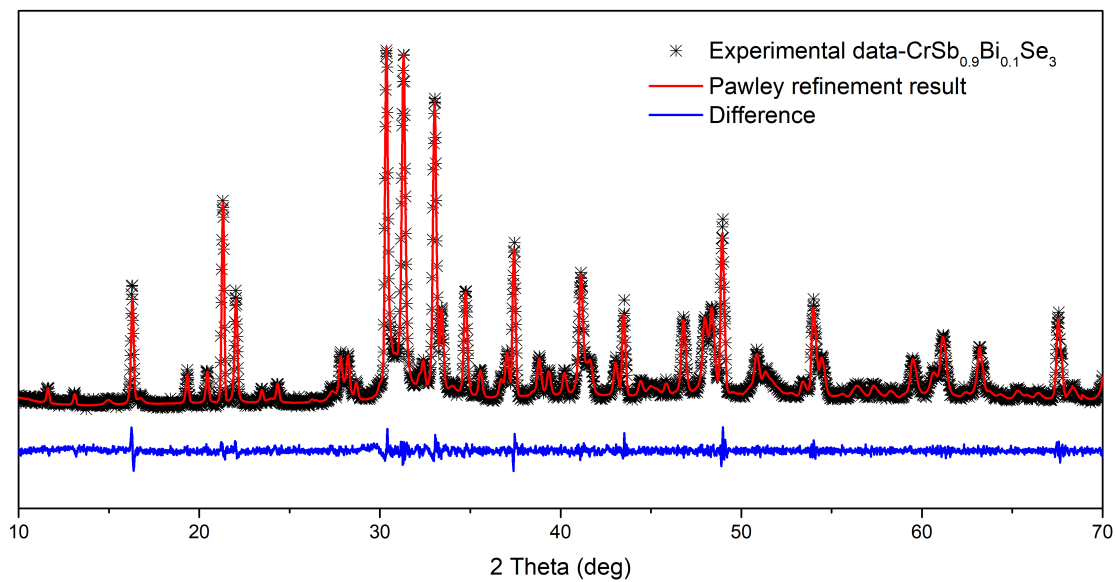
Figure 4.10. Pawley refinement result of CrSb$_{0.9}$Bi$_{0.1}$Se$_3$
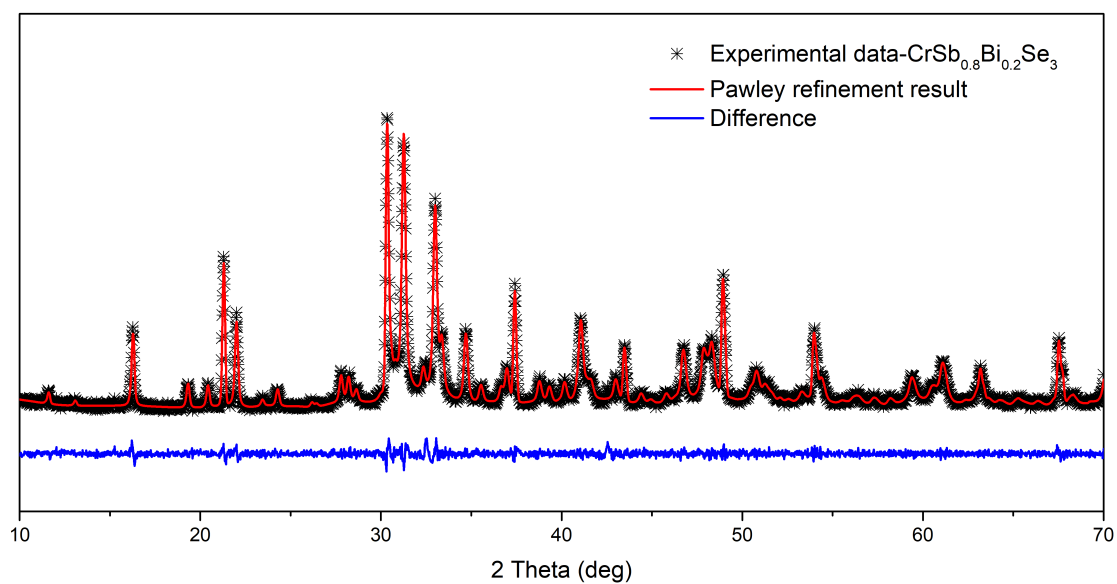
Figure 4.11. Pawley refinement result of $CrSb_{0.8}Bi_{0.2}Se_3$
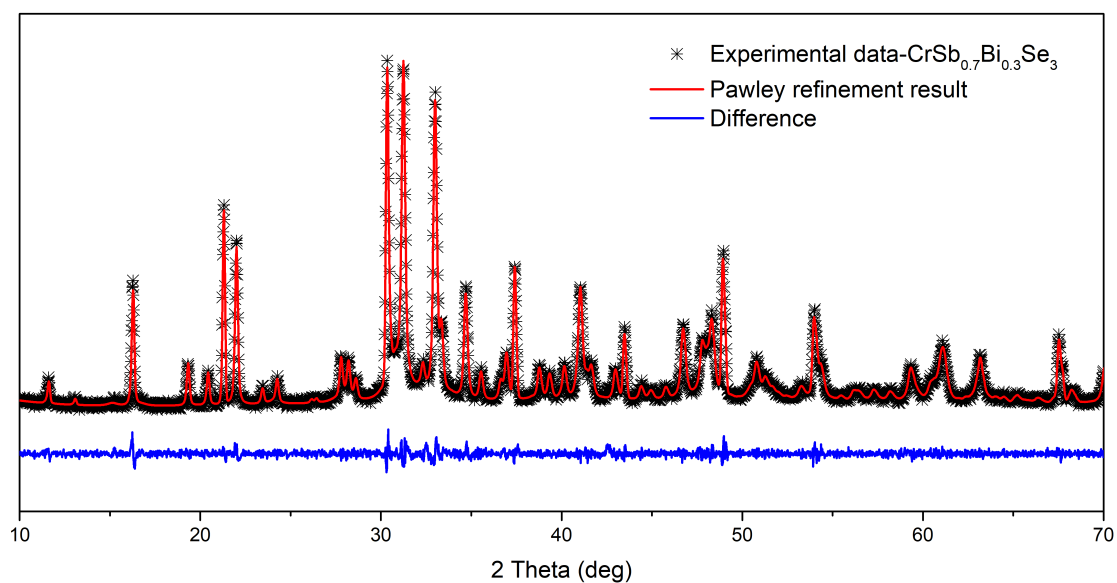
Figure 4.12. Pawley refinement result of $CrSb_{0.7}Bi_{0.3}Se_3$
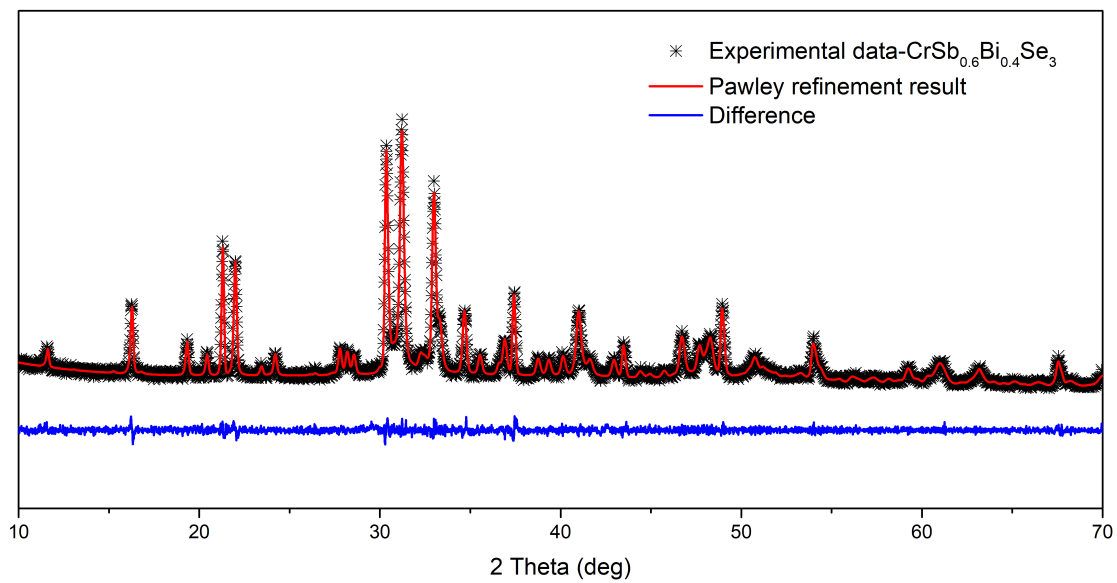
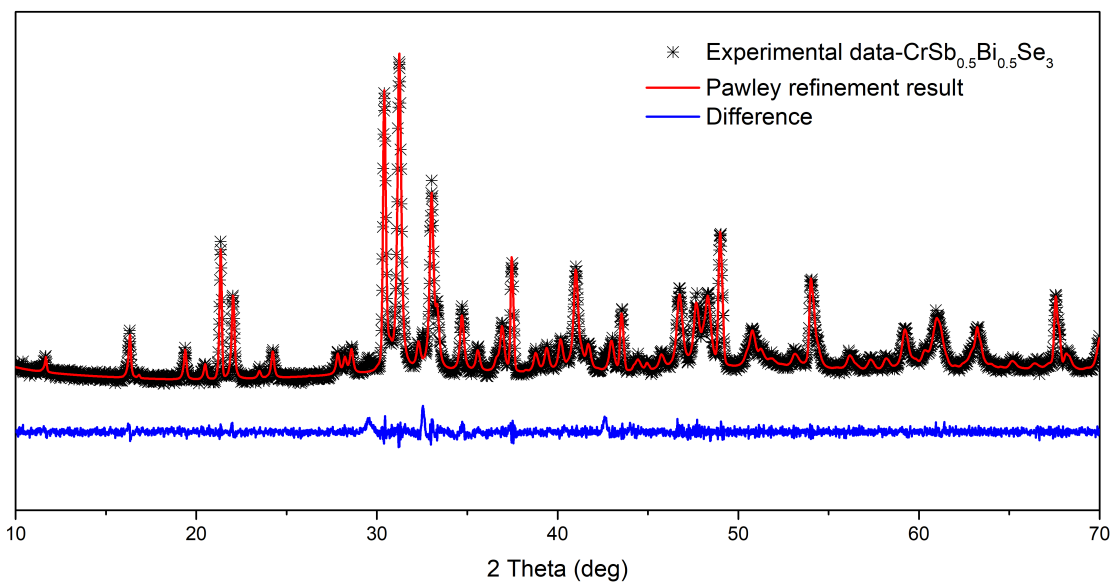**Figure 4.13**. Pawley refinement result of $CrSb_{0.6}Bi_{0.4}Se_3$

Figure 4.14. Pawley refinement result of $CrSb_{0.5}Bi_{0.5}Se_3$

Table 4.5. R_{wp} values of the Pawley refinements for $CrSb_{1-x}Bi_xSe_3$ (x = 0, 0.1, 0.2, 0.3, 0.4, 0.5)

x value in $CrSb_{1-x}Bi_xSe_3$	0	0.1	0.2	0.3	0.4	0.5
Rietveld refinement R_{wp} (%)	6.8	5.6	5.4	5.3	6.9	13.7

4.5.4.3 Fitting Results of Rietveld Refinements of $CrSb_{1-x}Bi_xS_3$
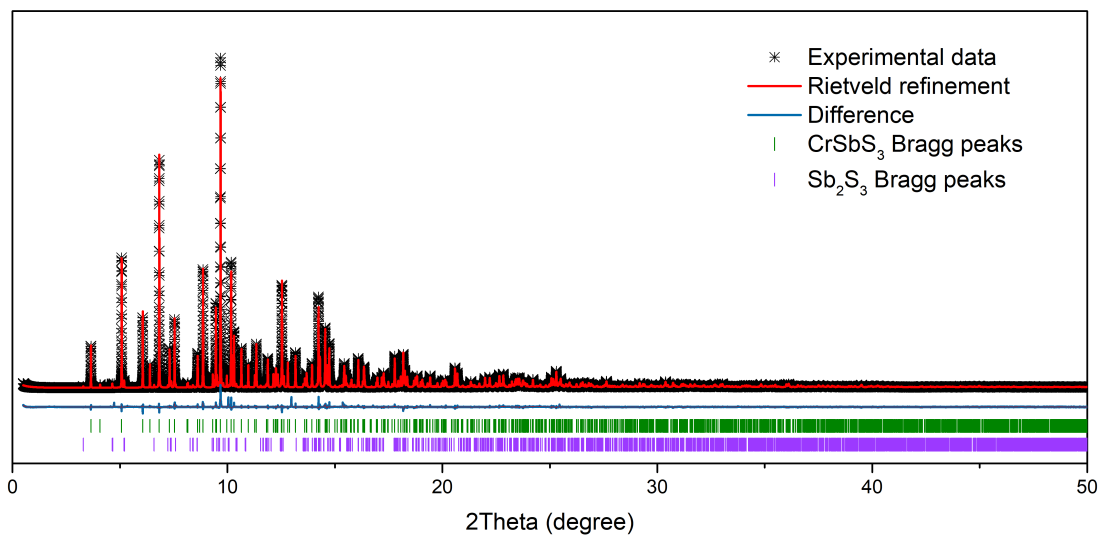
Figure 4.15. Rietveld refinement result of $CrSbS_3$
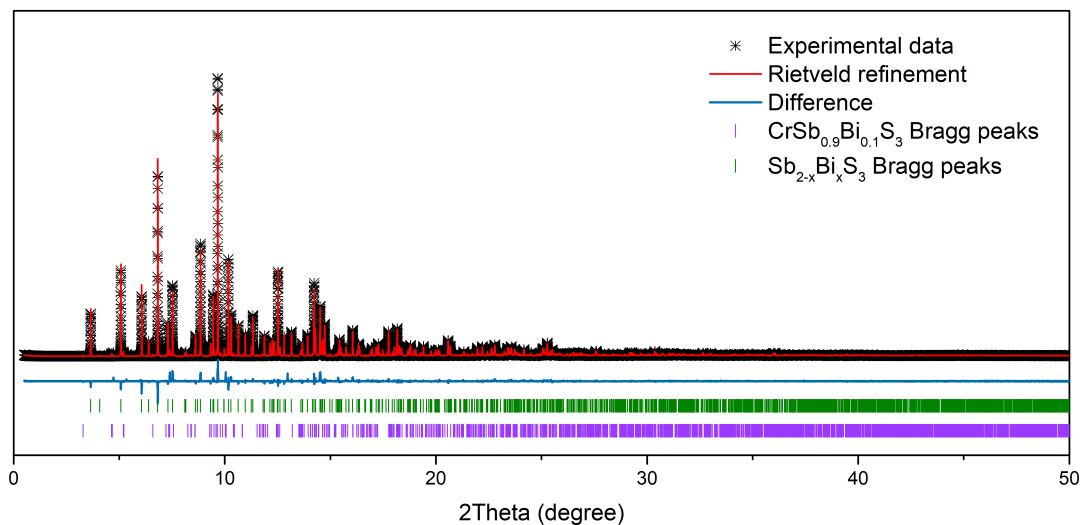
Figure 4.16. Rietveld refinement result of $CrSb_{0.9}Bi_{0.1}S_3$
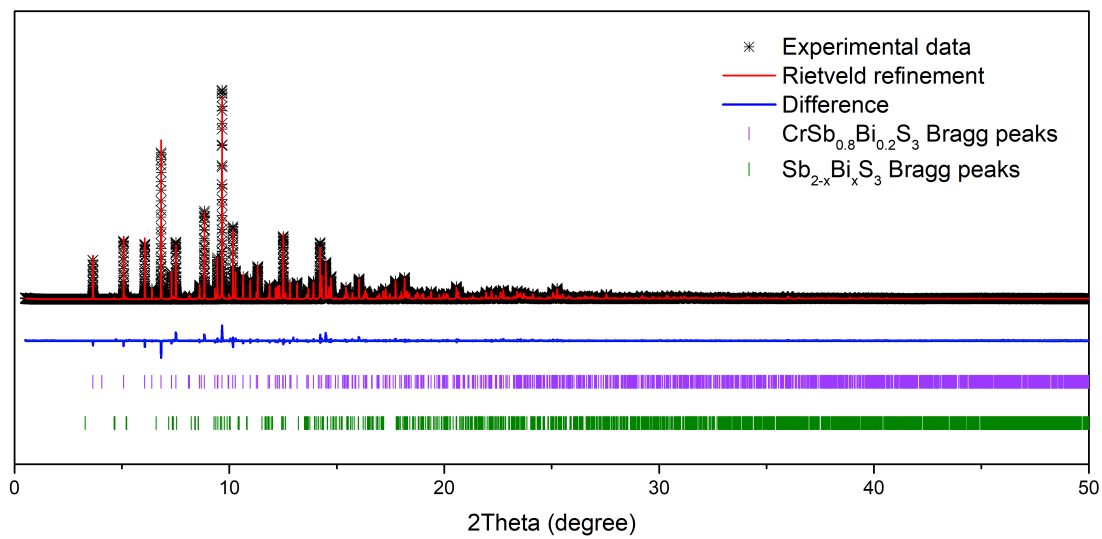
Figure 4.17. Rietveld refinement result of $CrSb_{0.8}Bi_{0.2}S_3$

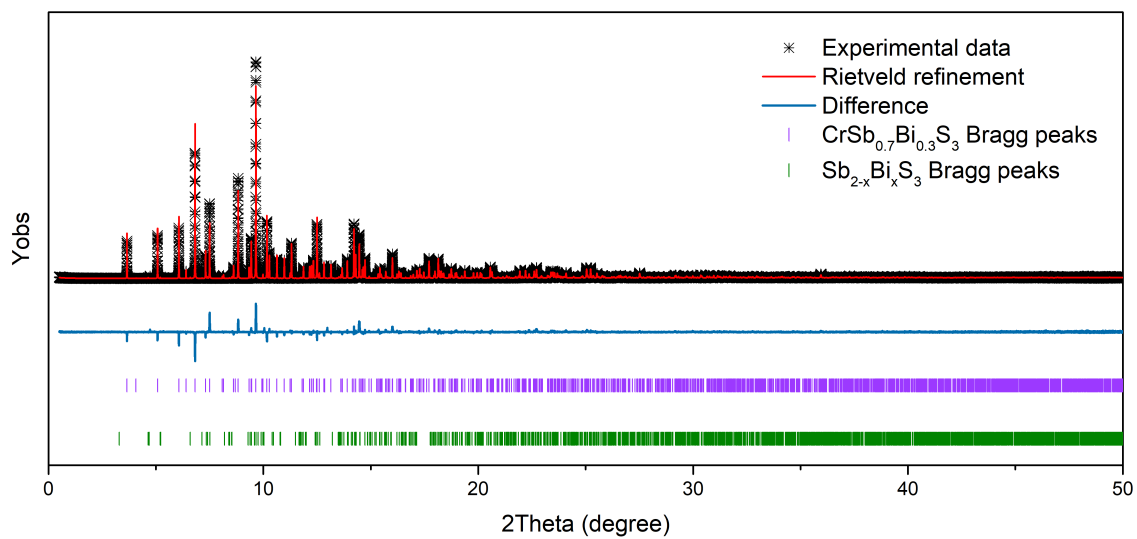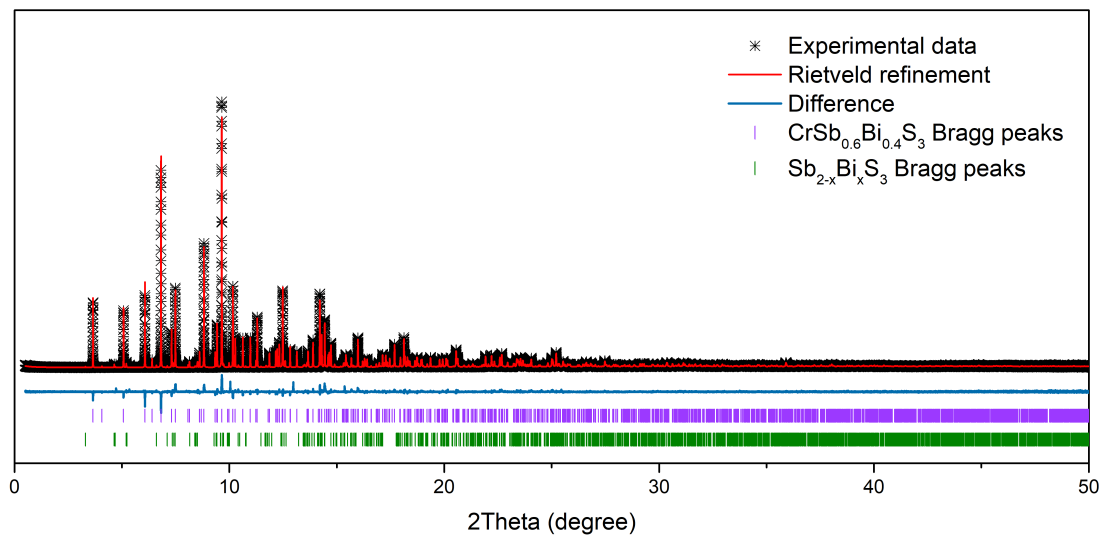**Figure 4.18**. Rietveld refinement result of $CrSb_{0.7}Bi_{0.3}S_3$

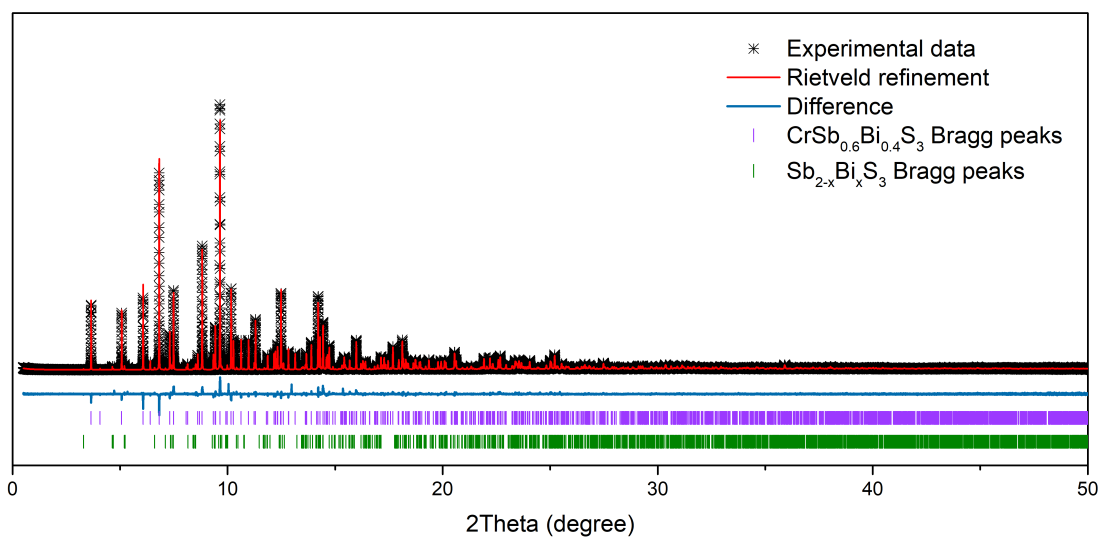**Figure 4.19**. Rietveld refinement result of $CrSb_{0.6}Bi_{0.4}S_3$

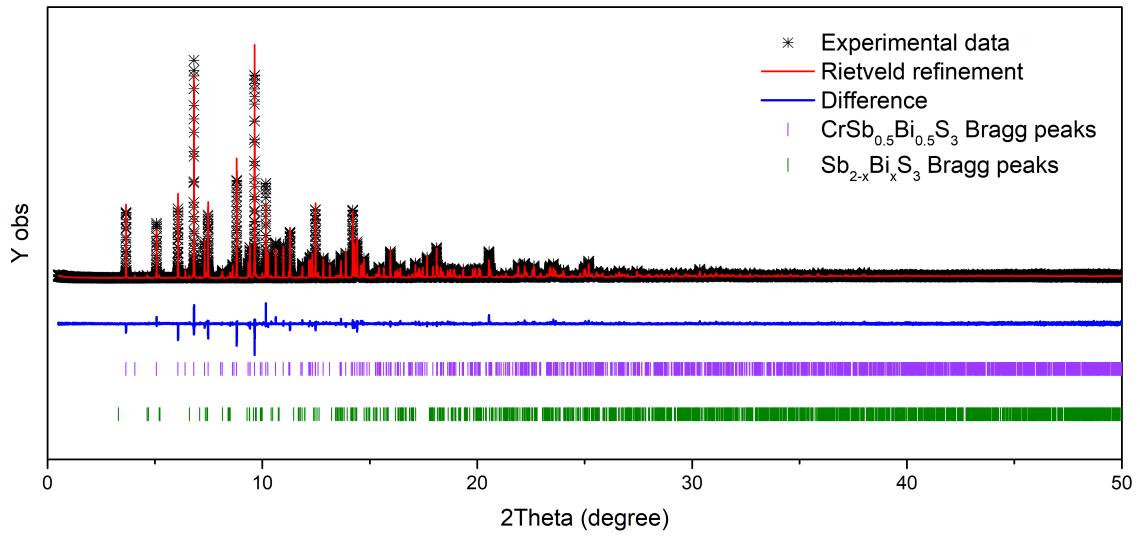**Figure 4.20**. Rietveld refinement result of $CrSb_{0.5}Bi_{0.4}S_3$

Figure 4.21. Rietveld refinement result of $CrSb_{0.5}Bi_{0.5}S_3$

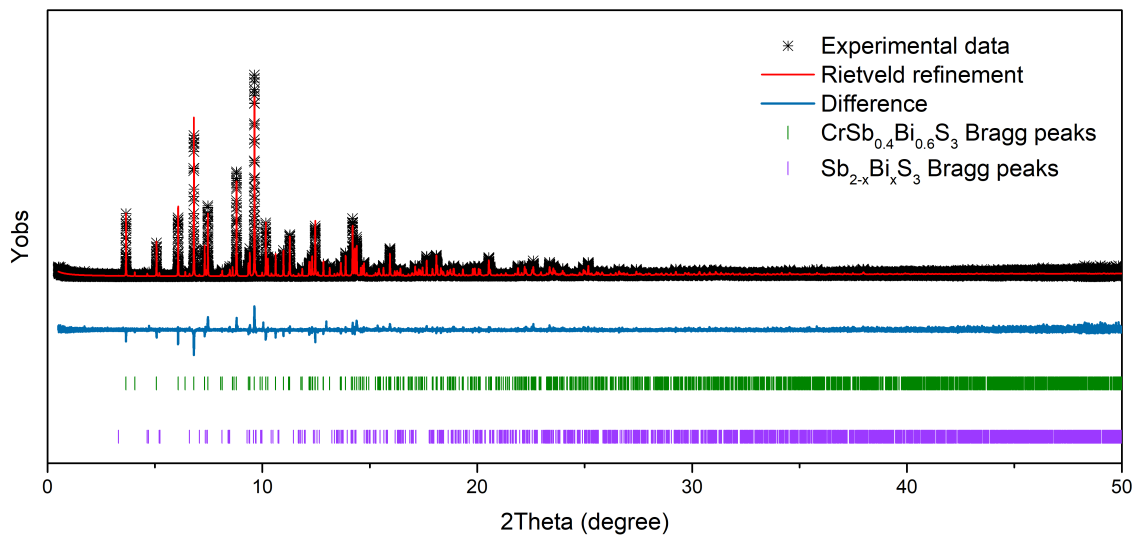**Figure 4.22**. Rietveld refinement result of $CrSb_{0.4}Bi_{0.6}S_3$

Table 4.6. R_{wp} values of the Rietveld refinements for $CrSb_{1-x}Bi_xS_3$ (x = 0, 0.1, 0.2, 0.3, 0.4, 0.5, 0.6) and the weight percentage of impurity

x value	0	0.1	0.2	0.3	0.4	0.5	0.6
Estimated $Sb_{2-y}Bi_yS_3$ weight% (%)	5.2	4.4	3.3	3.2	6.1	6.3	8.9
Rietveld refinement R_{wp} (%)	9.33	13.01	11.88	18.67	13.83	14.34	24.38

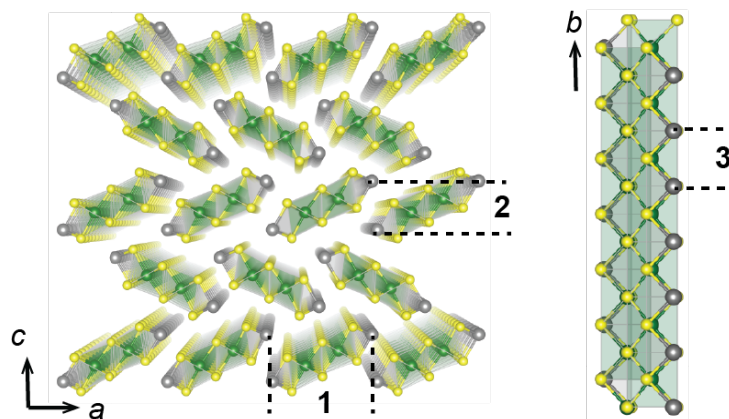## 4.5.5 Analysis of the Anisotropic Changes of Unit Cell Dimensions upon Bi-alloying

Figure 4.23. A schematic view of the nearest pnictogen-pnictogen distances along different crystallographic directions in $CrPnCh_3$ (Pn = Sb, Bi; Ch = S, Se). Green, grey, and yellow spheres represent Cr, Pn, and Ch, respectively.

We attribute the anisotropic change of unit cell dimensions upon Bi-alloying to the different distances between the nearest pnictogens along different crystallographic directions. The

nearest pnictogen-pnictogen distance in $CrSbSe_3$ is 9.1152(3) Å along a axis (distance **1** in **Figure S17**), 4.6662(13) Å along c axis (distance 2 in **Figure S17**), and 3.78460(11) Å along b axis (distance **3** in **Figure S17**). Due to this, the pnictogen-pnictogen repulsion is the strongest along b axis and the weakest along a axis. The same sequence holds true for $CrSbS_3$. As a result, b axis expands the most upon Bi alloying, and a axis does not show obvious expansion upon Bi alloying.

The main source of the a-axis-contraction is the contracted distance between the nearest pnictogen-chalcogen along a axis. Such a decrease is probably because of the stronger interaction between Bi and S/Se compared to Sb and S/Se.

4.5.6 Connection of Cr^{3+} in Each Double-Rutile Chain in $CrSb_{1-x}Bi_xSe_3$ and $CrSb_{1-x}Bi_xS_3$

Note: the distances or angles represented by the numbers in the following two tables are shown in **Figure S16**.

Table 4.7. Connection of Cr^{3+} in each double-rutile chain in $CrSb_{1-x}Bi_xSe_3$

	Cr-Cr distance (Å)	Cr-Cr distance (Å)	Cr-Se-Cr angle (°)		
	1	2	1	2	3
$CrSbSe_3$	3.78460(11)	3.639(3)	97.06(6)	93.84(5)	92.92(5)
$CrSb_{0.9}Bi_{0.1}Se_3$	3.79020(11)	3.6412(10)	97.16(3)	94.03(3)	92.98(19)
$CrSb_{0.8}Bi_{0.2}Se_3$	3.79790(11)	3.6443(11)	97.33(3)	94.29(3)	93.02(3)

Table 4.8. Connection of Cr^{3+} in each double-rutile chain in $CrSb_{1-x}Bi_xS_3$

|	Cr-Cr distance (Å)	Cr-Cr distance (Å)	Cr-Se-Cr angle (°)		
	1	**2**	**1**	**2**	**3**
$CrSbS_3$	3.61845(0)	3.42896(0)	97.9214(0)	94.2488(0)	92.0939(0)
$CrSb_{0.9}Bi_{0.1}S_3$	3.62618(0)	3.43000(0)	97.6084(0)	94.3552(0)	91.7618(0)
$CrSb_{0.8}Bi_{0.2}S_3$	3.63291(0)	3.43060(0)	97.8601(0)	94.3258(0)	91.7171(0)
$CrSb_{0.7}Bi_{0.3}S_3$	3.63955(0)	3.42072(0)	97.7608(0)	94.5261(0)	91.4435(0)
$CrSb_{0.6}Bi_{0.4}S_3$	3.64583(0)	3.43106(0)	98.2503(0)	94.8338(0)	91.8556(0)
$CrSb_{0.5}Bi_{0.5}S_3$	3.65237(0)	3.45125(0)	98.3138(0)	95.6471(0)	92.3419(0)
$CrSb_{0.4}Bi_{0.6}S_3$	3.65783(0)	3.44499(0)	98.3235(0)	95.5285(0)	91.8039(0)
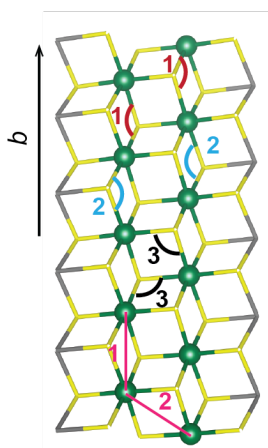
Figure 4.24. A schematic view of the Cr–Cr connectios in $CrPnCh_3$ (Pn = Sb, Bi; Ch = S, Se). Green spheres, grey points, and yellow points represent Cr, Pn, and Ch, respectively.

References

(1) Mermin, N. D.; Wagner, H., Absence of ferromagnetism or antiferromagnetism in one- or two-dimensional isotropic Heisenberg models. *Phys. Rev. Lett.* **1966,** *17* (22), 1133-1136.

(2) Coughlin, A. L.; Xie, D.; Yao, Y.; Zhan, X.; Chen, Q.; Hewa-Walpitage, H.; Zhang, X.; Guo, H.; Zhou, H.; Lou, J.; Wang, J.; Li, Y. S.; Fertig, H. A.; Zhang, S., Near degeneracy of magnetic phases in two-dimensional chromium telluride with enhanced perpendicular magnetic anisotropy. *ACS Nano* **2020,** *14* (11), 15256-15266.

(3) Kim, J.; Kim, K. W.; Kim, B.; Kang, C. J.; Shin, D. B.; Lee, S. H.; Min, B. C.; Park, N., Exploitable magnetic anisotropy of the two-dimensional magnet CrI_3. *Nano. Lett.* **2020,** *20* (2), 929-935.

(4) Park, S. Y.; Kim, D. S.; Liu, Y.; Hwang, J.; Kim, Y.; Kim, W.; Kim, J. Y.; Petrovic, C.; Hwang, C.; Mo, S. K.; Kim, H. J.; Min, B. C.; Koo, H. C.; Chang, J.; Jang, C.; Choi, J. W.; Ryu, H., Controlling the magnetic anisotropy of the van der Waals ferromagnet Fe_3GeTe_2 through hole doping. *Nano. Lett.* **2020,** *20* (1), 95-100.

(5) Qu, Y.; Arguilla, M. Q.; Zhang, Q.; He, X.; Dinca, M., Ultrathin, High-aspect ratio, and free-standing magnetic nanowires by exfoliation of ferromagnetic quasi-one-dimensional van der Waals lattices. *J. Am. Chem. Soc.* **2021,** *143* (46), 19551-19558.

(6) Sun, Y.; Song, Z. F.; Tang, Q.; Luo, X., Origin of anisotropic magnetic properties in the ferromagnetic semiconductor $CrSbSe_3$ with a pseudo-one-dimensional structure. *J. Phys. Chem. C* **2020,** *124* (20), 11110-11116.

(7) Lado, J. L.; Fernandez-Rossier, J., On the origin of magnetic anisotropy in two dimensional CrI_3. *2D Mater.* **2017,** *4* (3), 035002.

(8) Kim, D. H.; Kim, K.; Ko, K. T.; Seo, J.; Kim, J. S.; Jang, T. H.; Kim, Y.; Kim, J. Y.; Cheong, S. W.; Park, J. H., Giant magnetic anisotropy induced by ligand LS coupling in layered Cr compounds. *Phys. Rev. Lett.* **2019,** *122* (20), 207201.

(9) Wu, L. S.; Nikitin, S. E.; Wang, Z.; Zhu, W.; Batista, C. D.; Tsvelik, A. M.; Samarakoon, A. M.; Tennant, D. A.; Brando, M.; Vasylechko, L.; Frontzek, M.; Savici, A. T.; Sala, G.; Ehlers, G.; Christianson, A. D.; Lumsden, M. D.; Podlesnyak, A., Tomonaga-Luttinger liquid behavior and spinon confinement in $YbAlO_3$. *Nat. Commun.* **2019,** *10*, 698.

(10) Chang, J.; Zhao, J. Z.; Ding, Y., Anisotropic superexchange through nonmagnetic anions with spin-orbit coupling. *Eur. Phys. J. B* **2020,** *93* (8), 159.

(11) Winter, S. M.; Hill, S.; Oakley, R. T., Magnetic ordering and anisotropy in heavy atom radicals. *J. Am. Chem. Soc.* **2015,** *137* (11), 3720-3730.

(12) Kong, T.; Stolze, K.; Ni, D. R.; Kushwaha, S. K.; Cava, R. J., Anisotropic magnetic properties of the ferromagnetic semiconductor $CrSbSe_3$. *Phys. Rev. Mater.* **2018,** *2* (1), 014410.

(13) Walsh, L. A.; Smyth, C. M.; Barton, A. T.; Wang, Q. X.; Che, Z. F.; Yue, R. Y.; Kim, J.; Kim, M. J.; Wallace, R. M.; Hinkle, C. L., Interface chemistry of contact metals and ferromagnets on the topological insulator Bi_2Se_3. *J. Phys. Chem. C* **2017,** *121* (42), 23551-23563.

(14) Liu, X. S.; Chen, J.; Luo, M.; Leng, M. Y.; Xia, Z.; Zhou, Y.; Qin, S. K.; Xue, D. J.; Lv, L.; Huang, H.; Niu, D. M.; Tang, J., Thermal evaporation and characterization of Sb_2Se_3 thin film for substrate Sb_2Se_3/CdS Solar Cells. ACS *Appl. Mater. Interfaces* **2014,** *6* (13), 10687-10695.

(15) Ramaraj, S.; Mani, S.; Chen, S. M.; Palanisamy, S.; Velusamy, V.; Hall, J. M.; Chen, T. W.; Tseng, T. W., Hydrothermal synthesis of Cr_2Se_3 hexagons for sensitive and low-level detection of 4-nitrophenol in Water. *Sci. Rep.* **2018,** *8,* 4839.

(16) Grigas, J.; Talik, E.; Lazauskas, V., X-ray photoelectron spectra and electronic structure of Bi_2S_3 crystals. *Phys. Status Solidi B* **2002,** *232* (2), 220-230.

(17) Zakaznova-Herzog, V. P.; Harmer, S. L.; Nesbitt, H. W.; Bancroft, G. M.; Flemming, R.; Pratt, A. R., High resolution XPS study of the large-band-gap semiconductor stibnite (Sb_2S_3): Structural contributions and surface reconstruction. *Surf. Sci.* **2006,** *600* (2), 348-356.

(18) Zhou, S. S.; Wang, R. Y.; Han, J. B.; Wang, D. L.; Li, H. Q.; Gan, L.; Zhai, T. Y., Ultrathin non-van der Waals magnetic rhombohedral Cr_2S_3: Space-confined chemical vapor deposition synthesis and raman scattering investigation. *Adv. Funct. Mater.* **2019,** *29* (3), 1805880.

(19) Bennett, L. H.; Della Torre, E., Analysis of wasp-waist hysteresis loops. *J. Appl. Phys.* **2005,** *97* (10), 10E502.

(20) Leclercq, B.; Kabbour, H.; Damay, F.; Colin, C. V.; Pautrat, A.; Arevalo-Lopez, A. M.; Mentre, O., Metamagnetic transitions versus magnetocrystalline anisotropy in two cobalt arsenates with 1D Co^{2+} Chains. *Inorg. Chem.* **2019,** *58* (19), 12609-12617.

(21) Baranov, N. V.; Selezneva, N. V.; Sherokalova, E. M.; Baglaeva, Y. A.; Ovchinnikov, A. S.; Tereshchenko, A. A.; Gorbunov, D. I.; Volegov, A. S.; Sherstobitov, A. A., Magnetic phase transitions, metastable states, and magnetic hysteresis in the antiferromagnetic compounds $Fe_{0.5}TiS_{2-y}Se_y$. *Phys. Rev. B* **2019,** *100* (2), 024430.

(22) Yamada, K.; Kanamori, J., Magnetization process in antiferromagnets with a strong uniaxial anisotropy energy. *Prog. Theor. Phys.* **1967,** *38* (3), 541-550.

(23) Zhang, L. Z.; He, X. D.; Zhang, A. L.; Xiao, Q. L.; Lu, W. L.; Chen, F.; Feng, Z. J.; Cao, S. X.; Zhang, J. C.; Ge, J. Y., Tunable Curie temperature in layered ferromagnetic $Cr_{5+x}Te_8$ single crystals. *Apl. Mater.* **2020,** *8* (3), 031101.

(24) Sheldrick, G. M., Crystal structure refinement with SHELXL. *Acta. Crystallogr. C: Struct. Chem.* **2015,** *71* (Pt 1), 3-8.

(25) Wang, J.; Toby, B. H.; Lee, P. L.; Ribaud, L.; Antao, S. M.; Kurtz, C.; Ramanathan, M.; Von Dreele, R. B.; Beno, M. A., A dedicated powder diffraction beamline at the advanced photon source: Commissioning and early operational results. *Rev. Sci. Instrum.* **2008,** *79*, 085105.

(26) Lee, P. L.; Shu, D. M.; Ramanathan, M.; Preissner, C.; Wang, J.; Beno, M. A.; Von Dreele, R. B.; Ribaud, L.; Kurtz, C.; Antao, S. M.; Jiao, X.; Toby, B. H., A twelve-analyzer detector system for high-resolution powder diffraction. *J. Synchrotron Radiat.* **2008,** *15*, 427-432.

(27) Dalesio, L. R.; Hill, J. O.; Kraimer, M.; Lewis, S.; Murray, D.; Hunt, S.; Watson, W.; Clausen, M.; Dalesio, J., The experimental physics and industrial control-system architecture: Past, present, and future. *Nucl. Instruments Methods Phys. Res. A* **1994,** *352*, 179-184.

Chapter Specific Acknowledgement

Acknowledgment

It goes without saying that the completion of my Ph.D. is impossible without the support from lots of people. It is equally impossible to express my gratitude in a few pages to all of you who have enlightened this five-year journey, but here is a modest attempt:

I would like to first express my sincere appreciation to my advisor, Mircea Dincă, for his support, guidance, patience, and open mind. He has given me tremendous freedom to pursue what I am deeply passionate about, allowing me to work on a completely new research direction, encouraging me to build many collaborations, supporting me to follow my interest in patent law, and helping me with my job searching and law school application. I cannot be more grateful for what he has taught me over the past five years. When I become frustrated about my results, he nicely tells me what experiments I should do. When I lost my way in research, he wisely shows me how to tell a story based on what I have done. When I head in the wrong direction, he timely points out my mistake and patiently helps me to correct everything. If I were given the opportunity to re-select my group after being at MIT for five years, I would still choose the Dincă without any hesitation. Mircea, thank you so much. I will never forget your mentorship, and I am proud to be your student.

I would like to thank my committee chair, Prof. Tim Swager, and my committee member, Prof. Moungi Bawendi, for their support of my scientific endeavor. I still vividly remember the first time I stepped into Tim's office, and his first question for me was "describe your research to me in three minutes". He told me that I should always be prepared to introduce my research to a person out of my field within a few minutes, and it is beyond description how much this suggestion has helped me with my academic networking and job searching. Thank you, Tim, for always being this helpful in advising my research and career since our very first meeting. I am also grateful for Moungi's guidance on my research project, and I really admire his expertise in nanomaterials. He even allowed me to use all his lab instruments. My nanowires won't be possible without the fancy centrifuge and microscope in his lab.

I am grateful to all the members of the Dincă group. I want to start with thanking my very first mentor in the Dincă lab, Maxx Arguilla. Maxx is a fantastic mentor, both in science and life. I knew nothing about solid-state chemistry and nanotechnology until I met Maxx. He taught me how to start a flame, how to cut and seal glass and quartz tubes, how to use furnaces, how to exfoliate van der Waals materials, how to get high-quality SEM images without charging, how to take AFM and TEM, how to write a proposal, how to tell a story in a manuscript, how to choose a cover slide for my presentation, how to plan for life, how to choose a future career, how to catch the oyster happy hour while waiting for XPS measurements, how to find great Asian restaurants near Harvard CNS…It is my fortune to have met you and worked with Maxx, and I truly envy his current and future students at UC Irvine.

I must also express my gratitude to Lei Sun (孙磊). Although we have never worked in the Dincă lab for even one day, I have heard Lei's story since my sophomore year at Nanjing University. The Ph.D. application experience he shared with his following undergrads, including me, at Nanjing University was so helpful and inspiring and significantly changed the way I planned and prepared for my future when I was 19. Even after graduation, I can always turn to Lei when I need advice, and he constantly offers wise solutions and encouragement. Lei is not only a fantastic scientist but

also a great mentor and friend. It is not an exaggeration to say that without Lei, I would not be able to get into MIT and I won't be able to survive here.

I need to give special thanks to my labmates Tianyang Chen (陈天阳) and Mike Payne. Joining MIT chemistry in the same year, we have experienced too much together. We have struggled together facing the overwhelming course load, especially the extremely difficult homework of Bioinorganic Chemistry. We have survived the cold call of Prof. Cummins in 5.03. We have been so wise that we all chose the Dincă group. We passed the activation barrier of Ph.D., the second-year oral exam, on the same day. We have enjoyed so many group trips and group dinners sitting next to each other. We will graduate nearly together. It is bittersweet to be the first one to leave. I will always remember the days we spent together.

I also want to thank the more senior graduate students and postdocs in the Dincă group, who have taught me a lot about how to face frustrated data, how to avoid making Mircea unhappy during subgroups, and how to find good food in Cambridge. Eric, Adam, Maciej, Amanda, and Elise, thank you all for training me on lots of instruments and staying patient when I messed things up. Grigorii, thank you for teaching me the refinement skills and contributing so many joyful moments in subgroups and group meetings. Lilia, thank you for being such an excellent mentor and teaching me to use and maintain our PPMS instrument. Luming (杨露鸣), Jin-Hu (窦锦虎), and Kevin (孙晨悦), thank you for being nice friends and extremely helpful mentors. It is my fortune to have three reliable and wise senior labmates from China who can understand my concerns and provide constant help. I would also like to thank Ivo Stassen, Bobby Day, Ash Wright, Xin He, Dong-Gwang Ha, Rob Comito, and Connie Neumann for their scientifically inspiring suggestions on my project. Their passion for science and their well-organized working style has vividly taught me how to be a Ph.D. student. My life over the past five years has been consistently enriched by beautiful results and incredible scientific achievements from all of you, and I am looking forward to seeing what you all could accomplish in the future.

I want to thank everyone who joined the group later than me, who have brought fresh air to my daily work and make me happy when in the office. Ruomeng (万若萌), thank you for being such a considerate and reliable friend. I love all the food you have cooked, and I wish you the best in your future career. Jules, thank you for teaching me all the refinement skills. Your solid chemistry knowledge, deep love for inorganic chemistry, and the insights you gave to people during subgroups have impressed me greatly. And I really like the feeling of your hair. Andrei, thank you for your help with the PPMS and for being a humorous person. I wish I could have a chance to run with you in the future. Bhavish, thank you for being the social chair and bringing many joyful conversations to the table. Alice and Kim, thank you for being responsible colleagues. Your smartness and sharp mind have always been an encouragement for me as a woman in science. I am also grateful to Justin Andrews, Harish Banda, Alina Kampouri, Rain Mariano, Jiande Wang, Val Hosseininasab, Dong-Ha Kim, and Won Ho Choi for bringing their expertise and perspective to the lab. I can feel how diverse our group's expertise and research interests have become after you all join this group. I really appreciate all the provoking conversations we have had. Wish you all make amazing results in the Dincă group.

There is no word in any language strong enough to describe all the happy moments we have spent together. The photos will always be in my iCloud album, and the scenes will always be in my memory.

I am also grateful for the friendship and support I received from the MIT community. Wencong (王文聪) and Lennon (罗少雄), we have retired eight decks of worn-out cards over the past five years. I will always remember the days we played *Shengji* and Mahjong, traveled and cooked together, and went out for drinking. Thank you for adding colorful moments to the otherwise tedious experiment days. I want to thank my mentor at Women in Chemistry, Hanna Moon, who is always patient in answering my questions and selflessly helps me. I want to thank Bing Yan and Corey Kaminsky for their help with my second-year oral. I also want to thank my MIT classmates, Mengshan Ye (叶梦珊) and Zhongling Jiang (姜钟灵). You two are the first two classmates I met. You have brought me lots of happiness and beautiful memories. I also need to express my gratitude to my other MIT classmates Gen Li (李根), Weiwei Sun (孙维维), Juanye Zhang (张隽晔), and Sheng Feng (冯晟). It is fantastic to have met you at MIT and I wish our friendship will last forever.

I would reserve my special thanks to my scientific mentors and my very best friends before MIT. I want to thank my undergrad advisor, Prof. Xinping Wang (王新平), and Prof. Gengwen Tan (谭庚文). You two literally helped me grow from an undergrad who knew nothing about research to be a qualified Ph.D. candidate. The working styles, the research methods, and the rigorous attitude towards science I saw in both of you have permanently changed the way I conceive a project and how I carry out research. I am also extremely grateful to Prof. Lin Wu (吴琳), who taught me Organic Chemistry in my sophomore year. He not only taught me knowledge but also helped to build my confidence and interest in chemistry. Finally, I want to thank all my friends at Nanjing University: my classmates at the NJU chemistry and my teammates at the Debate Association. I cannot come up with any sentence to describe how amazing you are and how lucky I am to have met all of you. You brought me so much happiness. We cheered for success. We drank to vent frustration. We laughed together like the weirdest people in the world. We discussed literature, history, law, and philosophy for the entire night. Even though we are not in the same city or country anymore, your pure existence is enough to support me when I am suffering. Thank you for always being there for me, for better or worse, in good or bad times.

I want to thank my parents, Yanchang Qu (曲延昌) and Hongmei Du (杜红梅), who are professors in science and have cultivated my interest in natural science since I was very young. They helped to build my confidence and warmed my life with selfless love. I want to express my gratitude for the entire education I received in China in Chinese history, Chinese literature, and Chinese philosophy. As I grow older, I could resonate with more ancient poems and sayings, and the rich wisdom from Chinese culture has been a powerful spiritual support for my daily life. Although I have not been able to travel back to China during my Ph.D. years, there is never one moment that I am not missing my home country. Wish you prosperity, my dear motherland.

Finally, I want to thank Chenru Duan (段辰儒), for your love and care through every stage of my Ph.D. years. Ph.D. is a tough journey but has a color of sweetness because of you. In the end, I

want to thank myself and congratulate myself. No matter how much help and support I have received, it is I who have weathered every hardship, stayed positive and mentally strong, been persistent and hardworking, and gradually achieved what I have dreamed of. Wish I could stay creative, enthusiastic, determined, and strong as a Ph.D. student for my entire life.